UNIVERSITAT POLITÈCNICA DE CATALUNYA
BARCELONATECH
Escola Superior d'Enginyeries Industrial,
Aeroespacial i Audiovisual de Terrassa

Design and thermomechanical study of the case of a solid rocket motor of small dimensions

BACHELOR FINAL THESIS

Document:
Report

Author:
Jan Canet Vidal

Director / Co-director:
Dr. Juan Carlos Cante Terán
Dr. David Roca Cazorla

Degree:
Bachelor's degree in Aerospace Technology Engineering

Examination session:
Spring, 2022

Resum

En aquesta tesi s'ha dissenyat un motor de combustible sòlid capaç de propulsar un coet de petites dimensions anomenat Phobos fins a una alçada de 3 km en el marc de la competició europea EuRoC (European Rocketry Challenge). L'objectiu de la tesi ha estat també el de dissenyar un motor que fos més barat i accessible per grups d'estudiants com l'UPCSP (UPC Space Program), comparat amb els motors comercials utilitzats. En aquest sentit s'ha realitzat, d'una banda, un codi de balística interna, mitjançant Matlab, per avaluar el funcionament del motor, les corbes d'empenta i de pressió de cambra, i, d'altra banda, s'ha desenvolupat un estudi termomecànic d'una secció 2D axisimètrica de l'estructura per avaluar com afecta la temperatura en la integritat estructural dels components. La caracterització del procés de combustió s'ha realitzat a través del programa ProPEP 3 (Propellant Performance Evaluation Program), mentre que la simulació de vol del coet per determinar l'alçada màxima assolida s'ha dut a terme mitjançant el software OpenRocket. Respecte al preu, s'ha presentat també un pressupost del cost estimat de fabricació del motor. Els resultats obtinguts indiquen que per tal d'assolir l'alçada desitjada, donades les restriccions geomètriques de la carcassa, s'han d'emprar combustibles d'alt rendiment com el APCP (Ammonium Perchlorate Composite Propellant). Els resultats també mostren que com a conseqüència de les elevades temperatures assolides a la gola de la tovera, per conformar aquest component s'han d'utilitzar materials amb un alt punt de fusió i una conductivitat tèrmica superior a la de l'acer, tot mantenint unes càrregues límit similars a la d'aquest últim.

Abstract

In this thesis a solid propellant rocket motor capable of propelling a small scale rocket called Phobos up to a height of 3 km in the framework of the European EuRoC (European Rocketry Challenge) competition has been designed. The aim of the thesis was also to design an engine that was cheaper and accessible to groups of students such as the UPCSP (UPC Space Program), compared to the commercial engines used. In this sense, on the one hand, an internal ballistics code has been carried out, using Matlab, to evaluate the operation of the motor, the thrust and chamber pressure curves, and, on the other hand, a thermomechanical study of a 2D axisymmetric section of the structure has been developed to assess how temperature affects the structural integrity of components. The characterization of the combustion process has been carried out through the ProPEP 3 program (Propellant Performance Evaluation Program), while the flight simulation of the rocket to determine the maximum altitude reached has been carried out using the OpenRocket software. In terms of price, a budget for the estimated cost of manufacturing the motor has also been provided. The results obtained indicate that in order to reach the desired altitude, given the geometric restrictions of the case, high-performance fuels such as APCP (Ammonium Perchlorate Composite Propellant) should be used. The results also show that as a result of the high temperatures reached in the throat of the nozzle, the materials to be used to form this component must have a high melting point and a higher thermal conductivity than steel, while maintaining limit strengths similar to the latter.

Contents

List of Figures

List of Tables

List of Symbols

A	Area
A_b	Burning surface
A_t	Throat area
a	Speed of sound / Burn-rate proportional constant
$\boldsymbol{C}$	Elasticity matrix
C_d	Discharge coefficient
c_p	Specific heat at constant pressure
c^*	Characteristic velocity
D	Diameter
d	Diameter
E	Young modulus
F	Thrust
$\boldsymbol{f}$	Body force vector per unit volume
G	Transverse elastic modulus
g_0	Gravitational acceleration at Earth's surface
h	Enthalpy
h_g	Convective heat transfer coefficient
I_{sp}	Specific impulse
I_t	Total impulse
K_n	Burning to throat area ratio
L	Length
M	Mach number
M_p	Propellant mass
MW	Molecular weight
$\dot{m}$	Mass flow rate
m	Radius to thickness ratio

$\hat{\boldsymbol{n}}$	Normal unit vector
n	Burn-rate exponent / Number of moles
P	Static pressure
P_0	Stagnation pressure
P_c	Chamber pressure
P_d	Design pressure
P_u	Burst pressure
Pr	Prandtl number
$\dot{Q}$	Heat flow
$\dot{q}$	Heat flow per unit surface
R	Radius
R_g	Gas constant
R_u	Universal gas constant
r	Radial coordinate
r_b	Burn-rate
r_c	Radius of curvature
SF	Safety factor
T	Static temperature / Thrust
T_{aw}	Adiabatic wall temperature
T_c	Chamber temperature
T_w	Wall temperature
T_0	Stagnation temperature
t	Thickness / Time
$\boldsymbol{u}$	Displacement vector / Trial function
u	Internal energy
$\boldsymbol{v}$	Test function / Velocity vector
V	Specific volume
V_c	Chamber volume
V_{free}	Free volume
v	Velocity modulus
$\dot{w}$	Weight flow rate
z	Axial coordinate

α	Angle / Coefficient of thermal expansion
β	Strength ratio
Γ	Boundary
γ	Specific heat ratio
γ_{ij}	Engineering shear strain
$\boldsymbol{\delta}$	Unit tensor
$\boldsymbol{\varepsilon}$	Infinitessimal strain tensor
ε	Nozzle expansion ratio
ε_{ij}	Normal strain
η	Dynamic viscosity
θ	Azimuth coordinate
λ	First Lamé parameter / Thermal conductivity / Divergence angle correction factor
μ	Second Lamé parameter / Dynamic viscosity
ν	Poisson coefficient
ρ	Density
ρ_p	Propellant density
$\boldsymbol{\sigma}$	Stress tensor
σ_{ij}	Normal stress
σ_y	Yield strength
σ_u	Ultimate tensile strength
τ_{ij}	Shear stress
φ	Geometrical factor
Ω	Domain

List of Acronyms

AN Ammonium Nitrate. 7, 10, 35, 87

AP Ammonium Perchlorate. 7, 9, 10, 35, 36, 47, 48

APCP Ammonium Perchlorate Composite Propellants. 9

CAD Computed-aided design. 6

COTS Commercial off-the-shelf. vii, 2, 4, 12, 17, 32, 33, 81, 82, 87

CTPB Carboxyl-Terminated Polybutadiene. 8

DBP Dibutyl Phthalate. 8

DOA Dioctyl Adipate. 8, 35

DOF Degrees Of Freedom. 48

EuRoC European Rocketry Challenge. 1, 3, 4, 38, 85

FEA Finite Element Analysis. 5, 49

HTPB Hydroxyl-Terminated Polybutadiene. 8, 10, 34, 35

IDP Isodecyl Pelargonate. 8

MEOP Maximum Expected Operating Pressure. 14, 27, 30, 40

PBAN Polybutadiene Acrylonitrile. 8, 10, 34

PN Potassium Nitrate. 7, 9, 35, 36, 47

PVC Polyvinyl Chloride. 3, 29

SN Sodium Nitrate. 9

SRM Solid rocket motor. 4, 16

UPCSP UPC Space Program. 2, 4, 85

Chapter 1

Introduction

1.1 Objective

The aim of this thesis is to design a solid propellant rocket motor of small dimensions and to analyze the thermomechanical behavior of its structure.

Furthermore, this thesis sets the first design of a motor capable of propelling a model rocket named Phobos (see figure 1.1) to 3 km of altitude in the European Rocketry Challenge (EuRoC) competition. With this design and its corresponding thermomechanical analysis, further work such as implementation, manufacture and a satisfactory static fire test would be required prior to its launch in the competition but are kept out of the scope of this project.

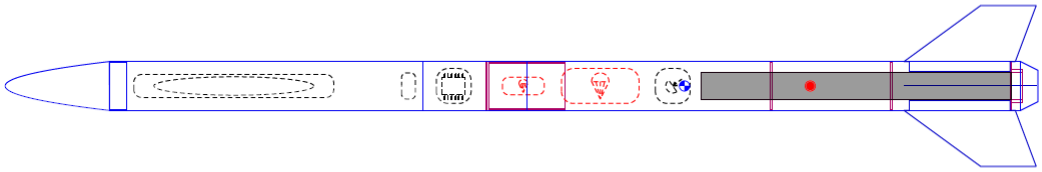

Figure 1.1: Schematic drawing of the Phobos model rocket.

1.2 Scope

In order to achieve the objectives of the thesis, the scope and limitations of the project involves the following:

- The thesis includes the motor components (case, nozzle, and forward closure) design, i.e., geometric definition and material selection.
- The thesis includes the propellant selection, by comparing the performance of several propellants.
- The thesis includes the propellant characterization but excludes the development of a chemical equilibrium combustion software. Thus, ProPEP 3 software will be used to determine the chemical equilibrium composition of the combustion products.

- The thesis includes the propellant grain design in terms of geometry.
- The thesis includes an analysis of the performance of the motor and the development of the corresponding code through Matlab. The thesis also includes the validation of the performance results through BurnSim and OpenMotor software.
- The thesis includes the simulation of the flight mechanics of the Phobos rocket with the designed motor installed but excludes both, the design of the rocket (since it is already designed by the UPC Space Program (UPCSP)), and the development of a flight mechanics code. Therefore, the flight simulation will be made through the OpenRocket software to determine the apogee reached.
- The thesis includes 2D axisymmetric thermal analysis of the motor components but excludes the development of a finite element code. Hence, ANSYS software will be used to determine the temperature and heat flux distributions.
- The thesis includes 2D axisymmetric thermomechanical analysis of the motor components using the ANSYS software to determine stress and strain distributions.
- The thesis excludes from its scope the development of economic feasibility analysis since the motor is not intended to be commercialized.
- The thesis excludes from its scope the implementation, manufacture, or the realization of a static fire test of the motor.
- The thesis excludes from its scope the manufacture of the propellant.
- The thesis excludes from its scope a very low cycle fatigue analysis of the motor components.
- The thesis excludes from its scope the design of an electrical motor igniter.
- The thesis excludes from its scope a two phase flow analysis of the combustion products.
- The thesis excludes from its scope the study of the structural integrity of the propellant grain.

1.3 Requirements

For the satisfactory completion of the project, the motor design must fulfill the requirements defined in tables 1.1 to 1.6. For each requirement there is a brief explanation of how is intended to be achieved or checked for compliance, and the purpose of them. There is as well a code for each one of the requirements to allow for an easy reference and traceability.

Table 1.1: General Requirements.

General Requirements		
Code	*Description*	*Comments*
GR-01	The motor shall be reusable.	This requirement will be taken into account in several parts of the thesis, including the material selection process, the design phase, and structural analysis.
GR-02	The total cost of the motor shall be less than the average cost of an equivalent Commercial off-the-shelf (COTS) motor.	This requirement will be taken into account during the design phase and checked during the budget calculation. Equivalencies between COTS motors can be made in terms of total impulse and diameter.

Table 1.2: Performance Requirements.

Performance Requirements		
Code	*Description*	*Comments*
PR-01	The motor shall not exceed an installed total impulse of 40960 N-s.	This requirement has to be fulfilled during the performance analysis of the motor and is imposed by the EuRoC competition.
PR-02	The motor shall propel the Phobos rocket to an altitude of 3000 m.	This requirement has to be fulfilled during the flight simulation via the OpenRocket software since it sets the target apogee.

Table 1.3: Material Requirements.

Material Requirements		
Code	*Description*	*Comments*
MR-01	PVC and similar low-temperature polymers and, Public Missiles Ltd. Quantum Tube components shall not be used in any structural capacity or propulsion system combustion chamber.	This requirement will be taken into account during the material selection process and is imposed by the EuRoC competition.
MR-02	Load-bearing bolts, if used, shall be made of steel or stainless steel.	This requirement will be taken into account during the material selection process and is imposed by the EuRoC competition.
MR-03	The materials selected to make up the motor case shall not be considered brittle.	This requirement will be taken into account during the material selection process and represents a safety measure in case of a motor explosion.

Table 1.4: Geometrical constraint Requirements.

Geometrical constraint Requirements		
Code	*Description*	*Comments*
GCR-01	The motor case's outer diameter shall be 75 mm.	This requirement has to be fulfilled during the design phase and is imposed by the motor mount dimensions of the Phobos rocket.
GCR-02	The motor case length shall be less or equal to 893 mm.	This requirement has to be fulfilled during the design phase and is imposed by the motor mount dimensions of the Phobos rocket.

Table 1.5: Propellant Requirements.

Propellant Requirements		
Code	*Description*	*Comments*
PRR-01	The propellant used shall be non-toxic[1].	This requirement will be taken into account during the propellant selection process, and is imposed by the EuRoC competition as a safety measure.

[1] "Toxic propellants are defined as those requiring breathing apparatus, special storage, and transport infrastructure, extensive personal protective equipment, etc."[1]

Table 1.6: Structural Requirements.

Structural Requirements		
Code	*Description*	*Comments*
SR-01	The motor shall be designed to a burst pressure no less than 2 times the maximum expected operating pressure.	This requirement will be taken into account during the design and analysis process, and is imposed by the EuRoC competition as a safety measure.

1.4 Justification

The engines used in the vast majority of model rockets are solid propellant rocket motors, or simply Solid rocket motor (SRM), given that they are the simplest motors that one can employ. Those, unlike liquid or hybrid propellant rocket motors, do not require turbomachinery, pipes, or propellant tanks to operate, and, in turn, those components increase complexity and inert mass to the rocket.

However, the engines are the most sophisticated components of the vehicle and are critical to ensuring a successful launch. For this reason, most model rockets include Commercial off-the-shelf (COTS) motors as part of their propulsion system.

Although COTS engines perform well and are reliable if assembled correctly, there are some problems associated. One of them has to do with the availability within Europe. Most manufacturers are from the USA and, because of some conflicts in American and European aviation regulations, motors are difficult to obtain and there are no estimates on arrival time. The second issue, which is related to the first one, is the high cost of the engines. For 75 mm diameter motors, the cost can scale up to 500 € [2] (reaching higher costs in more powerful motors) and can be increased due to transportation and hazardous material fees.

In this way, the main purpose of this thesis is to drastically reduce the uncertainty about the availability of the motors and the cost that they have in the Ares mission of the UPC Space Program (UPCSP), a student rocketry team from Universitat Politècnica de Catalunya, with regard to the EuRoC competition and further Ares projects.

1.5 Schedule

This section of the thesis includes the description of the work packages to be done in order to satisfy all the objectives and requirements (see tables 1.7 to 1.9). Furthermore, a Gantt diagram of the tasks has been developed to identify the project duration, the time destined to each work package, and its inter-dependencies (see appendix A).

Table 1.7: Bibliographic research tasks.

Bibliographic research tasks	
Tasks	*Description*
Elastostatic formulation	Formulation of the elastostatic theory of an axisymmetric body in cylindrical coordinates.
Heat transfer formulation	Formulation of the heat transfer equations in cylindrical coordinates.
Validation of numerical results	Validation of the numerical results of the ANSYS software through the analysis of three different cases with analytical solution.

Table 1.8: Design and Analysis tasks.

Design & Analysis tasks	
Tasks	*Description*
Case preliminary design	Preliminary design of the case, including material selection, geometric definition, and drawings.
Nozzle preliminary design	Preliminary design of the nozzle, including material selection, geometric definition, and drawings.
Forward closure preliminary design	Preliminary design of the forward closure, including material selection, geometric definition, and drawings.
Propellant selection	Selection of the propellants to be compared and used in the motor.
Grain design	Design of the grain geometry.
Propellant characterization	Characterization of the combustion products through the ProPEP 3 software, which determines the chemical equilibrium composition for the combustion of the solid propellant.
Performance analysis	Analysis of the performance of the motor through the development of a Matlab code, and several software like BurnSim and OpenMotor.
Flight simulation	Flight simulation of the Phobos rocket with the designed motor installed via OpenRocket software. This simulation serves to check the compliance of the target apogee required.
Thermal analysis	Thermal analysis of the motor components through a Finite Element Analysis (FEA) software such as ANSYS.
Thermomechanical analysis	Thermomechanical anlaysis of the motor components through a FEA software such as ANSYS.
Iterative design process	This task comprises all the iterative tasks of the design process.

Table 1.9: Documentation and Deliverables tasks.

Documentation & Deliverables tasks	
Tasks	*Description*
Appendices	Structure and write appendices.
Project charter	Development of the project charter.
State-of-the-art	Write the state-of-the-art chapter.
Drawings	Development of the drawings of the components through a Computed-aided design (CAD) software like SolidWorks.
Conclusions	Write the conclusions chapter.
Budget	Development of the budget of the project.
Environmental impact	Analysis of the environmental impact of the project.
Report	Write the thesis report.

Chapter 2

Review of the state of the art

In this section of the thesis, the current technologies regarding propellant formulation, manufacturing processes of structural components, and component assembly methods will be covered so as to get to know the available technologies that are employed in the amateur rocketry sector.

2.1 Solid propellants

Solid propellants can be classified in two main categories, double-base propellants or composite propellants. The first ones are a type of propellant that result in an homogeneous mixture, i.e., the ingredients are linked chemically, and they are made of nitrocellulose and nitroglycerin plus additives. However, in the amateur sector, the composite propellants are the ones that are extensively employed. Those, in the contrary, are heterogeneous because the ingredients are physically mixed and in general provide higher performance.

2.1.1 Components

A composite solid propellant can be made of multiple components or ingredients, each one with a specific function and objective (or multiple). Although some of the components presented below are present in every propellant formulation, there are some that might be present in only some formulations, since depending on the ingredients used the resultant mix will have different properties.

Oxidizer

The oxidizer is one of the main ingredients of the mixture and comprises the major part of the mixture with proportions around 60% to 85%. Its main function is to react with the fuel and deliver the high energy of the combustion process. It consists of a powder of an inorganic compound such as Ammonium Perchlorate (AP), Ammonium Nitrate (AN), Potassium Nitrate (PN), or others. In some cases, the size of this particles can be reduced to increase the performance of the combustion process, as is the case of AP.

Metal fuel

In some propellants, metal powders are add as a fuel to increase the total performance, since these are capable of increasing the heat of combustion, as well as the propellant density and the thermal conductivity. Which improves the burn-rate and, hence, the total specific impulse.
Typical metals used as fuels in amateur solid propellants are aluminium, iron oxide and in some cases magnesium, with percentages that range from 3% to almost 20% of the mixture.

Binder

The binder is also a main component in a solid propellant and has two main functions. The first is to act as a matrix or glue of the composite mixture by holding all the ingredients together and providing enough structural integrity to the mixture so that it keeps the shape while burning. The second main function is to act as a fuel and react with the oxidizer during the combustion. Some common binders are Hydroxyl-Terminated Polybutadiene (HTPB), Polybutadiene Acrylonitrile (PBAN), Carboxyl-Terminated Polybutadiene (CTPB) or epoxy. HTPB has been extensively employed in recent years due to the amount of research that has been performed, and because it allows higher fractions of solids (i.e., metal fuels or oxidizer), up to 90% [3].

Curing agent

Curing agents are the ingredients that cause the polymeric binders to form longer molecular chains and interlocks between them so as to solidify and harden the binder. They are also called crosslinkers because of its main function. They comprise a small fraction of the mixture (0.2% to 3%), however, variations of the fraction of this component can lead to serious problems in terms of aging (i.e., shelf life), physical properties or even manufacturing issues. The most commonly used crosslinkers are MDI isocyanate, DDI isocyanate and even epoxy resin [4].

Burning-rate modifier

Burn-rate modifiers are also called catalysts, because their main function is to enhance or reduce the burning-rate of the propellant. Some of these ingredients are also metal fuels such as aluminium or iron oxide powder, which increase the burning-rate, while others like lithium fluoride or ammonium chloride act as burn-rate suppressants by consuming combustion energy.

Plasticizer

The plasticizer is an ingredient used to improve the processing properties of the uncured mixture. Is is usually in the form of a low-viscosity liquid that reduces the glass transition temperature of the polymeric binder as well as the overall viscosity, and also acts as a fuel. It makes the manufacture of the propellant easier and in some cases can increase the pot life of the cured mixture. The most commonly used plasticizers are Dioctyl Adipate (DOA), Dibutyl Phthalate (DBP) and Isodecyl Pelargonate (IDP) [4].

Opacifier

The opacifier is a compound that is used only in semi-transparent propellants to generate opaqueness. Its main function is to avoid the heating of undesired parts of the propellant from the gas emitted radiation. It is usually present in very small fractions (around 0.1%) and does not contribute in the combustion.

2.1.2 Composite propellants

Here are classified some of the most widely used composite propellants in the amateur rocketry sector [5].

Sugar based

Sugar based propellants are probably the most commonly used in the hobby since they are the simplest, cheapest and easiest to manufacture. They are made of Potassium Nitrate or Sodium Nitrate (SN) as the oxidizer, and different sugar substitutes, like the ones below, as fuel.

- Potassium Nitrate/Sucrose
- Potassium Nitrate/Sorbitol
- Potassium Nitrate/Dextrose
- Potassium Nitrate/Fructose
- Potassium Nitrate/Erythritol
- Potassium Nitrate/Mannitol
- Potassium Nitrate/Xylitol
- Potassium Nitrate/Sorbitol/Aluminium
- Potassium Nitrate/Potassium Perchlorate/Sorbitol
- Sodium Nitrate/Sucrose/Iron oxide
- Sodium Nitrate/Sucrose/Iron oxide/Aluminium
- Sodium Nitrate/Sorbitol/Iron oxide/Aluminium

Standard formulations use an oxidizer to fuel ratio of 65/35.

Some of the drawbacks of this type of propellants is that they are heat-cast, this means that in order to be mixed, they have to be melted by the addition of external heat so that later can be cast inside a casting tube. This can be dangerous since the auto-ignition temperature of the components could accidentally be exceeded during the process. In addition, they are considered to be in the low-performance range of the propellants, since the ingredients are not as energetic as for example AP.

Ammonium perchlorate based

Ammonium Perchlorate based propellants use small particles of AP (in the range of 100 μm to 600 μm) as the oxidizer. They are also known as Ammonium Perchlorate Composite Propellants (APCP) and are considered to be high-performance propellants because of the specific impulses delivered (above 200 s)[1].

Some typical formulations of this propellants are presented below.

- Ammonium Perchlorate/Silicone II

[1]Specific impulse is a parameter that is measured in seconds and is widely used in rocketry to compare different motor performances. Reasonable values of performance range between 200 s to 280 s, see chapter 4 for more details on that.

- Ammonium Perchlorate/PBAN/Epoxy
- Ammonium Perchlorate/PBAN/Epoxy/Aluminium
- Ammonium Perchlorate/HTPB/Aluminium
- Ammonium Perchlorate/Epoxy/Iron

Although the binders of this propellants are in liquid phase at room temperature, some of them (PBAN and HTPB) can not be cast, because the uncured mixture becomes puttylike, thus, they have to be packed into a mold. The drawback of this is that air can be trapped during the process if not done carefully.

In terms of curing, HTPB has the advantage of curing at room temperature, while PBAN in the contrary, has to be cured at elevated temperatures (around 60 $°C$) for several days. Moreover, the AP/Epoxy/Iron formulation also cures at room temperature but at the expense of having to be pressurized at 28 bar to eliminate the porosity.

Ammonium nitrate based

Ammonium Nitrate based propellants utilize AN particles as the oxidizer, and are almost as efficient as AP-based, delivering specific impulses in the range of 200 - 215 seconds [5]. Those type of propellants came from the attempts of developing cleaner propellants and are a good alternative to AP, since the latter contains HCl molecules (a polluting agent) in the exhaust products [6]. However, the principal drawback of AN-based propellants is that Ammonium Nitrate is very hygroscopic, i.e., it tends to absorb moisture with ease. The problem with this is that during the curing process gases can generate inside the propellant, creating voids[2]. That is why this type of propellants need proper storage conditions.

Some formulations of AN-based propellants are:

- Ammonium Nitrate/Aluminium/Neoprene
- Ammonium Nitrate/HTPB/Magnesium
- Ammonium Nitrate/Ammonium perchlorate/Silicone

Others

Some other propellant formulations that do not strictly belong to a specific group are:

- Zinc/Sulfur
- Potassium Nitrate/Epoxy/Iron oxide

The first one is not in use nowadays and is probably the simplest to manufacture, since it only comprises the mixing of two powders. However, it delivers a low impulse and has an uncontrollable burning-rate.

The second one, belongs to the mid-performance category, nevertheless, has the advantage of being manufactured and cast at room temperature (cold-cast). It also has a low unit cost (around 7.10 $\$/kg$ [5]), good machineability (which allows the drilling of different core shapes) and resistance to accidental ignition.

[2]The formation of voids and cracks in solid propellants is of major concern, since they drastically increase the exposed surface. This results in an increase of combustion gas generation inside the chamber that rises the pressure beyond the expected.

2.2 Components manufacturing

There are several ways to manufacture the motor components to suit the desired objectives and comply with all the requirements imposed. However, they depend on the material they are made of. The most typical materials used in this type of applications are aluminium and steel alloys, phenolic resins and carbon fiber composites.

If the materials to be used are metals such as aluminium or steel alloys, the machining of the components is a reasonable manufacturing method. The way in which the desired motor part is formed is by progressively removing extra material from an initial block of metal, which is fixed by one end to a lathe where it rotates (see figure 2.1). In this way, the operator gives shape to the final component by employing some specific sharp tools. Depending on the hardness of the metal used, this process can take just a few hours or prolong several more hours. The total cost of this process highly depends on the time employed by the operator, thus, a more refined and detailed design could cost more than a simpler one, even though it requires slightly more material.

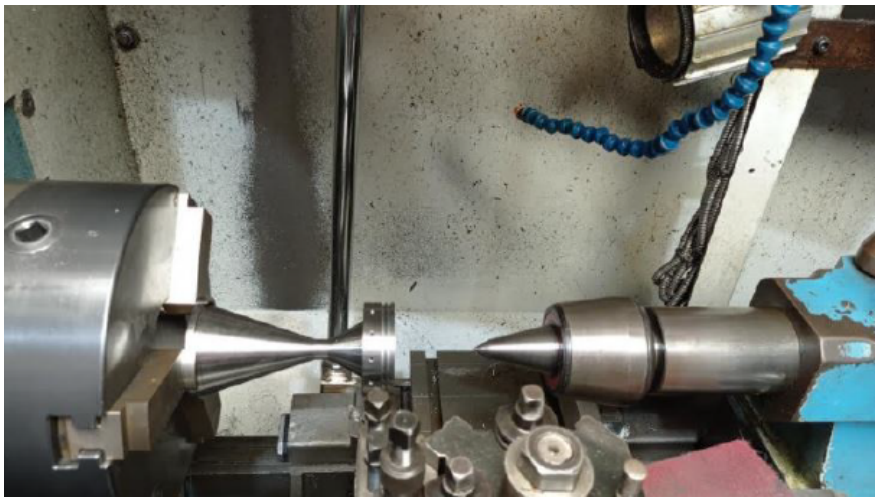

Figure 2.1: Machined aluminium nozzle. Source: [7].

One more way in which a metallic component could be manufactured would be by 3d-printing it. Some companies have special 3d printers that instead of printing with plastic, can print metal pieces. This however, is a highly expensive method of manufacture, since then the components need to be sand in order to have the desired finish.

Another option is to use a metallic tube of standard dimensions from the market in the design, and to modify it so as to comply with the assembly interfaces. This can also be done if the case is meant to be made of carbon fiber composite, since some online stores provide standard casing tubes.

If however, the case needs to be made of composite materials but with non-standard dimensions, then the manufacturing process needed would require a filament winding machine (see figure 2.2). This is required to wind all the fibers around a mandrel with the same diameter as the case. Later, after the polymeric matrix is applied, it would need to be cured in a special oven in order to solidify.

Figure 2.2: Filament winding machine for composite motor cases and pressure vessels manufacture. Source: <https://www.compositeautomation.com/filament-winding-machines/>.

2.3 Assembly mechanisms

Currently there are four methods in which the motor components can be assembled to the casing and held together.

- *Snap-ring.* This element is a C-shaped opened ring with holes in the edges. The way in which is used to assemble the nozzle and the forward closure to the case is shown in figure 2.3. The case shall be thick enough so as to enable the perforation of a groove in the inside surface of both ends. The snap-ring is fitted inside the groove by shrinking it from the edges (that is why it is an open ring), where it then expands, thus preventing the nozzle or the closure from moving outside the case. The drawback of this method is that it only prevents the displacement of the components in one direction but not through the interior. However is commonly used in low and mid-power COTS motors.

- *Threaded caps.* As the name suggests, this assembly mechanism holds the components together by means of a threaded closure that is screwed into the case. Sometimes, the nozzle and the forward closure are retained by means of external threaded caps that prevents them from getting apart. This mechanism is the most used in commercial motors because of its simplicity and is employed in all types of motors. Figure 2.3 shows an image of a COTS threaded forward closure.

- *Radial bolts.* This assembly mechanism retains the nozzle as well as the forward closure to the case through several bolts that are inserted radially (see figure 2.3). This is a less common method, since it is used in high-power rockets made by the amateur community, and it is not used in commercial motors, where threaded caps are preferred. The advantage over the latter method is that it is easier to manufacture, however is more time consuming in terms of assembly and disassembly, while at the same time increments slightly the inert mass of the motor.

- *Epoxy.* This last mechanism consists in gluing the components to the case with a significant amount of epoxy resin, as in figure 2.4. It is only used by some rocketeers

in low-impulse motors, since it is not reliable enough for bigger motors.

Figure 2.3: Top picture shows a motor with a radial bolt assembly, bottom left shows a threaded forward closure, and bottom right depicts a snap-ring assembly.

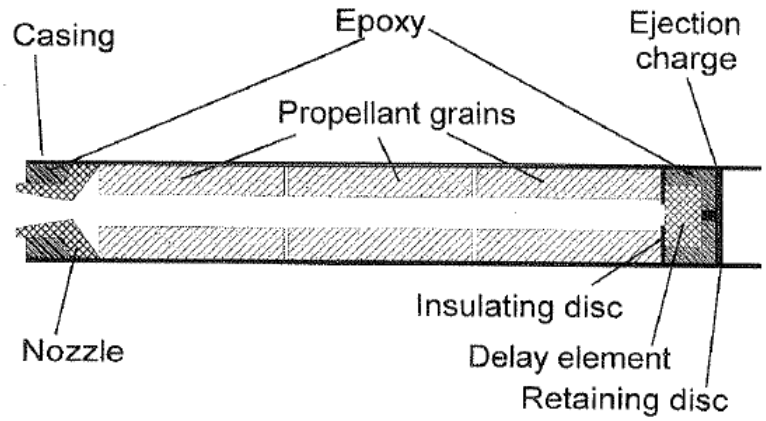

Figure 2.4: 2D diagram of a solid rocket motor with the nozzle glued to the case with epoxy. Source: [4].

Chapter 3

Methodology

This section covers the steps to be followed to obtain a motor design that fulfills the objectives and requirements of the thesis.

The design of a solid rocket motor is not a straight forward task, but rather a process where a set of requirements and constraints have to be continuously evaluated. Since they can be met in a variety of ways, the decisions of every design step have to be based on a selection criteria. Therefore, this process is expected to be made by a series of iterative analysis and redesigns.

The way in which the design process will develop is depicted in the diagram of figure 3.1. Here the design requirements and the rocket interfaces, defined in chapter 1, will set the basis of the preliminary design.

This preliminary design is meant to serve as an approach to the definitive solution, where analytical expressions and decisions based on cost, schedule, scope, selection criteria and the state of the art, will be employed to draft a first conceptual design of the motor.

The manner in which the preliminary design is intended to be approached is the following: First, the case will be sized based on the geometrical constraints, and then the materials to be employed will be selected. With this information, the burst pressure can be estimated and the Maximum Expected Operating Pressure can be defined. Later, the assembly mechanism will be defined and the forward closure sized. Note that these designs will be based on initial assumptions or predefined values that are subjected to change throughout the course of the desing process.

Next, the thermal insulation method will be tackled, followed by the selection and characterization of the possible propellants, which will be performed via the ProPEP 3 software (a propellant evaluation program).

Once the propellant is selected, the possible grain configurations will be evaluated, and finally, when the rest of the information is known, the nozzle will be sized.

When the preliminary design phase finishes, the proposed solutions obtained will be evaluated in the next design phase, the performance evaluation.

The performance evaluation phase will consist in two performance analysis. The first will evaluate the performance of the motor itself. This will be done with the development of the pertinent code (developed in Matlab). The second performance analysis will be related with the altitude reached by the Phobos rocket. This will be done via the OpenRocket software and will evaluate if the apogee requirement is met and, therefore, the proposed solution can continue forward in the design process, or, in the contrary, the proposed solution has weaknesses and has to go back to the preliminary design phase to be reviewed.

If the proposed solution overcomes the performance evaluation phase, then will be subjected to the detailed design phase, where finite element analysis will be performed to verify the operation of the structure. The first analysis to be performed will be a bi-dimensional axisymmetric thermal analysis, followed by a bi-dimensional axisymmetric thermomechanical analysis. Both of them will be developed via ANSYS. In the first one the temperature distribution will be obtained and serve as an input for the second one. In addition, it will also act as a filter for the proposed solutions that do not surpass this first simulation, for example a motor design that reaches the melting temperature. In the second, however, the stress distribution will be obtained to evaluate the structural integrity of the overall assembly.

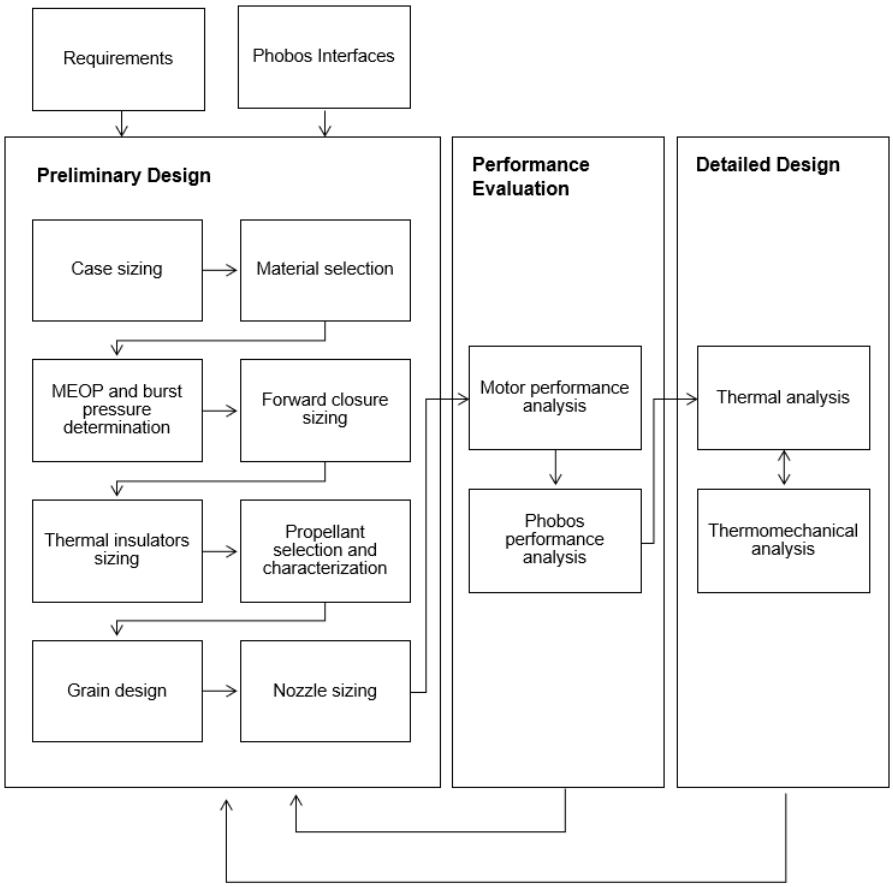

Figure 3.1: Workflow of the solid rocket motor design process.

Chapter 4

Theoretical base

Prior to the design process of the motor itself, a few theoretical concepts should be explained to fully understand the operation of a solid propellant rocket motor, and the decisions behind every design step.

In the next sections of this chapter, the fundamentals and the theoretical basis of solid rocket motors are expounded. These include the functioning and the components that make up a solid rocket motor, some of the basic thermodynamic relations that occur in the nozzle, the most typical propellants and their additives, the importance of heat transfer, and structural integrity concepts.

4.1 Definitions and fundamentals

The operation of solid propellant rocket motors is relatively simple in comparison to liquid propellant rocket engines, since there is no need to use separate tanks to carry the propellant, nor pipes and turbo-pumps to direct the propellant to the combustion chamber and neither injectors. Even the staring of SRM is much simpler.

A solid rocket motor operates as follows: first, an internal (in professional motors) or external (in amateur and commercial motors) igniter initiates the combustion process of the solid propellant. When the exposed surfaces of the propellant grain start to burn, combustion product gasses are generated inside the combustion chamber, thus, increasing the pressure. Then the gasses flow through the nozzle, where they expand until the exit is reached. The pressure at the combustion chamber increases very rapidly or progressively, depending on the grain geometry, therefore, raising the expelled mass flow, which increases until it gets to the chocked condition. The chocked condition is achieved in a rocket motor when the gas reaches Mach 1 at the minimum area section, i.e., the throat. In chocked condition, the flow is not affected by downstream pressure variations or perturbations, however, it is affected by the upstream pressure variations, i.e., the chamber pressure. When this condition is reached, the flow in the diverging section of the nozzle becomes supersonic. At the same time all this is occurring, the expelled mass and the pressures applied by the hot gas in the motor walls generate a force in the same direction of the flow but in the opposite way, that is the thrust. When the propellant is fully consumed, the pressure inside the chamber decreases exponentially until ambient pressure is reached.

There is also a huge difference between the SRMs that are used for professional aerospace applications and space exploration to the ones used in the amateur level. The latter are much simpler and can be divided in two types: single-use and reusable motors.

Single-use motors usually deliver less total impulse than reusable motors and are intended to be used a single time, as the name suggests, since they are made from phenolic resins that erode during operation and which can not be disassembled.

In the other hand, reusable motors can be used several times by allowing the disassembly of the motor and the removal of the charred components, thus, leaving space to add new ones and new propellant grains at each flight. Those type of motors use metal cases so as to withstand all the loads and to permit its reusability. The nozzles, however, can also be metallic, and thus, reusable, or simply single-use. The latter can be made of phenolic resin or can be made of steel with graphite inserts at the throat region, which erodes during operation.

Yet another way of classifying solid rocket motors exists and is widely used in the amateur sector. It separates the motors by the total impulse generated, giving a letter from A to O to each of the impulse ranges. This classification is showed in table 4.1. As it can be seen, each letter range doubles the impulse from the previous one until a maximum of 40960 $N \cdot s$ is reached, since it is considered to be the limit for amateur rocket motors.

Then, after the letter, a number that represents the average thrust of the motor that is to be named is added. So for example, an $L995$ (41% L) motor has an average thrust of 995 N, and has a total impulse that is between 2560 $N \cdot s$ - 5120 $N \cdot s$. More specifically, has a total impulse of 3618 $N \cdot s$, since it is defined as a 41% L motor.

This method of labeling the motors is used in COTS motors and will also be used in this thesis.

Table 4.1: Solid rocket motor letter classification by total impulse.

Class	Total Impulse ($N \cdot s$)	Class	Total Impulse ($N \cdot s$)
A	1.26 – 2.5	I	320 – 640
B	2.5 – 5	J	640 – 1280
C	5 – 10	K	1280 – 2560
D	10 – 20	L	2560 – 5120
E	20 – 40	M	5120 – 10240
F	40 – 80	N	10240 – 20480
G	80 – 160	O	20480 – 40960
H	160 – 320		

4.1.1 Motor components

The main components of an amateur reusable motor are depicted in figure 4.1, where the hardware from a I435T-M motor is shown as an illustrative example.

As it can be seen from figure 4.1, the motor is composed of:

- Motor case (7). Acts as a combustion chamber, houses the propellant, withstands the pressure generated by the combustion products, and is the responsible to transmit all the thrust to the rest of the rocket.
- Forward closure (14). Covers the upper end of the motor and withstands the axial loads produced by the gas.
- Aft closure (2). Retains the nozzle and withstands the axial loads produced by the gas.
- Liner / Thermal insulator (6). Protects the case from the extreme temperatures that generate inside the chamber.

- Propellant grains (8). The solid propellant itself, which is bonded to the casting tube where it was manufactured.
- Forward and aft insulation discs (9 and 5). Protect both the forward closure and the nozzle from the temperatures of the chamber.
- Forward and aft o-rings (10 and 4). Seal the ends of the motor so as to avoid gas leakages and motor failure.
- Nozzle (3). Increases the thrust of the motor by expanding the combustion products to ambient pressure while increasing its velocity.

Some motors, like the one showed in figure 4.1, can include an ejection charge and a delay grain inside the forward closure. The intention behind this is that while the motor operates, the delay grain is consumed. This delay is adjusted to end burning at the rocket apogee so as to ignite the ejection charge and eject the rocket parachute at the apogee.

Nevertheless, this is not a recommended technique, since the precision in adjusting the delay grain is very poor.

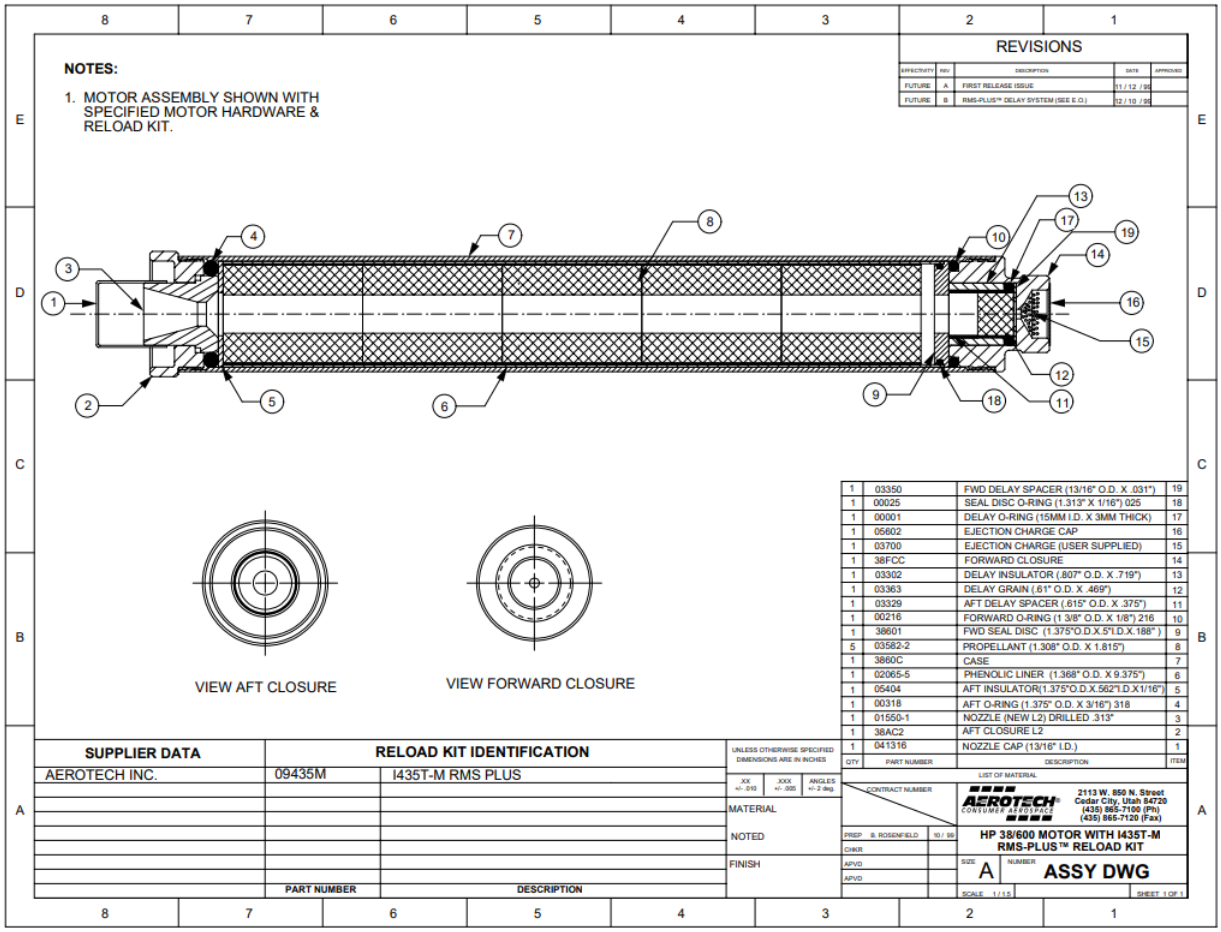

Figure 4.1: Assembly drawing and hardware breakdown of an I435T-M motor.
Source:<https://www.rocketmotorparts.com/page/motor-assembly-drawings>

4.2 Ideal nozzle theory

In this section, the ideal nozzle theory will be briefly explained in order to derive the mathematical relationships that will be employed in the preliminary design chapter to determine the key design parameters. The idea of an ideal propulsion system is usually used in early design phases so as to simplify the gas dynamics principles and the thermodynamic processes that occur inside the nozzle.

The assumptions that define an ideal nozzle are the following: (1) The working fluid obeys the perfect gas law, (2) Adiabatic flow, that is no heat losses through the walls, (3) There is no friction at the walls and boundary layer effects are neglected, (4) There are no shock waves within the flow, (5) All exhaust gases are ejected in the direction of the nozzle axis, (6) Gas variables such as temperature, pressure, velocity and density, are considered to be uniform throughout any of the nozzle cross-sections, that is quasi-one-dimensional flow, (7) The working fluid is assumed to be in a frozen composition, i.e., the gas composition remains constant across the nozzle length, (8) The flow is isentropic and compressible, (9) Steady-state flow.

However, real nozzles do not perform like that, so in order to take losses of performance into account, a set of correction factors, each one accounting for a different feature, are always applied after the ideal nozzle analysis.

From the conservation of energy in an adiabatic and isentropic flow, the decrease in enthalpy between two axial cross-sections can be expressed as an increase in kinetic energy, because changes in potential energy are neglected

$$h_x - h_y = c_p(T_x - T_y) = \frac{1}{2}(v_x^2 - v_y^2) \tag{4.1}$$

By applying the conservation of mass principle of steady-state flows, for one inlet and one outlet control volumes, the obtained mass flow rate can be expressed in terms of the cross-section (A), the velocity (v) and the specific volume (V)

$$\dot{m}_x = \dot{m}_y = \frac{Av}{V} \tag{4.2}$$

The perfect gas law is expressed as follows

$$P_x V_x = R_g T_x \tag{4.3}$$

where R_g is the gas constant, which depends on the universal gas constant and the molecular weight of the gas ($R_g = R_u/\mathrm{MW}$).

In any isentropic process, the subsequent expression holds true

$$\frac{T_x}{T_y} = \left(\frac{P_x}{P_y}\right)^{\frac{\gamma-1}{\gamma}} \tag{4.4}$$

The stagnation temperature, which in adiabatic flow remains constant, can be expressed as the sum of the local static temperature and a kinetic energy contribution.

$$T_0 = T + \frac{v^2}{2c_p} \tag{4.5}$$

From now on, the stagnation conditions will be presented with the subscript 0, whereas the subscripts 1, t and 2, are kept for describing the nozzle inlet, throat and exit sections, respectivly.

From previous equations and the Mach number definition ($M = v/a = v/\sqrt{\gamma R_g T}$), the ratio between stagnation and static temperature can be written as

$$\frac{T_0}{T} = 1 + \frac{1}{2}(\gamma - 1)M^2 \tag{4.6}$$

and the ratio between stagnation and static pressure as

$$\frac{P_0}{P} = \left[1 + \frac{1}{2}(\gamma - 1)M^2\right]^{\frac{\gamma}{\gamma-1}} \tag{4.7}$$

By applying equations (4.2), (4.3), (4.6) and (4.7), the area ratio between any two nozzle cross-sections can now be expressed in terms of the Mach number as follows

$$\frac{A_y}{A_x} = \frac{M_x}{M_y}\sqrt{\left[\frac{1 + (\frac{\gamma-1}{2})M_y^2}{1 + (\frac{\gamma-1}{2})M_x^2}\right]^{\frac{(\gamma+1)}{\gamma-1}}} \tag{4.8}$$

Another important variable that is directly related with the thrust generated is the exhaust or exit velocity, which can be derived from equation (4.1)

$$v_2 = \sqrt{2(h_1 - h_2) + v_1^2} \tag{4.9}$$

However, when $A_t/A_1 << 1$, the inlet velocity becomes so small that the term v_1^2 can be neglected, and the inlet properties (T_1, P_1) differ little from the stagnation conditions (T_0, P_0). Therefore, by applying equations (4.1), (4.4) and the specific heat relation for isotropic gases ($c_p = \gamma R_g/(\gamma - 1)$), the latter expression can be rewritten as

$$v_2 = \sqrt{\frac{2\gamma}{\gamma - 1}\frac{R_u T_0}{\mathrm{MW}}\left[1 - \left(\frac{P_2}{P_0}\right)^{\frac{(\gamma-1)}{\gamma}}\right]} \tag{4.10}$$

Sometimes it is useful to express any nozzle cross-section in terms of its local static pressure, instead of the Mach number. This can be obtained by applying equation (4.2) in the throat and in an arbitrary section and equating both. Then equations (4.3), (4.4), (4.10) are substituted taking into account that for choked conditions $M_t = 1$. The resulting expression writes as

$$\frac{A_t}{A} = \left(\frac{\gamma + 1}{2}\right)^{\frac{1}{(\gamma-1)}}\left(\frac{P}{P_0}\right)^{\frac{1}{\gamma}}\sqrt{\frac{\gamma + 1}{\gamma - 1}\left[1 - \left(\frac{P}{P_0}\right)^{\frac{(\gamma-1)}{\gamma}}\right]} \tag{4.11}$$

The mass flow rate expression in steady and choked conditions can be rewritten as

$$\dot{m} = A_t P_0 \gamma \frac{\sqrt{\left(\frac{2}{\gamma+1}\right)^{\frac{(\gamma+1)}{(\gamma-1)}}}}{\sqrt{\gamma R_g T_0}} \tag{4.12}$$

With respect to the thrust generated by the motor, it is composed of two contributions: the first is the expulsion of large amounts of gas at high velocities, and the second is the

contribution of the atmospheric pressure (P_3) that surrounds the motor surface. The total thrust can be computed as

$$F = \dot{m}v_2 + (P_2 - P_3)A_2 \tag{4.13}$$

Note that in space, P_3 vanishes, and, although it might seem non-intuitive, for a given altitude, the thrust generated is maximum only if $P_2 = P_3$. Because even if $P_2 > P_3$ would seem that the thrust is higher than in the previous condition, the truth is that the first term would be decreased because of the incomplete expansion of the gas inside the nozzle.

Other important parameters to be defined are the total impulse, which is defined as the integral of the thrust over time

$$I_t = \int_0^t F dt \tag{4.14}$$

and the specific impulse, which is the ratio of the thrust generated over the weight flow.

$$I_{sp} = \frac{I_t}{m_p g_0} = \frac{F}{\dot{m} g_0} = \frac{F}{\dot{w}} \tag{4.15}$$

here m_p is the propellant mass and g_0 the acceleration of gravity at Earth's surface.

Although the specific impulse is measured in seconds, serves as a figure of merit for comparing the performance of different motors and propulsion systems. The higher the I_{sp}, the more efficient a motor is, since it produces more thrust for the same amount of propellant.

4.3 Internal ballistics

The internal ballistics makes reference to the study of the combustion characteristics of the solid propellant grain. It describes the the parameters that affect the burning and operation of the propellant.

The first of these parameters is the burning-rate (r_b). It is the rate at which the grain is consumed. The regression of the web, i.e. the propellant thickness, is basically perpendicular to its surface and is highly related with the chamber pressure. The most common function of the burning-rate is known as the APN model (see equation (4.16)). It is an empirical generalization that states that the burning rate can be described through the chamber pressure (P_0), a proportional constant (a), and an exponential constant (n). The last two are experimental parameters that depend on the propellant of study.

$$r_b = aP_0^n \tag{4.16}$$

Other expressions of the burning-rate have been formulated, including erosive burning, ambient temperature dependence or rocket acceleration enhancements, however, those expressions require sophisticated experimental data of the propellant retrieved from exhaustive laboratory characterization.

The mass flow rate at which the gases at the combustion chamber are generated is a function of the burning-rate as well as the burning area (A_b) and the solid propellant density (ρ_p).

$$\dot{m} = A_b r_b \rho_p \tag{4.17}$$

In the previous equation, the propellant density remains constant, whereas the burning-rate and the burning surface change in time. This two parameters can be used in the design process to obtained the desired performance. If for example, the grain is designed such that

A_b only increases with time, the thrust profile obtained will be progressive. If it decreases with time, the thrust profile obtained will be regressive, and if the grain is designed such that A_b remains constant through the whole burn, the thrust profile obtained will be neutral (see figure 4.2).

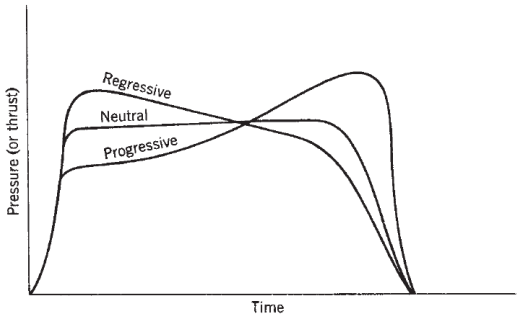

Figure 4.2: Types of thrust-time profiles. Source: [3]

Figure 4.3 shows the regression of different grain configurations and how they affect to the thrust profile.

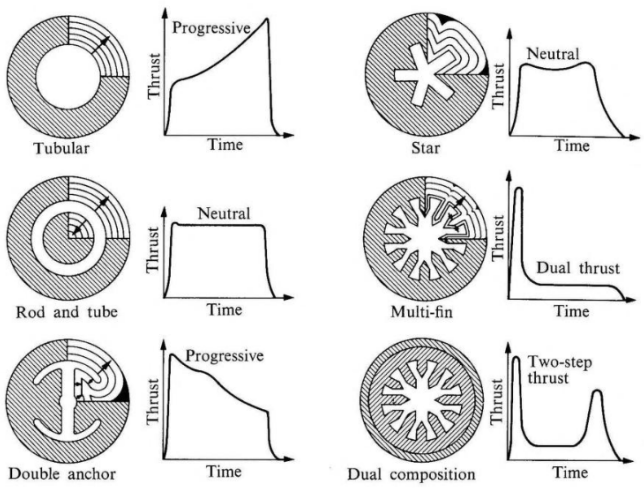

Figure 4.3: Regression and thrust profiles of several grain configurations. Source: [8]

Another important parameter that is used in the design of solid propellant rocket motors is the burning to throat area ratio (A_b/A_t). It is a dimensionless coefficient denoted as K_n that can also be expressed in terms of the chamber pressure by applying the mass conservation principle inside the chamber.

$$K_n = \frac{A_b}{A_t} = \frac{P_0^{1-n}}{a\rho_b c^*} \tag{4.18}$$

here c^* is known as the characteristic velocity and can be computed in terms of the chamber pressure, the throat area, and the nozzle mass flow rate

$$c^* = \frac{P_0 A_t}{\dot{m}} = \frac{\sqrt{\gamma R_g T_0}}{\gamma\sqrt{\left(\frac{2}{\gamma+1}\right)^{\frac{(\gamma+1)}{(\gamma-1)}}}} \tag{4.19}$$

Note that the characteristic velocity only depends on the propellant properties, that is the combustion temperature, the gas constant, and the specific heat ratio. Therefore, it is a good parameter to compare propellant performance.

4.4 Heat transfer

One of the main concerns in rocket motors are the high temperatures that generate in the combustion chamber, which in some cases can scale up to 2500 K. Thus, the biggest threat is the melting or the weakening of any of the motor structural components, which could lead to a total failure. Therefore, controlling the temperature of the motor components is of major importance, and thermal analysis are necessary to ensure the integrity of the motor.

4.4.1 Convective heat transfer at the nozzle

The main mechanisms of heat transfer from the hot gas to the nozzle walls are convection and radiation. The first one has a dominant effect in the overall response, since the heat flux transferred by convection is influenced by the velocity at which the gas travels, and in a rocket motor nozzle the velocities achieved are supersonic. The radiation heat transfer though, can be significant if the amount of solid particles or liquid droplets present in the gas are remarkable, however, this heat transfer mechanism will be neglected.

The convective heat flux that generates inside the nozzle is the following

$$\dot{q} = h_{g_2}(T_{aw} - T_w) \tag{4.20}$$

where T_{aw} is the adiabatic wall temperature, which is dependent of the local Mach number, the specific heat ratio, and the dimensionless Prandtl number [9],

$$T_{aw} = T_0 \left(\frac{1 + \mathrm{Pr}^{0.33} \left(\frac{\gamma-1}{2}\right) M^2}{1 + \frac{\gamma-1}{2} M^2} \right) \tag{4.21}$$

and, h_{g_2} is the convective heat transfer coefficient, which is can be computed through the semi-empiric Bartz formula [10][11].

$$h_{g_2} = \left[\frac{b}{D_t^{0.2}} \left(\frac{\mu_0^{0.2} C_p}{\mathrm{Pr}^{0.6}} \right) \left(\frac{P_0}{c^*} \right)^{0.8} \left(\frac{D_t}{r_c} \right)^{0.1} \right] \left(\frac{A_t}{A} \right)^{0.9} \sigma \tag{4.22}$$

where

$$\sigma = \frac{1}{\left[\frac{1}{2} \left(\frac{T_w}{T_0} \right) \left(1 + \frac{\gamma-1}{2} M^2 \right) + \frac{1}{2} \right]^{0.8-m/5} \left[1 + \frac{\gamma-1}{2} M^2 \right]^{m/5}} \tag{4.23}$$

μ_0 is the gas viscosity evaluated at stagnation conditions, r_c is the throat radius of curvature, and D_t is the throat diameter.

According to [11], the Prandtl number can be expressed in terms of the specific heat ratio as

$$\mathrm{Pr} = \frac{\gamma}{1.77\gamma - 0.45} \tag{4.24}$$

and, also according to [11], the coefficients m and b from equation (4.22) and (4.23) take the subsequent values

$$\begin{aligned} m &= 0.75 \\ b &= 0.026 \text{ (for subsonic speed)} \\ b &= 0.023 \text{ (for supersonic speed)} \end{aligned}$$

From equation (4.22) some observations must be pointed out:

- The heat flux is almost linear with the chamber pressure ($h_{g_2} \sim P_0^{0.8}$).
- The maximum heat flux occurs at the throat, where A is minimum ($h_{g_2} \sim (A_t/A)^{0.9}$).
- The lower the molecular weight of the gas, the higher the heat flux ($c_p \sim (1/MW)$, $c^* \sim (1/MW)^{0.5} \longrightarrow h_{g_2} \sim (1/MW)^{0.6}$).
- The sharper the radius of curvature, the higher the heat flux ($h_{g_2} \sim (1/r_c)^{0.1}$).

4.4.2 Effect of heat losses

In real nozzles, part of the thermal energy of the flow is lost through the walls of the nozzle in the form of convective heat flux. These losses can not turn into kinetic energy and, thus, the total performance of the motor is reduced. This is generally taken into account by computing the effective exhaust velocity of the gasses, which is lower than the ideal one.

The total heat flux lost at the walls of the nozzle can be computed by integrating the heat flux per unit surface along the inner nozzle area.

$$\dot{Q}_w = \int_{S_{int}} \dot{q}_w dS \tag{4.25}$$

The fraction of heat lost is then evaluated by dividing the losses over the total heat flux generated at the combustion chamber

$$\frac{\dot{Q}_w}{\dot{Q}_T} = \frac{\dot{Q}_w}{\dot{m} c_p T_0} \tag{4.26}$$

In general, the decrease in performance by the reduction of the kinetic energy at the nozzle exit is somehow less than the heat flux losses. Thus, the following relation is satisfied

$$\dot{m} \left(\frac{v_2^2}{2} - \frac{v_2'^2}{2} \right) < \dot{Q}_w \tag{4.27}$$

where v_2' is the effective exhaust velocity, and v_2 is the ideal exhaust velocity, i.e. without heat losses (seen in the previous sections).

Then, the ratio of the effective exhaust velocity over the ideal exhaust velocity can be obtained by isolating v_2' from the previous relation, and then substituting equation (4.10) and rearranging some terms.

$$\frac{v_2'}{v_2} > \sqrt{1 - \left(\frac{\dot{Q}_w}{\dot{m} c_p T_0} \right) \left(\frac{1}{1 - \left(\frac{P_2}{P_0} \right)^{\frac{\gamma - 1}{\gamma}}} \right)} \tag{4.28}$$

4.5 Structural integrity

The case of a solid propellant rocket motor not only houses the propellant, but acts as the combustion chamber. Therefore, it has to withstand all the mechanical loads produced by the gasses, and the stresses that the high temperatures can generated through the thermal expansion of the components.

Since the structure of the motor is intended to be axysimmetric, as well as the loads applied on it, all the stresses produced are principal stresses and receive the following names in the cylindrical reference system: radial stress (σ_{rr}), hoop (or circumferential) stress ($\sigma_{\theta\theta}$)

and axial (or longitudinal) stress (σ_{zz}). See appendix D for a deeper insight of the elastostatic formulation of the problem, and the stresses and strains involved.

The proper way to design the structure would then be a finite element analysis of the motor geometry that could couple both, the thermal and the mechanical effects of the boundary conditions applied.

Nevertheless, a preliminary design is also required to size some of the components of the motor and to determine other design parameters such as the maximum expected operating pressure. In order to do so, the motor case can be modeled as a cylindrical pressure vessel with closed ends.

If the ratio of the thickness to the internal radius of the cylinder is less than 1/10, then the thin-walled cylinder approximation is reasonable and a simplified membrane theory can be applied. In this case, the hoop and longitudinal stresses are considered to be constant across the wall thickness and so much greater in value than the radial stress that the latter can be neglected.

If, on the contrary, the ratio of the thickness to the internal radius of the cylinder is greater then 1/10, then the thick-walled cylinder approximation is more accurate and the Lamé expressions have to be applied.

A comparison of both models is shown in figure 4.4, where the stress distributions are depicted for the thick-walled cylinder.

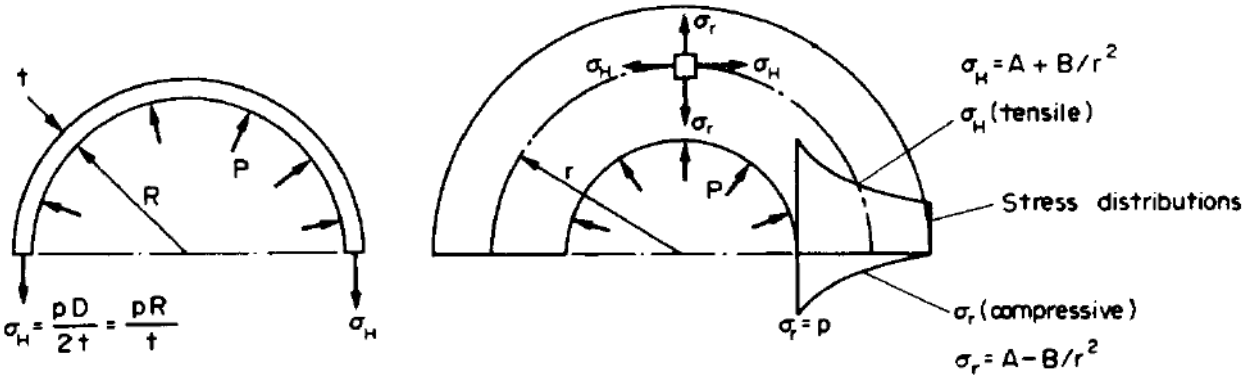

Figure 4.4: Stress distribution of thin (left) and thick (right) walled cylinders with internal pressure load. Source: [12].

4.5.1 Burst pressure

One of the most concerning ways in which the structure could fail is by bursting, i.e., by overcoming the ultimate (or burst) pressure. If that were to happen, the case would collapse and the motor would explode, causing a serious danger for the people around, and the total failure of the rocket.

Therefore, it is important to design the motor case such that the burst pressure is never reached nor exceeded.

This pressure depends on the material properties of the case (i.e., yield strength σ_y and ultimate strength σ_u) as well as its geometry. A simple way to estimate this value is to approximate the case to a cylindrical pressure vessel, either thin or thick walled (depending

on its radius to thickness ratio), and by applying the Svensson's equations [13]:

$$P_u = \sigma_y \psi B_1 \quad \text{(thick cylinders)} \tag{4.29}$$

$$P_u = \frac{\sigma_y}{m} B_3 \quad \text{(thin cylinders)} \tag{4.30}$$

where B_1 and B_3 are burst factors that depend on the strength ratio $\beta \equiv \sigma_y/\sigma_u$, m is the radius/thickness ratio, and ψ is a geometrical factor that depends on m.

Huston and Josephs [13], also provide the relations between the burst factors and the strength ratio (see figure 4.5), as well as the relation between the geometry factor and the radius to thickness ratio (see figure 4.6).

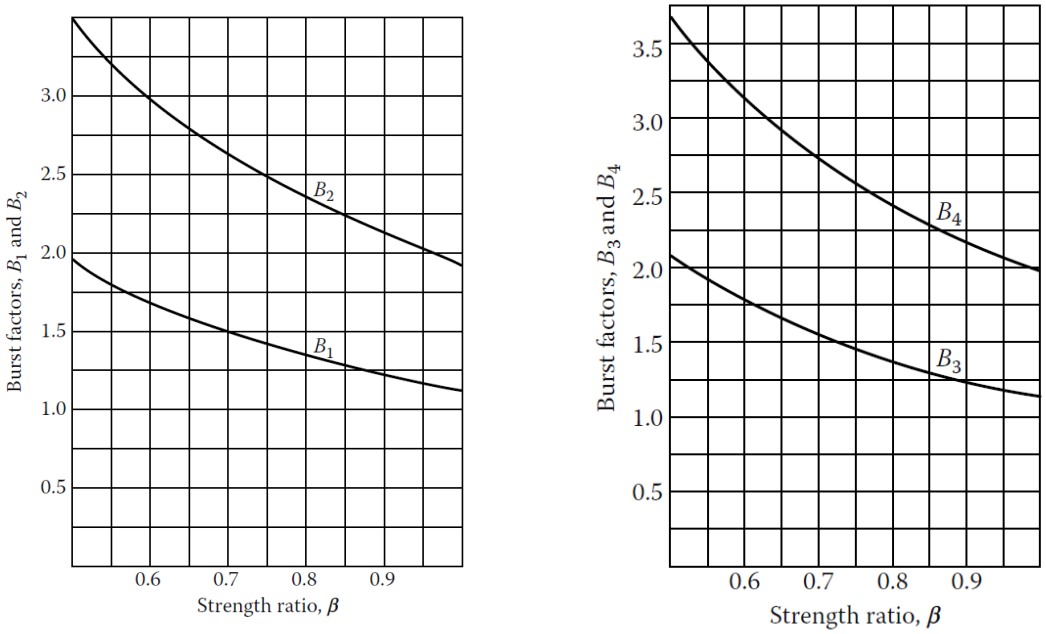

Figure 4.5: Burst factors of thick (left) and thin (right) cylinders and spheres as a function of the strength ratio. Subscripts 1-3 refer to cylinders, and 2-4 refer to spheres. Source: [13].

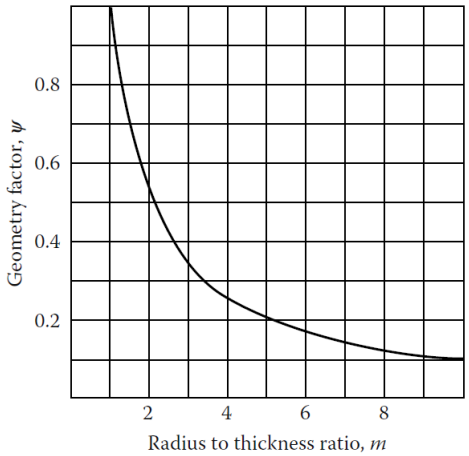

Figure 4.6: Geometry factor for thick cylinders and spheres as a function of the strength ratio. Source: [13].

4.5.2 MEOP pressure

Although bursting has to be avoided at all costs, another failure mode that has to be taken into account when designing a reusable motor is the permanent deformation of the structure. This can occur if the yield strength of the case is surpassed.

In this way, the Maximum Expected Operating Pressure (MEOP) is defined as the maximum chamber pressure that the case can withstand before yielding. However, a factor of safety will be included such that if small perturbations of pressure occur near the limit and the threshold is exceeded, the structure does not fail.

The equations employed will vary depending on whether the case can be modeled as a thin or thick-walled cylinder pressure vessel.

If the case can be approximated as a thin-walled cylinder, stresses can be computed from the simplified membrane theory equations [12][3]

$$\sigma_{\theta\theta} = 2\sigma_{zz} = \frac{P_c R}{t} \tag{4.31}$$

where P_c is the chamber pressure, R is the mean radius, and t is the wall thickness.

If the case can be approximated as a tick-walled cylinder, stresses can be computed from the Lamé equations [12]

$$\sigma_{rr} = \frac{R_i^2 P_c - R_o^2 P_a}{R_o^2 - R_i^2} - \frac{(P_c - P_a) R_i^2 R_o^2}{r^2 (R_o^2 - R_i^2)} \tag{4.32}$$

$$\sigma_{\theta\theta} = \frac{R_i^2 P_c - R_o^2 P_a}{R_o^2 - R_i^2} + \frac{(P_c - P_a) R_i^2 R_o^2}{r^2 (R_o^2 - R_i^2)} \tag{4.33}$$

$$\sigma_{zz} = \frac{R_i^2 P_c - R_o^2 P_a}{R_o^2 - R_i^2} \tag{4.34}$$

where R_i is the inner radius, R_o is the outer radius, and P_a is the ambient pressure.

The yield criterion that will be used to compute the design pressure is the Von Mises stress, which has the following expression

$$\sigma_{vm} = \sqrt{\frac{1}{2}\left[(\sigma_{rr} - \sigma_{\theta\theta})^2 + (\sigma_{\theta\theta} - \sigma_{zz})^2 + (\sigma_{zz} - \sigma_{rr})^2\right]} \tag{4.35}$$

By introducing a safety factor and applying the yield criterion to the Von Mises stress expression one gets

$$\sigma_y = \mathrm{SF}_d \sqrt{\frac{1}{2}\left[(\sigma_{rr} - \sigma_{\theta\theta})^2 + (\sigma_{\theta\theta} - \sigma_{zz})^2 + (\sigma_{zz} - \sigma_{rr})^2\right]} \tag{4.36}$$

Chapter 5

Motor preliminary design

At this point of the thesis, the design process is started. The following sections gather all the design steps that have been done in order to fulfill the objectives as well as complying with the requirements.

In this chapter, all the motor components will be presented and sized. Moreover, the selection of the materials used, the propellants chosen, and the assembly mechanism will be covered as well.

5.1 Case sizing

The motor case is the first component to be sized, since is the only one with geometrical constraints (see table 1.4). This component is of major importance because it has to hold everything together, withstand the chamber pressure, and must be reusable several flights without failing.

The three parameters that will define the case are: the outer diameter (D_{case}), the thickness (t_{case}), and the length (L_{case}).

The first parameter, however, is already defined by the requirement GCR-01, which states that the motor case's outer diameter shall be 75 mm.

Regarding the case length, requirement GCR-02 states that it has to be 893 mm at the most, but its final value could be subjected to change depending on the outcomes in further steps of the design process. The way in which the length of the case affects the performance of the motor is that it is directly related to the exposed surface of the propellant (also known as the burning surface), therefore, it is directly related to the amount of thrust generated. As a consequence, the larger the motor, the more thrust it generates for the same diameter. Thus, the case length will be set to 893 mm for now.

The third design parameter of the case is the thickness, which will affect the structural mass, and the maximum pressure to which the motor is allowed to operate at. As seen in the previous chapter, it will also define if the case can be treated as a thick-walled or thin-walled cylinder. For now, it will be set to 5 mm, but could be subjected to change if necessary depending on the analysis' results.

Another key feature of the motor case is the thrust ring. It is a ring-shaped protrusion at the bottom end of the case that is responsible for transmitting the thrust generated by the motor to the rocket structure.

Table 5.1: Summary of the design parameters of the motor case.

Parameter	Value
D_{case}	75 mm
L_{case}	893 mm
t_{case}	5 mm

5.2 Material selection

Selecting the materials for each of the motor components is crucial for the subsequent performance of the motor and the Phobos rocket. The case material directly affects the maximum pressure at which the motor can operate, thus, limiting the thrust that it can generate. Furthermore, as the motor is carried inside the rocket after the burnout, the influence of the material density also plays an important role in the inert mass of the vehicle.

Then, it is important not only that the materials selected have high stiffness but also a low density. In this way, a good parameter to look at when comparing different types of materials or alloys in the aerospace sector is the specific stiffness (E/ρ), which is defined as the Young's modulus over the material density.

Nonetheless, although high stiffness materials are desired, it is crucial to avoid brittle materials such as PVC, ceramics, or some metallic alloys (which also have relevant stiffness values) because of the safety concerns that a motor failure could involve.

Other important features to compare and pay attention to, are the yield and ultimate tensile strength, and the melting temperature. The latter is of major importance at the nozzle, where the combustion gases produce the highest temperatures near the throat.

In terms of cost and manufacture, metallic materials are advantageous. In contrast with composite cases, where mandrels of the same diameter as the case are needed to wind the fibers, metallic cases can be made of cylinders of the desired dimensions already available on the market. Composite cases would also need a special oven to cure the matrix, and proper tools and software to wind the fibers around the mandrel.

Taking into account all that has just been explained, it has been considered that the most suitable type of materials to be used in the motor design are aluminium alloys and steel. Table 5.2 gathers all of the parameters mentioned for some of the most used alloys in the amateur rocketry sector.

As it can be seen, the 6000 series aluminiums are the ones with the lowest densities, and the highest specific stiffness. In addition, from the aluminium alloys presented in the table, those are the ones with the greatest melting temperature with an $80°C$ difference with respect to the 2000 series.

Regarding the 7000 series, although the yield and ultimate strength are significantly superior from the rest of the alloys, its low melting temperature, and the fact that it has the lowest specific stiffness, makes it unsuitable for any component.

The low-carbon steel, though, is the heaviest of the alloys presented but the surprisingly high melting temperature makes this material ideal for the nozzle.

For the case and the forward closure, the 6061-T6 alloy will be employed, since it is more easily machinable, lower cost, has best oxidation resistance, and is more common in the market than the 6082-T6 alloy.

Table 5.2: Comparison of structural material properties.
Sources: <https://www.makeitfrom.com/> and <https://matmatch.com/>.

Material	Density ρ (g/cm^3)	Young's Modulus E (GPa)	Yield Strength σ_y (MPa)	Ultimate Strength σ_u (MPa)	Specific Stiffness E/ρ	Melting Temperature $(°C)$
Aluminium 2024-T6	3.0	71	370	480	23.7	500
Aluminium 6061-T6	2.7	69	270	310	25.6	580
Aluminium 6082-T6	2.7	69	270	310	25.6	580
Aluminium 7075-T6	3.0	70	480	560	23.3	480
Low-Carbon Steel SAE-AISI 1020	7.9	190	380	460	24.1	1420

5.3 Pressure limits

In the previous chapter, the expressions for determining the burst and the MEOP pressures were presented and are now employed for determining such values.

From the values of table 5.1, the radius to thickness ratio (m) of the motor case is found to be

$$m = \frac{r_{case}}{t_{case}} = \frac{37.5}{5} = 6.5 < 10$$

thus, the thick cylinder approximation for the motor casing is acceptable.

The strength ratio (β) can also be determined now that the casing material has been selected, and is equal to

$$\beta = \frac{\sigma_y}{\sigma_u} = \frac{270}{310} = 0.871$$

By introducing those values in figure 4.6 and in the left chart of figure 4.5, respectively, a geometrical factor of 1.265 and a burst factor of 1.255 are obtained.

Now the burst pressure of the motor case can be computed through equation (4.29) as

$$P_u = \sigma_y \psi B_1 = 270 \cdot 1.265 \cdot 1.255 = 428.66 \text{ MPa}$$

while the MEOP, or also called, the design pressure (P_d), can be computed through the Von Mises yield criterion by substituting the Lamé expressions (equations (4.32), (4.33) and (4.34)) into equation (4.36), and isolating the chamber pressure. By taking into account the inner and outer radius of the motor case, an ambient pressure of 101325 Pa, and a safety factor of 1.5, the design pressure becomes

$$P_d = 25.97 \text{ MPa}$$

Since $P_u/P_d = 16.51$, requirement SR-01 (which states that the burst pressure shall be no less than 2 times the MEOP) is met.

Table 5.3: Summary of the pressure limit parameters of the motor case.

m	β	B_1	ψ
6.5	0.871	1.255	1.265
P_d	SF	P_u	P_u/P_d
25.97 MPa	1.5	428.66 MPa	16.51

5.4 Forward closure sizing

The forward closure design has to take into account several things. The first is the assembly between the closure and the casing. As previously seen, there are a few methods to do that but the selected one for this purpose is the radial bolts assembly. It has been chosen because it is more reliable than the snap ring, and simpler, in terms of manufacture, than the threaded closures. Not to mention that the epoxy method has been discarded because of the low reliability that it entails in such a motor.

In order to calculate the number of bolts necessary to subject the closure when the maximum chamber pressure is achieved, the following expression will be employed

$$N_{bolts} \geq \frac{P_d A_{closure}}{\tau_{shear,bolt} A_{bolt}} \tag{5.1}$$

where N_{bolts} is the number of bolts of the joint, $A_{closure}$ is the forward closure surface (equal to the cross-section of the case interior), A_{bolt} is the bolt cross section, and $\tau_{sy,bolt}$ is the bolt yield shear strength.

According to [14], the yield shear strength can be obtained through the tensile yield stress by assuming the following relation

$$\tau_{sy} \cong 0.577 \sigma_{ty}$$

The bolts to be employed are M3 flat head socket screws with chamfered heads, made of alloy steel grade 10.9, thus, complying with requirement MR-02. Those have a proof strength of 830 MPa, a yield stress of 940 MPa, and an tensile strength of 1040 MPa, which, according to the previous relation give a yield shear strength of 542.38 MPa.

The total number of bolts needed would then be

$$N_{bolts} = \frac{25.97 \cdot \pi \left(65/2\right)^2}{542.38 \cdot \pi \left(3/2\right)^2} = 22.48 \longrightarrow 23$$

however, as a safety measure, the total number of bolts to be included in the closure would be

$$N_{bolts} = 24$$

When designing a bolt attachment like this, another failure mode has to be considered, that is the bolt tear out. It can occur if the force that the case is receiving from the bolts is sufficient to tear the bolt ring out of the case by ripping the case material between the fasteners and the case edge. To ensure that this is kept away from happening, the following expression is employed

$$\tau_{shear,case} > \frac{P_d A_{closure}}{N_{bolts}(2 L_{edge} t_{case})} \tag{5.2}$$

where $\tau_{shear,case}$ is the case shear strength, L_{edge} is the shortest distance from the holes to the case edge, and t_{case} is the case thickness.

The shear strength of aluminium 6061-T6 is 210 MPa, and the distance of the holes from the case edge is 6 mm, since [14] recommends to leave a distance of at least twice the hole diameter to prevent tear out.

Then,

$$\frac{25.97 \cdot \pi \left(65/2\right)^2}{24 \cdot (2 \cdot 6 \cdot 5)} = 59.845 \text{ MPa} < 210 \text{ MPa}$$

this amount of shear is far less than the shear strength of the case and, therefore, no tear out is expected.

The second thing to take into account when designing the forward closure is the sealing of the casing. The combustion gases have to be kept inside the chamber, and prevented from escaping through the closure. For this purpose, two COTS Buna-N o-rings will be added to the perimeter of the closure (see dimensions of the rings in table 5.4).

Table 5.4: Geometrical parameters of the o-rings.

Parameter	Value
D_{o-ring}	65.09 mm
d_{o-ring}	60.33 mm
t_{o-ring}	2.62 mm

A cross-section of the forward closure is shown in figure 5.1 to present the current design and its dimensions. Note that the closure has a U-shape instead of a disk shape, because part of the top material, which does not have a clear function, has been deleted in order to reduce inert mass from the vehicle.

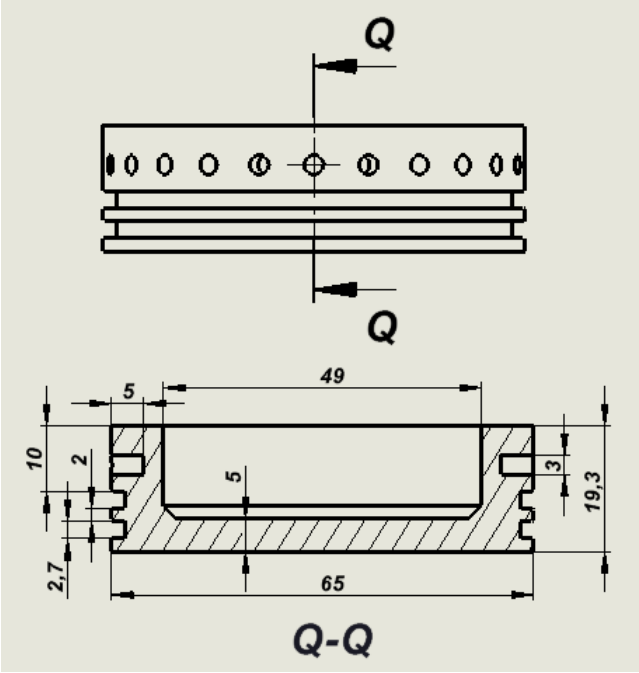

Figure 5.1: Forward closure design.

5.5 Thermal insulation

In rocket science, generally a high chamber temperature is always desired, since its synonym of great performance and elevated thrust. Nevertheless, the heat generated inside the combustion chamber has to be isolated as much as possible from the motor structure, because not only threatens to melt the walls, but also threatens to reduce the yield and ultimate strength of the structure. Of course this would be catastrophic, since the allowable pressure of the casing would be less than the actual chamber pressure.

In order to prevent that, there are three cooling methods to prevent serious structure damage: (1) Heat sink, (2) Insulating materials, (3) Ablative materials.

The first method is seldom used, because it has low reliability as well as low efficiency. The way in which this method works is by making the motor casing so thick that the material itself acts as a heat sink absorbing all the heat from the chamber. This is used in small motors, where the chamber temperatures are rather low and the burning times very short (around 1 s or less). It is not a good option for the motors concerning this thesis, since the combustion temperatures are expected to be at least above 1500 K and also because the case would need to be too thick, thus, increasing the inert mass of the motor.

The second method consists in adding a thermal insulating material (such as cardboard or resin impregnated cardboard), also called liner, between the case and the propellant. This materials shall have a low thermal conductivity so as to reduce the conductive heat flow coming from the chamber and headed to the structure walls. Those can still melt or burn at a certain temperature, therefore, they should be sized with a proper thickness so that enough material remains to isolate during the whole burn.

The third method can be applied at both, the case and the nozzle, and consists in adding a layer of ablative material (such as graphite or phenolic resins) between the flow and the structure. This material then decomposes as the flow erodes it, creating at the same time a protective boundary layer. When this method is applied at the nozzle, it reduces the performance of the motor, since the throat area is reduced by erosion, thus, reducing the chamber pressure and the thrust. Since the idea is to obtain a fully reusable rocket motor, this method will be discarded because it would require a new nozzle insert at each flight.

The method that seems more plausible then is the insulating material. For this case, cardboard will be used, since it has a low thermal conductivity (see table 5.5), is cheap and light, and is the most common type of liner used among amateur rocketeers, i.e., it has been proofed to be reliable. Two thermal insulators will be used: the liner, which will be located between the grain and the case, and the insulation disk, which will be located between the grain and the forward closure. The same material will be used as the casting tube, where the propellant shall be formed and at which will be attached.

The thicknesses used at first will be the ones in table 5.5, which are typically used in COTS motors, but are subjected to change depending on the results of further temperature analysis.

Table 5.5: Summary of the thermal insulation design parameters of the motor case.

Parameter	Value
λ	0.064 $W/(m \cdot K)$
t_{liner}	4.0 mm
t_{disk}	4.0 mm
t_{cast}	1.5 mm

5.6 Propellant selection and characterization

The solid propellant of the rocket motor has to be selected based on different aspects such as toxicity, performance, cost, manufacture, and available information.

In the first place, regarding the manufacturing processes, sugar based propellants have been discarded, since they are heat-cast propellants, i.e., they require an external heat source in order to melt, so that they can be mixed and cast. This is specially dangerous because the auto-ignition temperature could be exceeded during the process and harm the near personal. Other propellants such as PBAN-based, have also been discarded, because this binder cures at high temperatures (around 60ºC) for several days. Therefore, the propellant used in this design shall be able to be formed without the need of external heat sources, and shall cure at room temperature.

With the addition of these requirements, the amount of propellants left to choose is highly restricted. Nevertheless, two types of binders comply with this specifications: Epoxy and Hydroxyl-Terminated Polybutadiene (HTPB).

On the one hand, the epoxy resin can be used as a binder and has the advantage of curing at room temperature, moreover, as it is liquid, it can be cast into a mold at room temperature as well.

On the other hand, HTPB is another binder that can be cured at room temperature. Although it is also liquid, when combined with the oxidizer, the uncured mixture acquires a putty-like consistency, making it impossible to cast, but rather to be packed into the mold, also at room temperature.

Two formulations of propellants for this type of binders have been selected and are presented in tables 5.6 and 5.7, respectively.

Table 5.6: PN/Epoxy/Fe propellant ingredients and proportions.

Ingredient	**% wt**	**Density** $[g/cm^3]$
Potassium Nitrate	68	2.10
Epoxy (West System)	24	1.12
Iron (III) Oxide	8	5.24

Table 5.7: AP/HTPB/Al propellant ingredients and proportions.

Ingredient	**% wt**	**Density** $[g/cm^3]$
Ammonium Perchlorate, 200 μm	75.8	1.95
Hydroxyl-Terminated Polybutadiene	17.0	0.90
Dioctyl Adipate	2.5	0.92
MDI Isocyanate	1.6	1.22
Aluminium Powder	3.0	2.70
Lampblack	0.1	1.76

These two propellants have been selected based on the mentioned criteria and the availability of sufficient data for the study. Note that for example, a formulation of HTPB with

AN would be more beneficial than combining it with AP, because of the presence of polluting HCl molecules in the exhaust. However, not enough information of AN was found.

The first one is the PN/Epoxy/Fe propellant. It is a non-toxic propellant that uses Potassium Nitrate (PN) as the oxidizer, epoxy (and its curing agent) as the binder and fuel, and iron oxide as an additive for burn-rate enhancement. It has a very low amount of ingredients and is quite simple to prepare. Although it is considered to be a mid-range propellant in terms of performance, it has very good mechanical properties, and is very cheap (has a unit cost around 7.10 $\$/kg$ according to Richard Nakka[1]).

The second one is the AP/HTPB/Al propellant. It is also a non-toxic propellant, and in this case uses Ammonium Perchlorate (AP) as the oxidizer. HTPB is used both as fuel and binder, while aluminium powder is used as fuel but also as an additive for burn-rate enhancement. MDI isocyanate is the room temperature curative, and Dioctyl Adipate (DOA) is used as a plasticizer, since the mix would be extremely viscous if not added. Finally, lampblack, which is a fine dust of almost-pure carbon, is used as an opacifier, to make the propellant grain opaque so as to avoid the ultraviolet light of the flame to ignite undesired parts of the grain.

This propellant has a few more ingredients than the other one and, therefore, is slightly more complex to make. However, the cured mix also has good mechanical properties, and it is considered to be a high-performance propellant.

Some properties of the mentioned propellants like density, and the burn-rate coefficients are presented in tables 5.8 and 5.9

For the PN/Epoxy/Fe propellant, the a and n coefficients have been obtained from experimental results developed by Richard Nakka, while the coefficients for the AP/HTPB/Al propellant have been obtained through the following theoretical expressions [15]

$$a = K_1 D^{K_2 + K_3 C} C^{K4 + K_5 D} \tag{5.3}$$

$$n = K_6 + K_7 D + K_8 C \tag{5.4}$$

where D is the AP diameter in μm, C is the AP fractional concentration in weight, and $K_1 - K_8$ are empirical constants (see [15] for further insights on how the AP size and concentration affect the performance of this type of propellants).

The propellant density has been computed by applying the equation

$$\rho_p = \frac{1}{\sum_i^N f_i / \rho_i} \tag{5.5}$$

where ρ_p is the propellant density, N is the amount of ingredients, ρ_i is the i-th ingredient density, and f_i is the i-th ingredient mass fraction.

Table 5.8: PN/Epoxy/Fe propellant properties.
Source: <http://nakka-rocketry.net/rnx_bur.html>.

Property	Value
ρ	1.5418 g/cm^3
a	2.57 $mm/(s \cdot \mathrm{MPa}^n)$
n	0.371

[1]Unit cost extracted from: <http://nakka-rocketry.net/rnx_for.html#Cost>

Table 5.9: AP/HTPB/Al propellant properties.

Property	Value
ρ	1.5879 g/cm^3
a	1.9509 $mm/(s \cdot \text{MPa}^n)$
n	0.6231

The combustion characterization of the selected propellants has been done via the ProPEP 3 software. It is a propellant evaluation program that determines the chemical equilibrium composition for the combustion of the solid propellants. It has a huge database of liquid and solid propellant chemicals that can be inputted through the user interface, as well as the mass fractions of each ingredient, their initial temperature, the chamber pressure, and the nozzle exit pressure.

The software outputs important information regarding the combustion process such as the chamber temperature (T_c), the specific heat ratio (γ), the molecular weight of the mixture (MW), the specific heat at constant pressure of the mixture (C_p), and all the species present in the combustion products with their respective molar quantity.

The results obtained for the two propellants of study are presented in tables from 5.10 to 5.13 (see the output files of the program in appendix E).

By taking a look at those results, one can clearly seen that the AP-base propellant will be much better in performance than the PN-based. This is because, in the first place, the chamber temperature is more than 700 K higher, and, in the second place, the molecular weight of the AP-based propellant is significantly lower (more than 14 g/mol). Thus, from equation (4.10) it is clear that increasing the temperature, and, lowering the molecular weight translate into an exhaust velocity increase, and, therefore, a thrust increase.

Table 5.10: PN/Epoxy/Fe propellant combustion results.

Parameter	Value
T_c	1528 K
γ	1.135
MW	36.019 g/mol
c^*	934,40 m/s

Table 5.11: AP/HTPB/Al propellant combustion results.

Parameter	Value
T_c	2262 K
γ	1.250
MW	21.714 g/mol
c^*	1414.25 m/s

Another important thing to mention is about the condensed species. Both propellants contain species in the form of either liquid droplets, like potassium carbonate, or solid particles, like aluminium and iron oxide. Although a two phase flow study is out of the scope of this project, it is worth noting its implications. The mass fraction of this elements can be computed through the ratio of the mass of the species over the total mass. The mass of the

species is obtained by multiplying the number of mols to the molecular weight of the species.

$$(\text{wt}\%)_{\text{PN/Epoxy/Fe}} = \frac{\text{MW}_{\text{K}_2\text{CO}_3} \cdot n_{\text{K}_2\text{CO}_3} + \text{MW}_{\text{Fe}} \cdot n_{\text{Fe}} + \text{MW}_{\text{FeO}} \cdot n_{\text{FeO}}}{m_p} \times 100 =$$
$$= \frac{138.205 \cdot 0.336 + 55.84 \cdot 0.0691 + 71.84 \cdot 0.0311}{100} \times 100 = 52.5\%$$

$$(\text{wt}\%)_{\text{AP/HTPB/Al}} = \frac{\text{MW}_{\text{Al}_2\text{O}_3} \cdot n_{\text{Al}_2\text{O}_3}}{m_p} \times 100 = \frac{101.961 \cdot 0.0554}{100} \times 100 = 5.6\%$$

One can see that in the first propellant, the condensed species represent the 52.5% in mass of the combustion products, whereas for the second propellant those just represent the 5.6%. As the reader can imagine, the presence of condensed species is undesired, since they can, in the first place, contribute to the erosion of the nozzle walls, in the second place, absorb thermal energy from the flow which diminishes the efficiency of the motor, and in the third place, they are slowed down while traveling downstream and, thus, reducing the exhaust velocity.

Table 5.12: PN/Epoxy/Fe propellant combustion product species obtained via ProPEP 3 software.

Name	**Formula**	**Molar fraction (%)**
Carbon monoxide	CO	30.774
Hydrogen	H_2	23.581
Potassium carbonate	K_2CO_3 (L)	12.089
Nitrogen	N_2	12.072
Water	H_2O	11.295
Carbon dioxide	CO_2	5.461
Iron	Fe (S)	2.488
Iron oxide	FeO (S)	1.120
Methane	CH_4	0.997
Ammonia	NH_3	<0.100
Potassium hydroxide	KHO	<0.100
Hydrogen cyanide	CNH	<0.010
Potassium cyanide	KCN	<0.010
Potassium	K	<0.010
Formaldehyde	CH_2O	<0.010
Ethylene	C_2H_4	<0.001
Isocyanic acid	CNHO	<0.001
Ferrous hydroxide	FeH_2O_2	<0.001
Potassium oxide hydrate	$K_2H_2O_2$	<0.001
Methyl radical	CH_3	<0.001
Atomic hydrogen	H	<0.001

Table 5.13: AP/HTPB/Al propellant combustion product species obtained via ProPEP 3 software.

Name	Formula	Molar fraction (%)
Carbon monoxide	CO	29.061
Hydrogen	H_2	27.524
Water	H_2O	17.629
Hydrogen chloride	HCl	13.974
Nitrogen	N_2	7.123
Carbon dioxide	CO_2	3.421
Aluminium oxide	Al_2O_3 (S)	1.203
Atomic hydrogen	H	<0.100
Ammonia	NH_3	<0.100
Atomic chlorine	Cl	<0.010
Aluminium chloride	$AlCl_3$	<0.010
Hydrogen cyanide	CNH	<0.010
Hydroxyl radical	HO	<0.010
Methane	CH_4	<0.010
Formaldehyde	CH_2O	<0.010
Aluminium dichloride	$AlCl_2$	<0.001
Formyl radical	CHO	<0.001
Isocyanic acid	CNHO	<0.001
Chloroformyl radical	COCl	<0.001
Aluminium monochloride	AlCl	<0.001
Aluminium (III) chloride oxide	AlOCl	<0.001
Chlorine	Cl_2	<0.001
Nitric oxide	NO	<0.001
Methyl radical	CH_3	<0.001
Amino radical	NH_2	<0.001

Both of these propellants will be analyzed and evaluated in terms of performance in further design phases to select the definitive propellant.

5.7 Grain design

Propellant grains can be design with different shape perforations as seen in the previous chapter. Depending on this shape, the exposed propellant surface will vary, and the thrust curve profile will be different for each case. Some propellant designs might then be suitable for one application but undesired for others, therefore, the special features of each application have to be studied to design the most appropriate grain while complying with the requirements imposed.

In this case though, some specifications have to be met. The first is that the Phobos rocket, which will be launched in a 3 m launch rail, shall have a rail departure velocity of at least 30 m/s according to the EuRoC rules [1]. The purpose of this is to ensure a minimum rocket stability and a predictable flight path. Regarding the propellant design, this means that the thrust curve profile of the motor can not be purely progressive, since the initial thrust of the motor would not be enough to permit the rocket achieve the sufficient velocity.

From the opposing point of view, a purely regressive thrust profile is also undesired, since the rapid acceleration of the rocket would generate extreme loads that could damage the airframe structure.

Therefore, the most appropriate thrust curve for the Phobos rocket is a neutral profile. This can be achieved by means of a star perforation, a rod and tube perforation, or through the so called BATES grains. The latter are the best option in this design for several reasons.

On the one hand, both the star, and the rod and tube perforations can be challenging to produce, are prone to leave unburned propellant into the chamber, and the first one disables the option for axisymmetric approximations for further motor analysis.

On the other hand, BATES grains are axisymmetric, leave less unburned propellant in the chamber walls and are more easily manufactured.

The dimensions of the grain such as outer diameter and length are restricted by the space left in the motor case. From the known values of the case diameter and thickness, and the insulator thickness, the grain outer diameter is found to be 54 mm. In terms of length, even though the nozzle is yet to be designed, it will be attached to the case and sealed in the same way as the forward closure, therefore, it is assumed that the nozzle will penetrate inside the case the same length as the closure. By taking this into account and by considering the insulation dick thickness, the total propellant length results in 850.4 mm.

For the inner diameter of the grain, a perforation of 12 mm is initially considered, but prone to change if the burn time is intended to increase or diminish.

Finally, for the number of grains, a good rule of thumb is to make the grain length 1.5 times longer than its outer diameter [4]. The total number of grains that was found to get the length closer to the desired value was 10.

Table 5.14: Summary of the design parameters of the propellant grain.

Parameter	Value
D_{grain}	54 mm
d_{grain}	12 mm
L_{grain}	85.04 mm
N_{grain}	10

5.8 Nozzle sizing

The nozzle is the component of the motor that converts the thermal energy inside the combustion chamber into kinetic energy. The flow inside the nozzle goes from zero to supersonic velocity in a few centimeters and has to withstand the hot temperatures that generate at the walls, specially at the throat. It is the last component to be sized because its geometry depends on the grain design, the propellant, and the maximum chamber pressure.

The design process goes as follows:

First, the burning area of the BATES grain is expressed in terms of the regression variable x, which represents the thickness of the propellant burned at a given time (see figure 5.2).

$$A_b = N_{grain} \cdot \left[\pi (L_{grain} - 2x)(d_{grain} + 2x) + \frac{1}{2}\pi \left(D_{grain}^2 - (d_{grain} + 2x)^2 \right) \right] \tag{5.6}$$

Then, the value of x that maximizes the burning area is computed by differentiating the expression with respect to x, equaling to zero and isolating x.

$$\frac{dA_b}{dx} = \pi N_{grain} \cdot (2L_{grain} - 4d_{grain} - 12x) \tag{5.7}$$

$$\frac{dA_b}{dx} = 0 \longrightarrow x|_{A_{b,max}} = \frac{1}{6}(L_{grain} - 2d_{grain}) \tag{5.8}$$

Then, by substituting the $x|_{A_{b,max}}$ into A_b the maximum burning area is obtained

$$A_{b,max} = \frac{1}{2}\pi N \cdot \left[\frac{1}{3}\left(L_{grain} + d_{grain}\right)^2 + D_{grain}^2\right] = 951.10\ cm^2 \tag{5.9}$$

Figure 5.2: BATES grain regression. Source: [4].

It is important to know the maximum burning surface, since the maximum chamber pressure will be achieved when $A_{b,max}$ is reached.

In this way, the cross-section of the nozzle throat can be determined by applying equation (4.18). In this relation the K_n parameter depends on the chamber pressure (P_c), the characteristic velocity (c^*), the burn-rate coefficients (a, n) and the propellant density (ρ_p). The last three (a, n and ρ_p), can be assumed to remain constant throughout the burn, and c^*, which in turn depends on the combustion temperature (T_c), the specific heat ratio (γ), and the molecular weight of the combustion products (MW), can also be assumed to remain constant. Therefore, the K_n parameter depends upon P_c, and $K_{n,max}$ will be achieved when $P_{c,max}$ is reached, which at the same time will occur at $A_{b,max}$.

This can be summarized in the following expression[2]

$$K_{n,max} = \frac{A_{b,max}}{A_{throat}} \longrightarrow A_{throat} = \frac{A_{b,max}}{K_{n,max}} = \frac{a\rho_p c^*}{P_d^{1-n}} A_{b,max} \tag{5.10}$$

then

$$d_{throat} = 2\sqrt{\frac{A_{throat}}{\pi}} \tag{5.11}$$

The throat diameters for motors loaded with the two different propellants have been computed and are presented in table 5.15.

To size the exit diameter of the nozzle, the motor will be designed to operate at sea level, i.e., the gases will be expanded to an ambient pressure (P_a) of 101325 Pa. The cross-section of the nozzle exit can now be computed by applying equation (5.12) at the exit section.

$$\frac{1}{\varepsilon} = \frac{A_t}{A_e} = \left(\frac{\gamma+1}{2}\right)^{\frac{1}{(\gamma-1)}} \left(\frac{P_a}{P_d}\right)^{\frac{1}{\gamma}} \sqrt{\frac{\gamma+1}{\gamma-1}\left[1 - \left(\frac{P_a}{P_d}\right)^{\frac{(\gamma-1)}{\gamma}}\right]} \tag{5.12}$$

$$A_{exit} = \varepsilon \cdot A_{throat} \tag{5.13}$$

$$d_{exit} = 2\sqrt{\frac{A_{exit}}{\pi}} \tag{5.14}$$

[2]Note that the throat area has been evaluated for the MEOP (P_d).

The exit diameters for the two motors have been computed and are also presented in table 5.15.

The remaining question about the nozzle that arises now is, how will it be shaped, and how long will it be.

The key point in the nozzle design is to obtain a leaving gas flow as axial as possible, since only the axial exhaust velocity contributes to the thrust generation. Therefore, the smaller the exit angle (θ_e), the more efficient the nozzle will be.

In terms of shape, two types of nozzles can be designed: bell-shaped or conical. Bell-shaped nozzles are mostly used in the professional aerospace sector, since they can achieve smaller exit angles than conical, and operate at the same expansion ratio (ε) that a conical nozzle, but with a reduced length (see figure 5.3). However, the drawbacks of bell-shaped nozzles in the amateur sector is that they can be more expensive. Although the material is reduced, it is not the main expense. Considering that the machining time of the component is what will truly end up fixing the cost of the nozzle in this case, a nozzle with an optimized bell contour would require more attention, time, and cost to manufacture properly so as to maintain the efficiency.

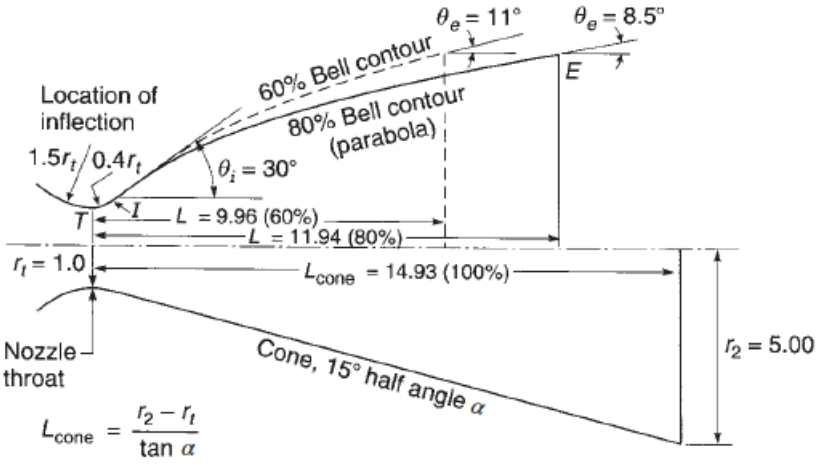

Figure 5.3: Comparison of a 15° conical nozzle with an 80% and 60% of total length bell-shaped nozzles, all with an expansion ratio of 25 : 1. Source: [3].

Therefore, a conical nozzle seems a more interesting option to explore due to its simplicity. These nozzles, nonetheless, have a constant divergence angle (2α), so this means that not all the gases leaving the nozzle will travel parallel to its axis. In fact, a decrease in efficiency is expected to occur, and can be expressed through the following correction factor

$$\lambda = \frac{1 + \cos \alpha}{2} \tag{5.15}$$

Of course, the lower the divergence angle, the higher the efficiency, but also the greater the total length of the nozzle, thus, a trade-off has to be met. This can be seen in figure 5.4, where the correction factor and the nozzle lengths of the two motors have been plotted against the divergence angle.

The half divergence angle chosen for the divergent section is 15°, which is a standard value among amateur rocketeers. It is commonly used because its 98.3% as efficient as an ideal nozzle.

Moreover, if the selected angle was to be, let's say 10°, the efficiency would be increased only a 0.94%, and, more important, the diverging cone length of the AP/HTPB/Al motor would be increased by a 52% with respect to the standard 15° nozzle.

In the contrary, if the selected angle was to be 20° for example, the efficiency would decrease 1.32%, which is significant, while the length would just be reduced by a 26% with respect to the standard 15° nozzle.

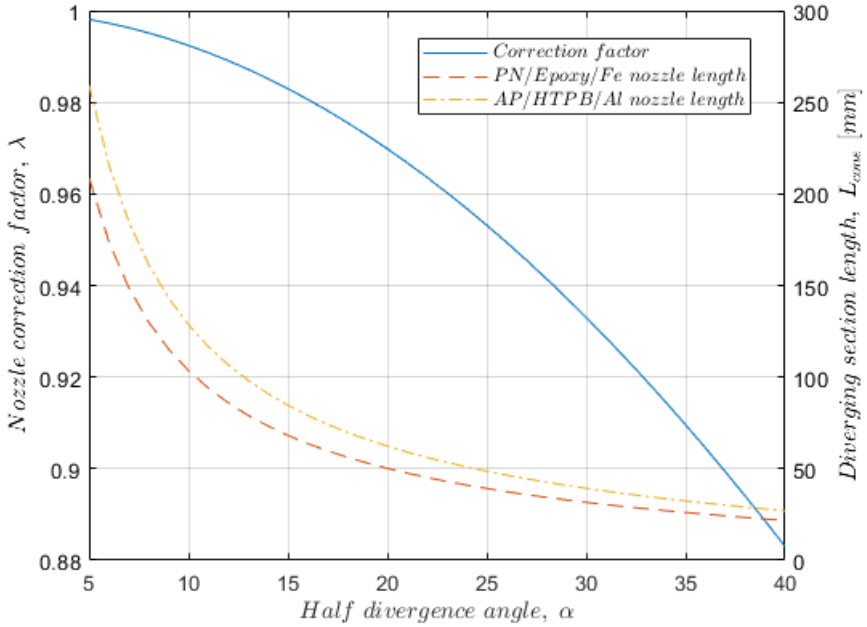

Figure 5.4: Nozzle correction factor and diverging cone length as a function of the half divergence angle.

In regard to the converging, section of the nozzle, the same applies. An optimized curved shape would reduce the turbulence of the flow, thus, making the nozzle more efficient, but the trade-off between cost and efficiency again makes it viable to just simply use a conical section. A typical entrance cone half angle of 45° is often employed [4] and so will be used in this design.

Table 5.15: Summary of the design parameters of the nozzle for the two propellants.

Parameter	**PN/Epoxy/Fe**	**AP/HTPB/Al**
d_{throat}	8.22 mm	12.46 mm
d_{exit}	44.74 mm	57.80 mm
ε	29.6 : 1	21.5 : 1
α_{conv}	45°	45°
α_{div}	15°	15°
L_{cone}	68.15 mm	84.61 mm

Chapter 6

Performance analysis of the proposed solutions

The aim of this section is to evaluate the performance of the preliminary designs in terms of pressure and thrust profiles, peak thrust, specific impulse, etc, and the performance of the Phobos rocket in terms of altitude, with the proposed motors loaded.

6.1 Motor performance analysis

In order to derive the differential equation that describes the chamber pressure variation over time, so that then it can be solved numerically in a Matlab code, a mass balance at the interior of the chamber is done.

$$\dot{m}_p = \dot{m}_c + \dot{m}_n \tag{6.1}$$

where $\dot{m}_p$ is the propellant mass flow rate, $\dot{m}_c$ is the mass rate accumulation inside the combustion chamber, and $\dot{m}_n$ is the mass flow rate leaving through the nozzle.

Recalling chapter 4, the propellant generation mass flow rate, and the nozzle mass flow rate are already known

$$\dot{m}_p = \rho_p A_b r_b \tag{6.2}$$

$$\dot{m}_n = C_d A_t P_c \tag{6.3}$$

where C_d is known as the discharge coefficient

$$C_d = \frac{\gamma}{\sqrt{\gamma R_g T_c}} \left(\frac{2}{\gamma + 1} \right)^{\frac{\gamma+1}{2(\gamma-1)}} = \frac{1}{c^*}$$

Therefore, equation (6.1) can be rewritten as

$$\rho_p A_b r_b = \frac{d}{dt}(\rho_c V_c) + C_d A_t P_c \tag{6.4}$$

where V_c is the chamber free volume (sometimes denoted by V_{free}).

Assuming that the pressure is uniform across the chamber at each time instant, the free-volume changes in the chamber are negligible, the combustion temperature remains constant, as well as the characteristic velocity and the burning-rate, and applying the perfect gas law, the previous equation becomes [16][17]

$$\rho_p A_b r_b = \frac{V_c}{R_g T_c} \frac{dP_c}{dt} + C_d A_t P_c \tag{6.5}$$

Substituting the burn-rate by the model seen in chapter 4 ($r_b = aP_c^n$), and isolating the pressure derivative yields

$$\frac{dP_c}{dt} = \frac{R_g T_c}{V_c}(\rho_p A_b a P_c^n - C_d A_t P_c) \tag{6.6}$$

This is the differential equation that describes the transient performance of the motor. As suggested by Michael A. et al. [18], it will be solved with a fourth-order Runge-Kutta method.

However, this equation only determines the pressure variations inside the chamber until the propellant is burned. The motor depressurization when the propellant has been consumed is known as the tail-off, and references [16] and [17] suggest an exponential relation to compute the pressure until the ambient pressure is reached.

$$P_c = P_{b0} \exp\left[-\frac{R_g T_c A_t}{V_c c^*}(t - t_b)\right] \tag{6.7}$$

where P_{b0} is the chamber pressure at burnout and t_b is the time at which burnout is reached.

The way in which the developed code has been structured is shown in figure 6.1. The user first introduces the input variables, such as grain geometry, propellant properties, ambient pressure, throat area and simulation time step, and then the initial conditions are defined.

Next, the transient simulation initiates a loop in which the program will compute the chamber pressure at each instant until the propellant is consumed.
With the computation of the chamber pressure, the burning-rate can be obtained and, this, allows to compute the regression parameters in the radial (Δx^i) and axial directions (ΔL^i). Then the propellant volume can be evaluated at each iteration until it becomes zero.

Once this happens, the propellant has been consumed and the tail-off loop starts. It then computes the chamber pressure until ambient pressure is reached.
Finally, the program computes the thrust, total impulse, and the specific impulse, based on the obtained data, and plots the results.

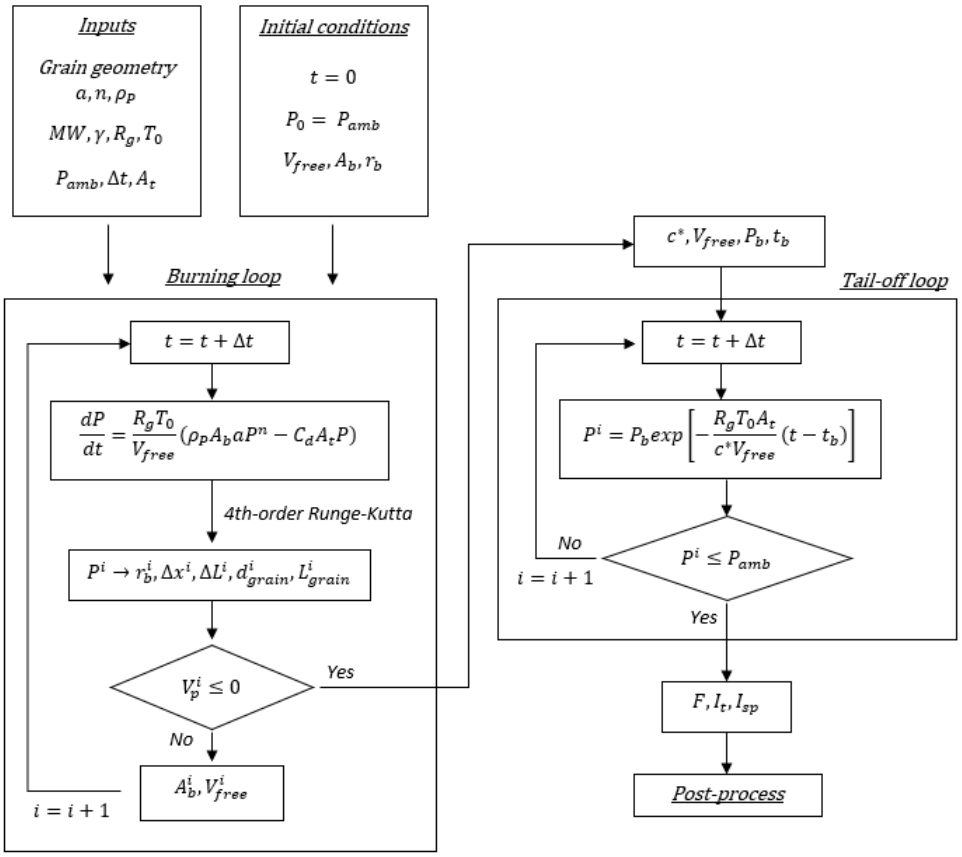

Figure 6.1: Workflow diagram of the motor performance evaluation code developed in Matlab.

In addition, in order to account for real nozzle performance, two correction factors are applied to the exhaust velocity.

The first has been mentioned in previous chapters and is called the divergence correction factor (λ). It takes into account the loss of performance due to the divergence nozzle angle, that is not all the gas particles travels parallel to the nozzle axis when expelled.
The second factor accounts for boundary layer effects, which according to [3], amounts between 0.5% to 1.5% of the losses. A factor of $\xi_{BL} = 0.99$ has been considered.

The results obtained for the two motor alternatives proposed are presented in figures 6.2 and 6.3, and tables 6.1 and 6.2.

Table 6.1: Performance results of the PN/Epoxy/Fe propellant motor.

Specific Impulse, I_{sp}	Total Impulse, I_t	Motor Designation
172 s	5634 $N \cdot s$ (10%M)	$M2108$
Peak Thrust, T_{max}	Average Thrust, $\tilde{T}$	Burn Time, t_b
2458 N	2108 N	2.672 s

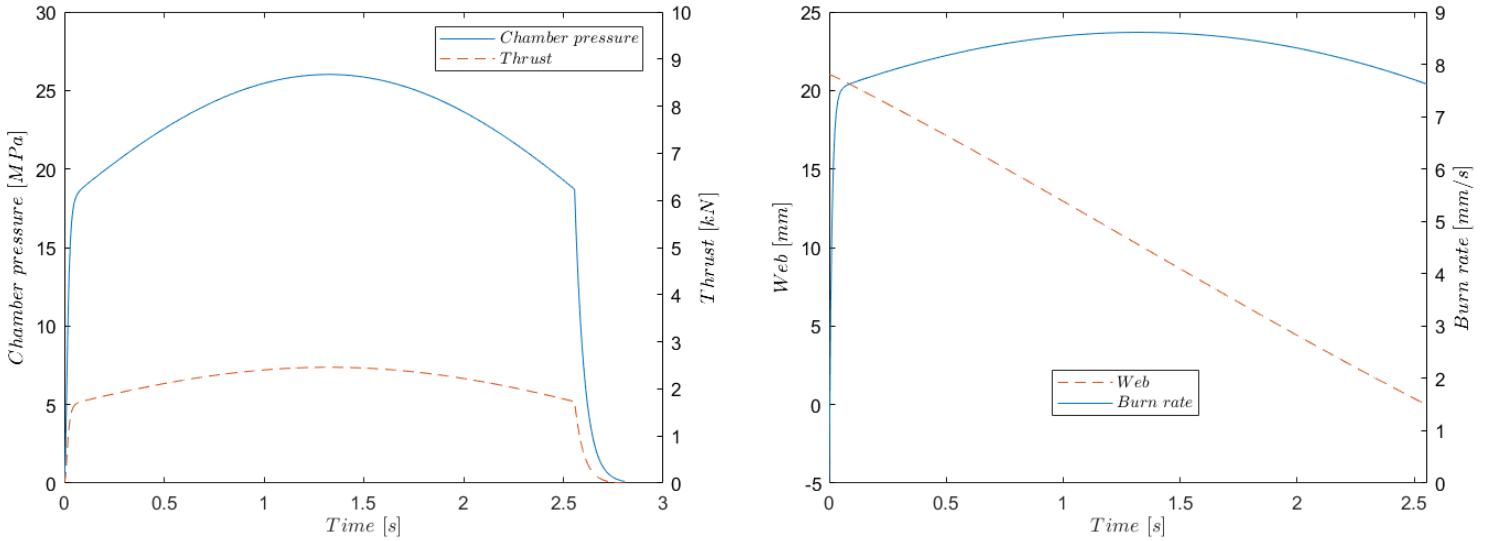

Figure 6.2: Chamber pressure and thrust profiles (left). Web regression and burn-rate over time (right). Results obtained for the PN/Epoxy/Fe propellant motor.

Table 6.2: Performance results of the AP/HTPB/Al propellant motor.

Specific Impulse, I_{sp}	Total Impulse, I_t	Motor Designation
241 s	6956 $N \cdot s$ (35%M)	$M4221$
Peak Thrust, T_{max}	Average Thrust, $\tilde{T}$	Burn Time, t_b
5312 N	4221 N	1.648 s

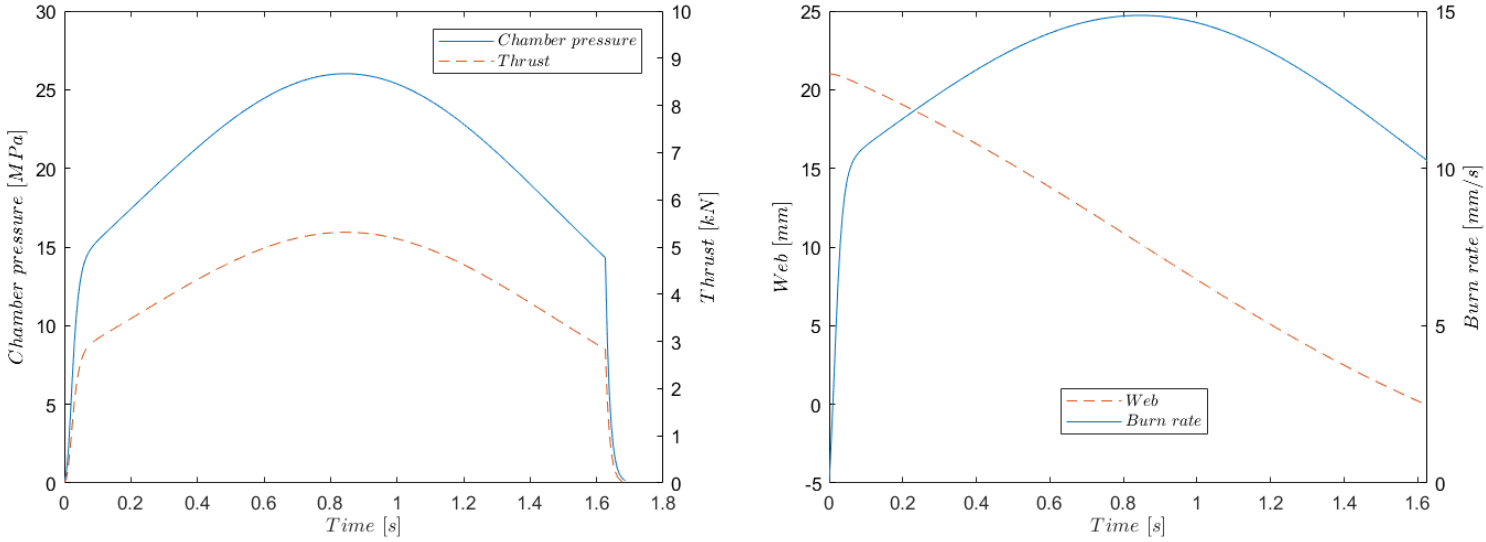

Figure 6.3: Chamber pressure and thrust profiles (left). Web regression and burn-rate over time (right). Results obtained for the AP/HTPB/Al propellant motor.

From this results the following can be identified:

- The PN/Epoxy/Fe propellant motor has an almost neutral thrust curve, while the AP/HTPB/Al propellant motor has a progressive-regressive thrust profile.
- The AP-based propellant motor has a significantly superior specific impulse than the PN-based, therefore, the first is more efficient.
- The PN/Epoxy/Fe propellant motor has a burn-rate that stays around 8 mm/s throughout the burn. This burn-rate is slower than the one from the AP/HTPB/Al propellant motor, which is kept above 10 mm/s. Thus, the total burn time of the first motor is greater (by 1 second).
- The average thrust of the AP-based propellant motor is almost the double of the PN-based propellant motor. This, in conjunction with the burn time, makes the AP/HTPB/Al propellant motor more powerful (25% more in the M category).
- Both motors comply with the PR-01 requirement regarding total impulse.

In order to validate the code and give credibility to the data obtained, the results of one of the motor alternatives (in this case the AP/HTPB/Al propellant) has been compared with the outputs of two different software for the same motor configuration. The programs BurnSim and OpenMotor have been used. Comparison of chamber pressure and thrust curves are presented in figure 6.4.

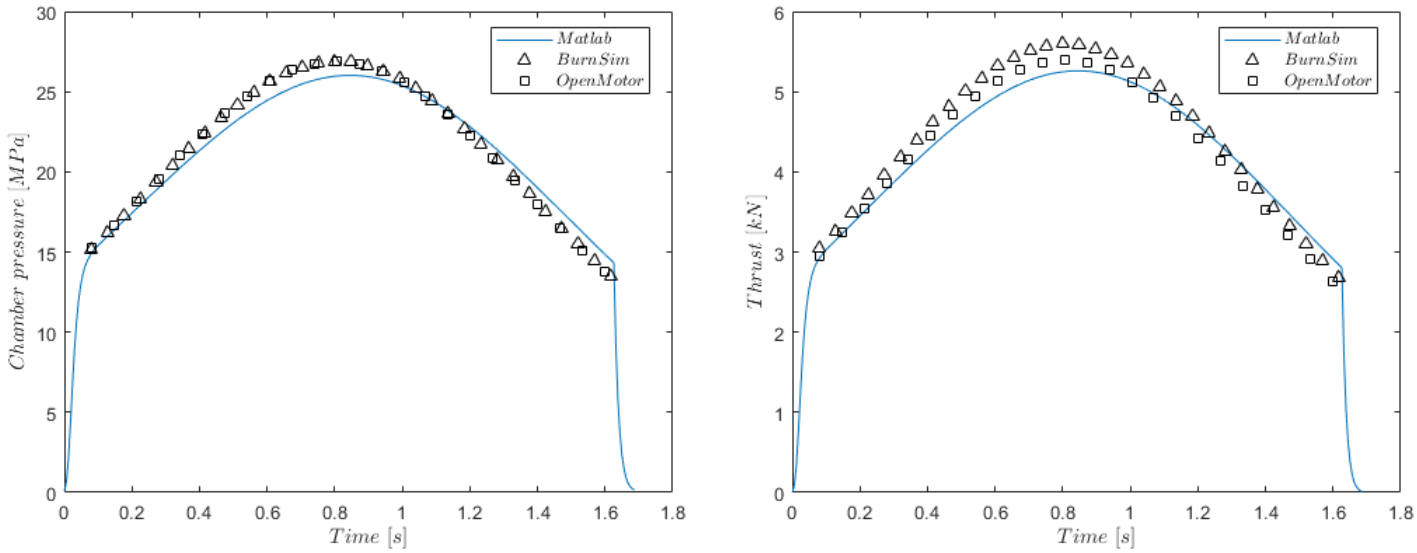

Figure 6.4: Comparison of the AP/HTPB/Al motor performance results obtained through the Matlab code, with respect to the results obtained via BurnSim and OpenMotor.

With respect to BurnSim, the maximum relative error in the chamber pressure computation is 4.6%, and in the thrust computation of 6.1%. Regarding OpenMotor, the maximum relative error in the chamber pressure computation is 5.2%, and in the thrust of 7.7%. The difference in thrust values is explained because of the correction factors employed, since those programs only take into account the divergence correction factor.

Therefore, the values obtained from the Matlab code can be considered to be reasonable.

6.2 Phobos performance analysis

This section gathers the altitude results obtained via the OpenRocket software, in which the Phobos rocket flight is simulated with 6DOF for both motor configurations.

The altitudes reached by the Phobos are presented in figure 6.5. The expected apogee with the PN/Epoxy/Fe propellant motor loaded is of 2677 m, and with the AP/HTPB/Al propellant motor loaded is 3047 m.

Thus, the AP-based motor is the only one from the two that complies with the 3 km altitude requirement (see requirement PR-02). Moreover, it stays pretty close from the altitude objective (within a margin of ± 50 m) and so no other design modification is needed.

In this sense, the AP/HTPB/Al propellant motor will be now subjected to a series of thermal and thermomechanical finite element analysis to refine the design and check for failure modes.

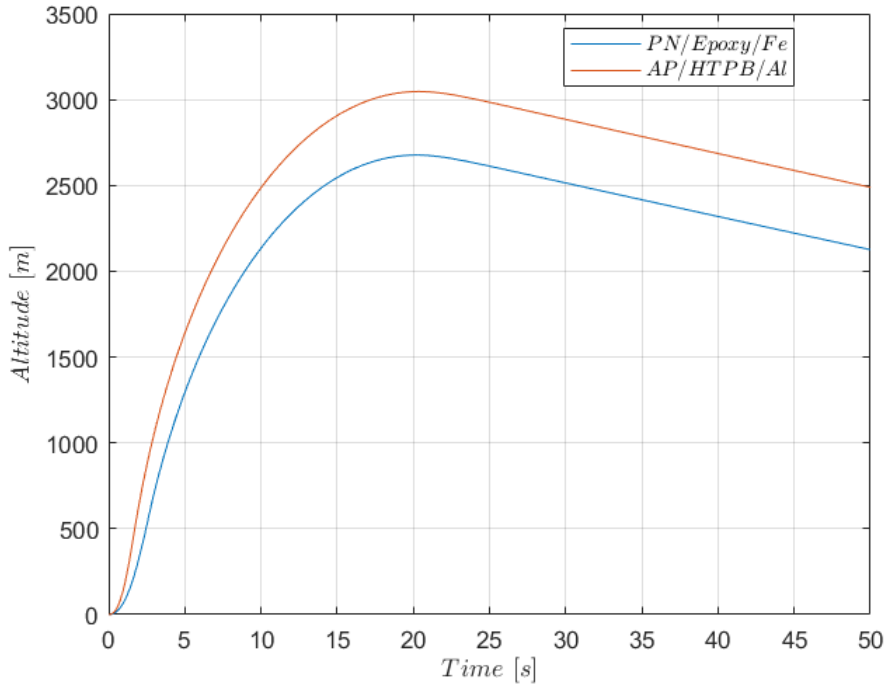

Figure 6.5: Phobos altitude over time for the two propellant configurations with BATES grains.

Chapter 7

Detailed design and analysis of the solution chosen

This is the third and final chapter that covers the design of the solid rocket motor. It provides a more refined design of the motor based on FEA analysis of the structure.

A first set of thermal analysis are performed to obtain the temperature distribution across the motor, check for acceptable temperature values (i.e., no melting temperature is surpassed), and resize the thermal insulators if necessary. Then, a set of thermomechanical analysis is performed to obtain the coupled response of the thermal and the mechanical effects. This is done to check if the structure truly holds the stresses and, therefore, validate the preliminary design, or in the contrary, to adjust the design so that the structure can withstand all the pressure and thermal loads.

7.1 Thermal analysis

For the development of the thermal analysis, the following assumptions have been made:

- 2D axisymmetrical analysis, i.e., the heat flow is considered negligible in the circumferential direction. This is assumed to simplify the analysis and to reduce the computation time. It is acceptable since the geometry and the boundary conditions that will be applied comply with this symmetry.
- Transient analysis. As previously seen in the propellant selection, the flame temperature of the combustion process scales up to 2262 K, which is about a thousand degree less than the surface of the sun, however, the motor reaches burnout in 1.648 s. Thus, the total time of the motor operation is so short that the steady-state is never reached and, therefore, a transient thermal analysis describes more accurately the temperature distribution during the operation time.
- The chamber temperature is assumed constant throughout the motor operation.
- The combustion products composition is assumed to remain unchanged across the nozzle, i.e., the gas is evaluated at frozen conditions.
- The charring and ablation of the insulators is not considered in this analysis.
- On boundary Γ_{h_1}, a forced convective heat transfer process is generated at the interior of the motor case, i.e., at the combustion chamber. See figure 7.1.
- On boundary Γ_{h_2}, a second forced convective heat transfer process is generated at the interior of the nozzle. See figure 7.1.

- On boundary Γ_{h_3}, a natural convective heat transfer process is generated at the exterior of the nozzle. See figure 7.1.
- On boundary Γ_q, the exterior wall of the motor case is assumed to be insulated, since the motor will be covered with an insulating phenolic tube and located inside the rocket motor mount. See figure 7.1.
- The radiation emitted by the exhaust gases is considered negligible with respect to the heat flow generated by convection.
- An initial temperature of 20 $°C$ is set uniformly to all the motor components.

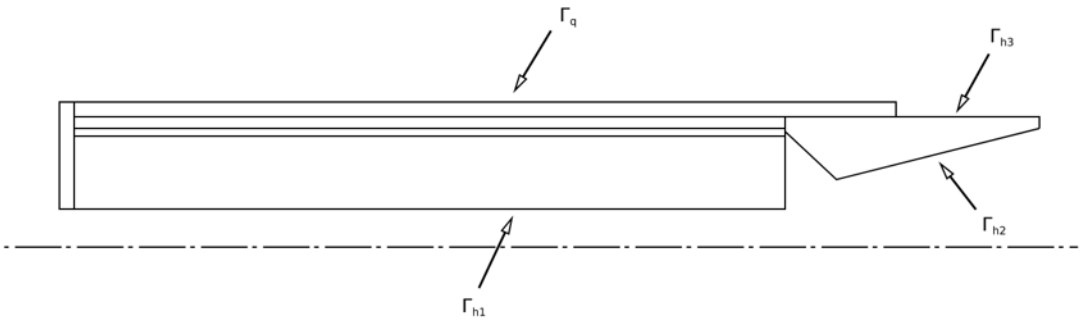

Figure 7.1: Thermal boundaries of a simplified solid rocket motor section.

7.1.1 Geometry

The geometry employed in the thermal analysis is presented in figure 7.2. The drawback of the ANSYS software in thermal analysis is that the geometry has to remain unchanged, i.e., one can not change the geometry throughout the simulation nor either obtain the temperature distribution of one geometry and send it as an input to another slightly different. As a consequence, the propellant geometry can not change during the thermal simulation.

For this first analysis, the geometry used is the one that the motor would have at the time where the maximum chamber pressure is achieved. This is done to determine the temperature distribution at the time where the maximum loads are applied, because the yield and ultimate strengths of the motor case could be reduced by the effect of temperature. So, if the initial geometry, with the propellant unburned was used, the temperature distribution would be somewhat cooler than it would actually be. Then, by using the geometry of that desired instant, the temperatures obtained will be slightly higher than would in fact be, thus, taking in consideration a safety margin. However, as the results will show, the change in the propellant geometry due to its consumption barely affects the temperature distribution of the case.

Note that this change in the propellant geometry only affects the case, since the thickness of material between the gas flow and the case decreases as the burn progresses, whereas in the nozzle the flow is permanently in contact with the steel walls.

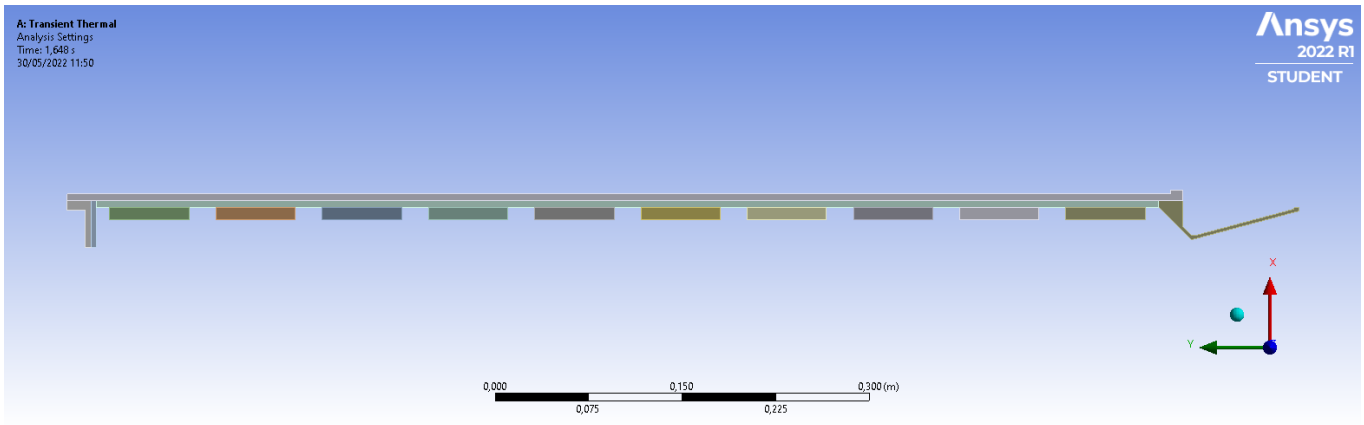

Figure 7.2: 2D axisymmetric geometry of the solid rocket motor employed in the thermal analysis.

7.1.2 Mesh

The mesh utilized is presented in figures 7.3 and 7.4, which show a zoom of the top and bottom ends of the assembly in order to appreciate the mesh. The element size used for the mesh generation is of 1 *mm*, since it is the lowest size that the software allows in the student version. It is worth noting that when possible, the mesh generated has been structured (in the case, insulators and propellant grains), so as to obtain a more precise result, whereas in some regions, like the nozzle and the forward closure, the program couldn't generate a full quadrilateral mesh and, therefore, the mesh is not structured in these components. Nevertheless, the mesh is fine enough to provide precise and representative results.

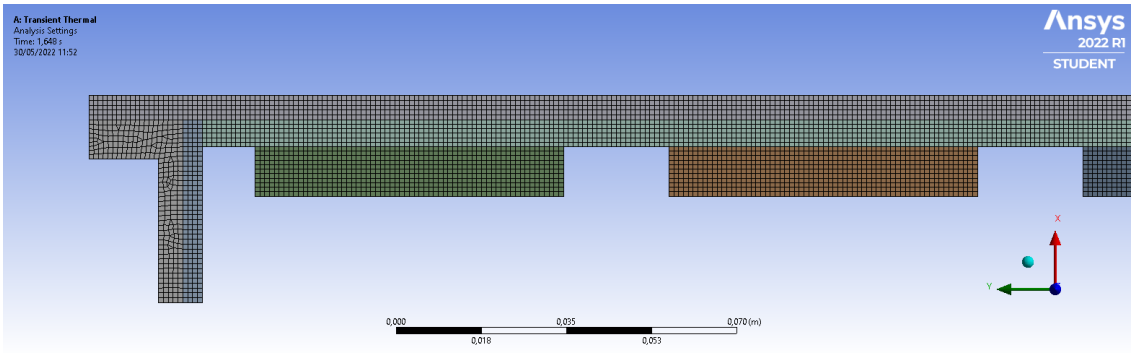

Figure 7.3: Zoom-in view of the top end of the thermal meshed geometry.

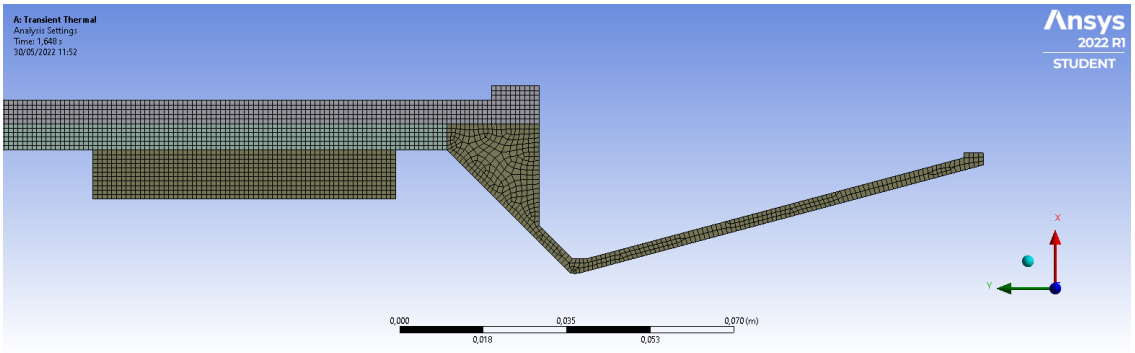

Figure 7.4: Zoom-in view of the bottom end of the thermal meshed geometry.

7.1.3 Boundary conditions

According to appendix B, the governing equation for conductive heat transfer is

$$\rho c_p \frac{\partial T}{\partial t} = \frac{1}{r}\frac{\partial}{\partial r}\left(\lambda r \frac{\partial T}{\partial r}\right) + \frac{\partial}{\partial z}\left(\lambda \frac{\partial T}{\partial z}\right) \tag{7.1}$$

note that the previous assumptions have been applied.

The boundary conditions that apply are the following:

- On boundary Γ_{h_1} (all the surfaces in direct contact with the gas inside the combustion chamber):

$$\dot{q} = h_{g_1}(T_0 - T_w) \tag{7.2}$$

- On boundary Γ_{h_2} (the nozzle inner wall):

$$\dot{q} = h_{g_2}(T_{aw} - T_w) \tag{7.3}$$

- On boundary Γ_{h_3} (the nozzle external wall and the top surfaces of the forward closure):

$$\dot{q} = h_{g_3}(T_w - T_{amb}) \tag{7.4}$$

- On boundary Γ_q (the external surfaces of the motor case):

$$\dot{q} = 0 \tag{7.5}$$

Here, h_{g_1}, h_{g_2} and h_{g_3} are the convective heat transfer coefficients, T_0 is the chamber temperature (also called flame or stagnation temperature), T_w is the wall temperature, T_{aw} is the adiabatic wall temperature, and T_{amb} is the ambient temperature.

The first coefficient (h_{g_1}) has been evaluated through the experimental expression of a gas flowing inside a circular duct (see equation (F.22) in appendix F) for several time instants. The coefficients used are presented in table 7.1.

Table 7.1: Combustion chamber convection coefficients at each time instant.

Δt $[s]$	h_g $[W/(m^2 \cdot K)]$
0.0-0.2	18960.8
0.2-0.4	15029.7
0.4-0.6	10883.3
0.6-0.8	7978.4
0.8-1.0	5397.2
1.0-1.2	4172.2
1.2-1.4	2969.6
1.4-1.648	2063.3

The second coefficient (h_{g_2}) is computed through the semi-empirical Bartz formula (see equation (4.22) in chapter 4). Nevertheless, the term σ of the Bartz relation depends upon the wall temperature, which in turn depends on time. In order to make an estimation of the convective coefficient, reference [11] recommends, based on literature and testing data, to assume an upper and lower bond of 1300 K and 500 K, respectively for the wall temperature.

In fact, this coefficient varies not only on time (since it depends on the chamber pressure) but also at the different nozzle locations (since it also depends on the local cross-section), therefore, it will be computed for different time instants and at several axial locations.

As figure 7.5 shows, the convective coefficients are greater when the wall temperature is lower, because the difference between the gas temperature and the wall is higher, thus, increasing the heat flux. Since the wall temperature remains unknown, the lower bond 500 K will be taken to estimate the coefficients h_{g_2}, as it is the most critical scenario. Figure 7.6 presents the coefficients used in the simulation.

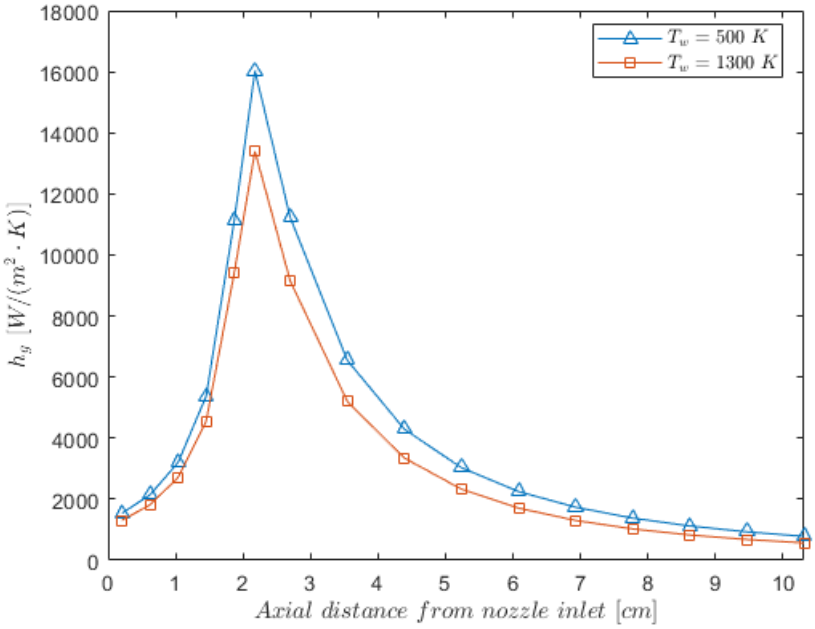

Figure 7.5: Convection coefficients of the nozzle inner wall evaluated at two different wall temperatures for the maximum chamber pressure instant.

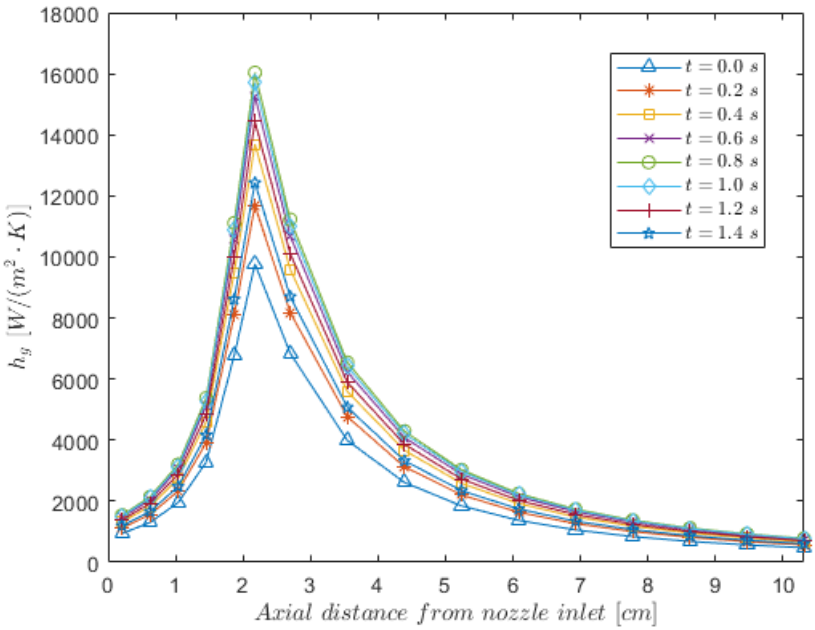

Figure 7.6: Convection coefficients of the nozzle inner wall evaluated at $T_w = 500\ K$ for different time instants.

The third coefficient (h_{g_3}) is also evaluated through an experimental expression. In this case though, the convection over the conical surface of the nozzle exterior wall has been approximated to that of a vertical cylinder with the same mean radius (see equation (F.28) in appendix F). The resultant coefficient is presented in table 7.2.

Table 7.2: Nozzle exterior wall convection coefficient.

$h_g\ [W/(m^2 \cdot K)]$	$T_{amb}\ [°C]$
11.22	20

7.1.4 Results

The temperature distribution obtained from the transient thermal analysis is presented in figures 7.7, 7.8 and 7.9. The first image shows an overall view of the motor, while the second and the third present a zoomed view of the top and bottom ends, respectively. In some regions where the legend becomes unclear, labels of local temperature have been added to facilitate the determination of the temperature.

In addition, a Google Drive folder has been created so as to save all the videos from the transient analysis that will be performed, such that the reader can visualize the distribution variations over time of all the parameters evaluated in the following link: <https://drive.google.com/drive/folders/1WUYYPB3UmCNXoKVB-MouSi8H6mmEnGbZ?usp=sharing>.

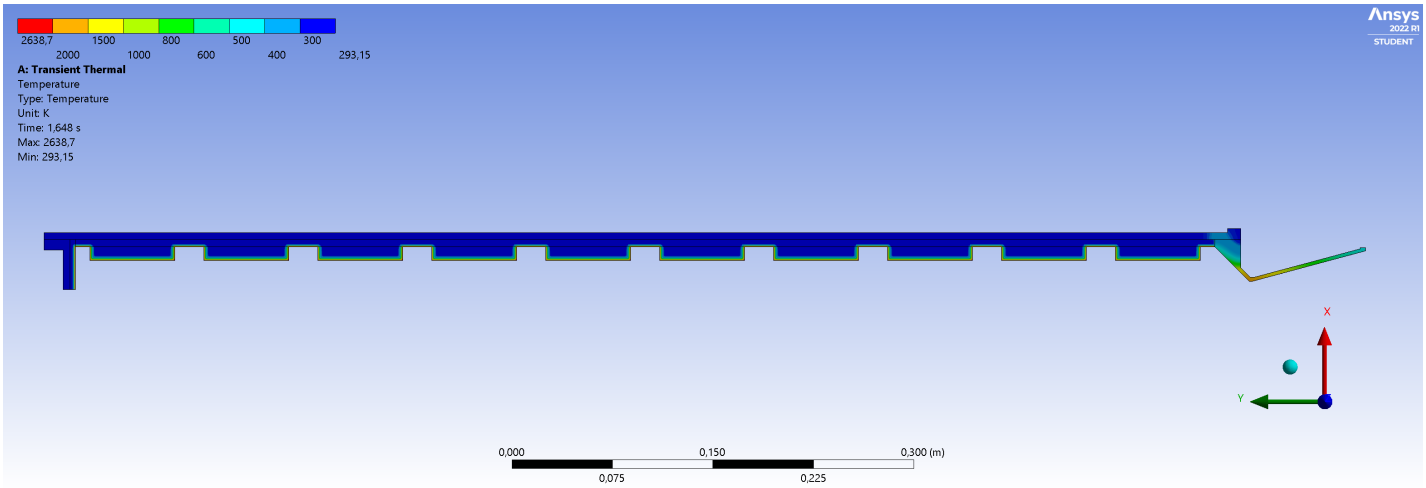

Figure 7.7: Temperature distribution of the solid rocket motor at burnout.

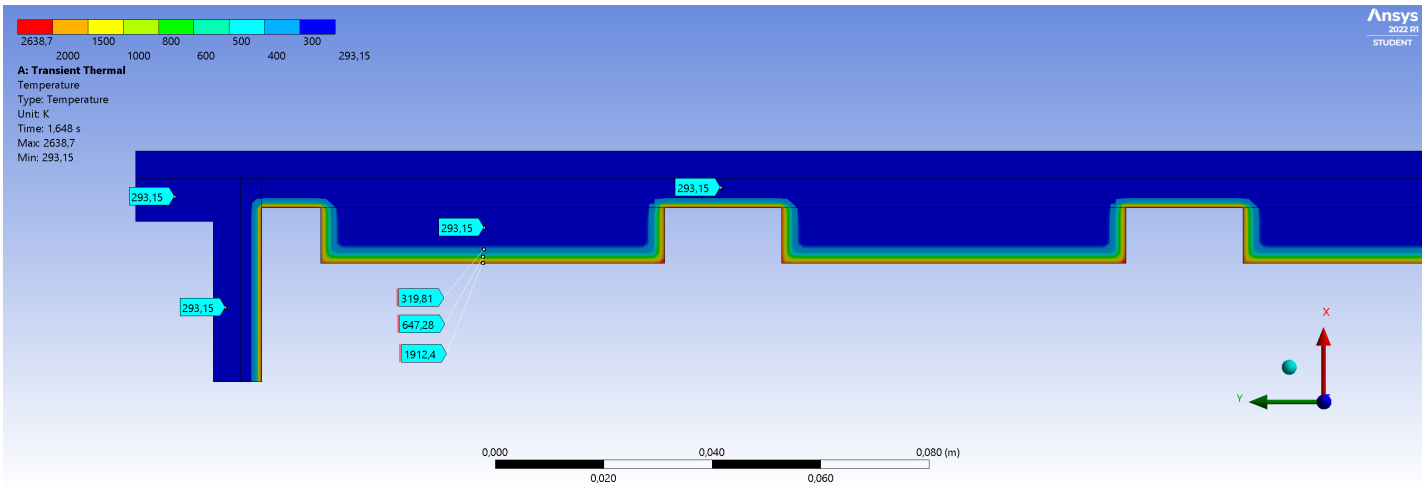

Figure 7.8: Zoom-in view of the top end's temperature distribution at burnout.

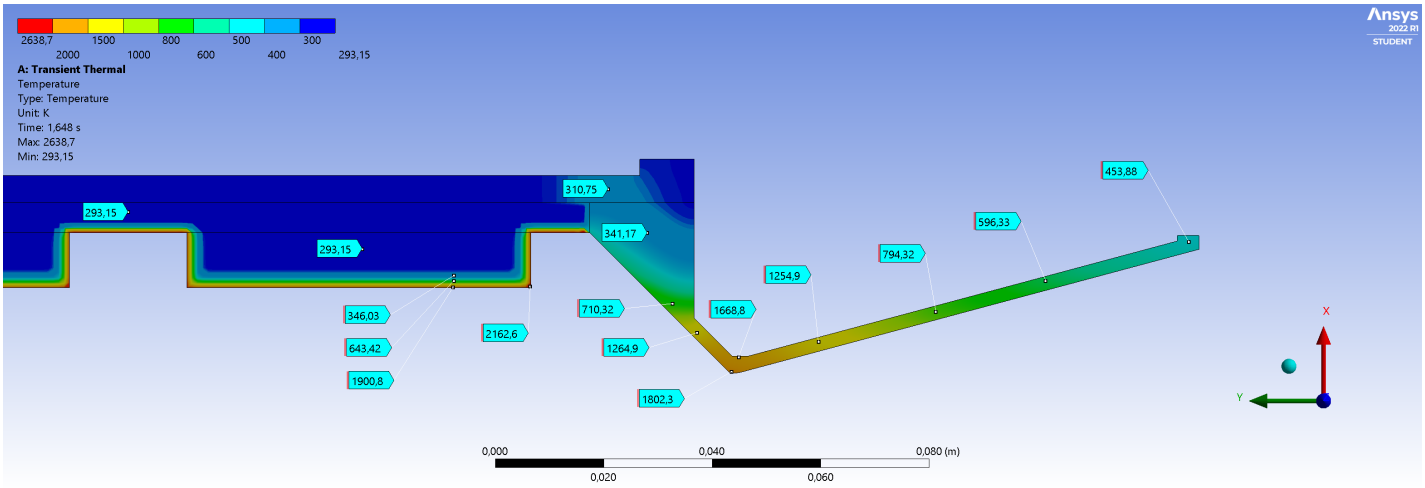

Figure 7.9: Zoom-in view of the bottom end's temperature distribution at burnout.

From this results, several things are deduced:

1. The motor case remains at ambient temperature throughout the full motor operation. Except for the bottom end of the case, where it contacts the nozzle, in which the temperature raises to almost 40 $°C$.

2. The motor case temperature does not depend upon the grain geometry (note that this holds true for the employed liner thickness and burn time). This is clear because even at the regions where the flow is in contact with the insulator, the case remains at ambient temperature.

3. In line with the second commentary, the liner thickness seems to be oversized. This appears to be more obvious in figure 7.10, where the temperature of the liner and the casting tube is plotted across the thickness of the components. As the graphic shows, the temperature drops to 20 $°C$ at about 2 mm from the combustion chamber. Therefore, some insulating material could be eliminated.

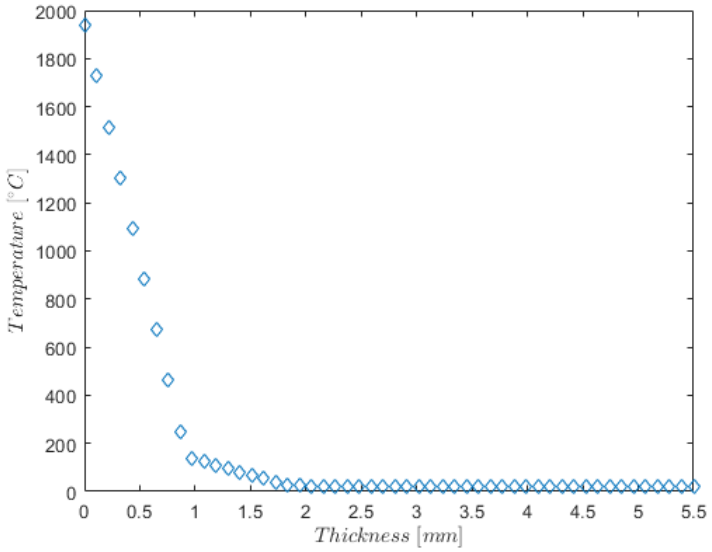

Figure 7.10: Temperature distribution across the insulator thickness (casting tube + liner) at burnout.

4. The most important aspect to remark from the analysis makes reference to the nozzle. The temperature at the throat region and its surroundings exceeds the melting temperature of the low-carbon steel SAE-AISI 1020 ($T_m = 1420\ °C$). This is depicted in figure 7.11, where the temperature of the nozzle inner wall is plotted for different time instants across its length.

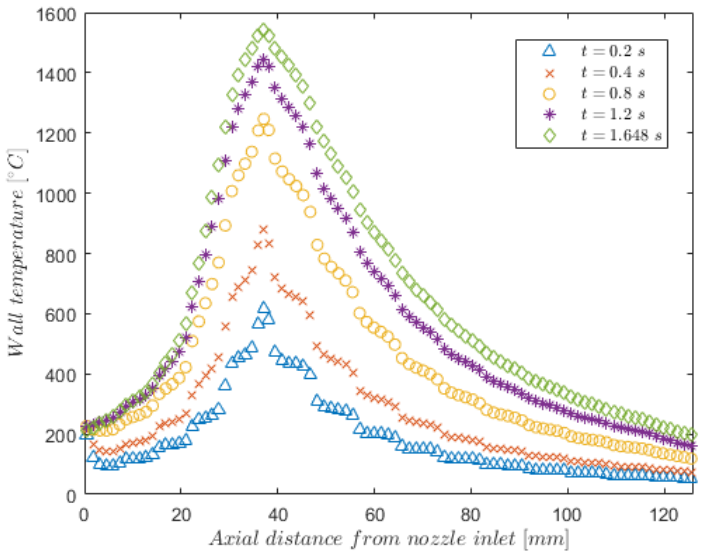

Figure 7.11: Nozzle inner wall temperature distribution across its length at different time instants.

5. Until now, the walls of the nozzle have been considered to be adiabatic, therefore, no heat losses are contemplated. However, in real nozzles this is not true and affects the total performance of the motor. In this analysis, those heat losses that occur at the nozzle walls have been calculated by integrating the mean heat flux along the nozzle inner surface (see figure 7.12). They represent a 1.76% of the total thermal energy of

the flux. This thermal energy that escapes through the walls can not be converted into kinetic energy, thus, produces and effective exhaust velocity that is 98.68% of the exhaust velocity of an ideal nozzle (i.e., without heat losses).

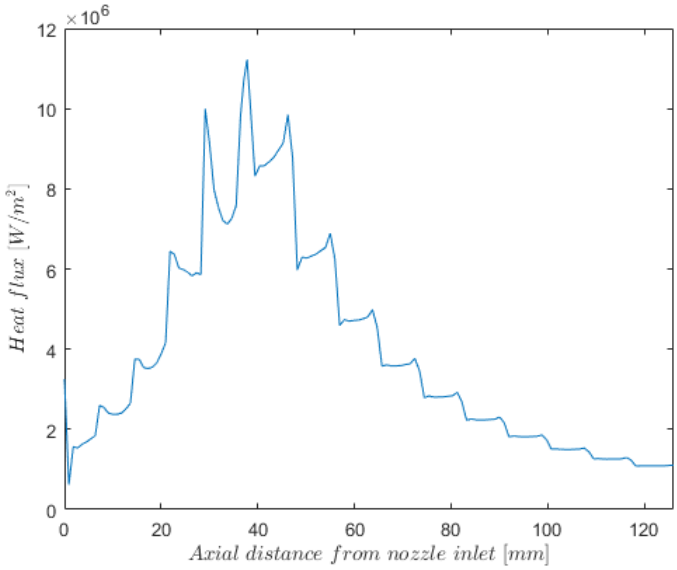

Figure 7.12: Average heat flux distribution at the nozzle inner wall.

7.1.5 Redesign and analysis

From the results obtained in the previous subsection, the motor needs to be redesign in order to comply with the requirements and the objectives of the thesis. Here is where the iterative nature of the design process arises.

In this sense, the issues that have to be resolved are the reduction in thickness of the liner, and the reduction in temperature of the nozzle.

The liner will be reduced 2 mm in thickness due to its oversizing. Although 3.5 mm of the current thickness remains at ambient temperature at the end of operation, only part of this material will be removed so as to keep a margin of safety of material that could burn or end up charring in real operations. This change, however, alters the geometry of the grain, which now will have an outer diameter of 58 mm, and the initial inner diameter of the grain, which now has to be determined again.

To do so, several values have been evaluated for operating conditions as in chapter 6, but now, the reduction in the exhaust velocity due to the thermal losses through the nozzle walls has been considered.

Figure 7.13 presents the altitude of the Phobos rocket for five different grain configurations.

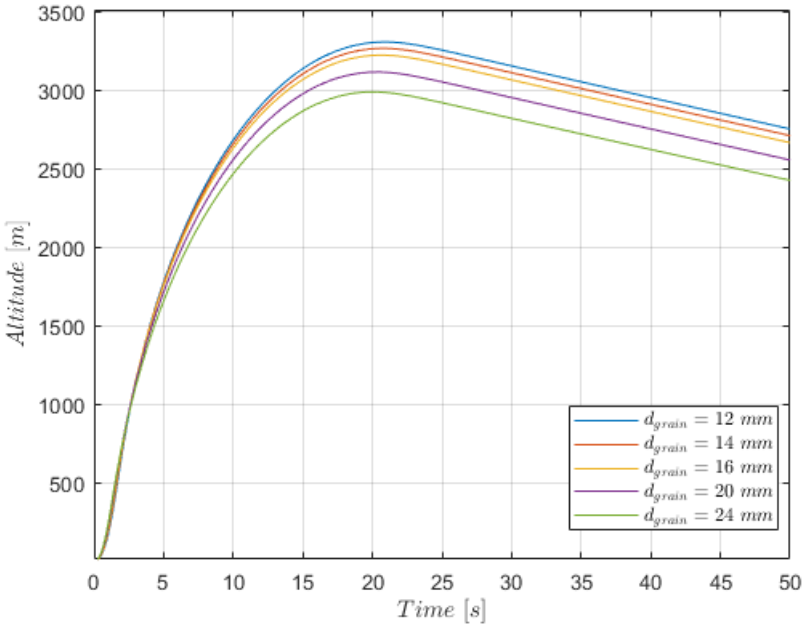

Figure 7.13: Phobos altitude over time for different grain configurations.

The motor configuration that surpasses the 3 km threshold and is closest to it is the one with a grain diameter of 20 mm. This will be the new motor configuration from now on, and the performance values and the nozzle adjustments that arise from this redesign are presented in tables 7.3 and 7.4.

Table 7.3: Motor design parameters that have changed from the previous design.

D_{grain}	t_{liner}	d_{exit}
58 mm	2 mm	62.32 mm
d_{grain}	d_{throat}	ε
20 mm	13.44 mm	21.5 : 1

Table 7.4: Performance results of the resized motor.

Specific Impulse, I_{sp}	Total Impulse, I_t	Motor Designation
236 s	7271 $N \cdot s$ (42%M)	$M5004$
Peak Thrust, T_{max}	Average Thrust, $\tilde{T}$	Burn Time, t_b
6033 N	5004 N	1.453 s

For the nozzle temperature issue, there are some changes that could help to its cooling. The first one would be to create a graphite insert in the throat to prevent the heat from melting the metal material, but as mentioned in other chapters of this thesis, this would not only reduce progressively the performance of the motor due to the throat erosion, but would make the nozzle a single-use component.

The heat sink method would not work in this case though because of the low thermal conductivity of the steel in comparison with other metals, and, in turn, would represent a serious increase in inert mass.

Nonetheless, yet another measure could be implemented to prevent those incredible temperatures to form in the throat. It is the increase in the throat radius of curvature. As seen in equation (4.22), the convection coefficient depends inversely on the radius of curvature,

therefore, a reduction on h_{g_2} would translate into a reduction in the temperatures generated. This can be explained since the radius of curvature acts as an impediment in the gas flow, the lower its value is, the greater the friction is and, thus, the temperature is increased drastically. So by increasing this radius, the flow encounters less obstacles and this friction is reduced.

In order to also facilitate the manufacturing process of the throat, this will be considered to be almost flat by taking a value of $r_c = 50\ m$. The new convective heat transfer coefficients at the nozzle are plotted in figure 7.14.

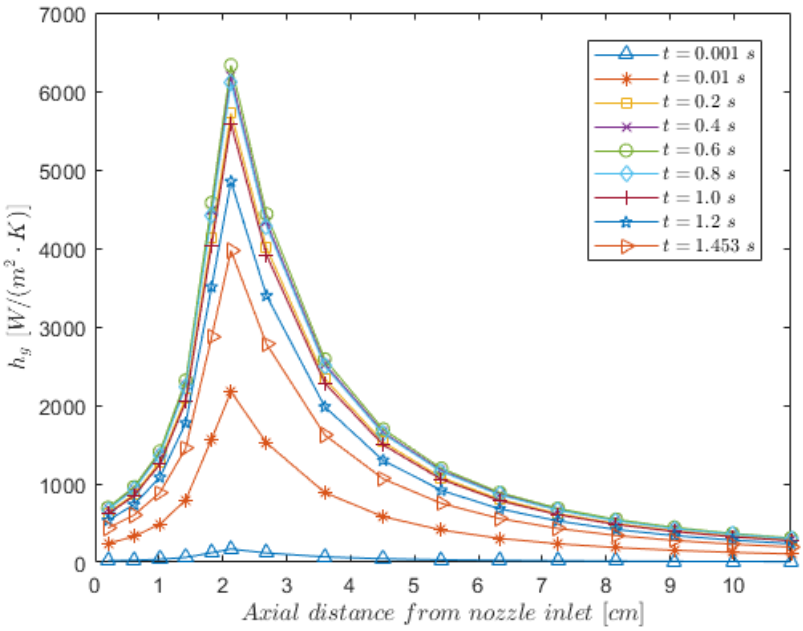

Figure 7.14: Convection coefficients of the resized nozzle inner wall, evaluated at $T_w = 500\ K$ for different time instants.

By applying this changes in the geometry and the boundary conditions, a new thermal analysis has been developed. The results are presented in figures 7.15 and 7.16.

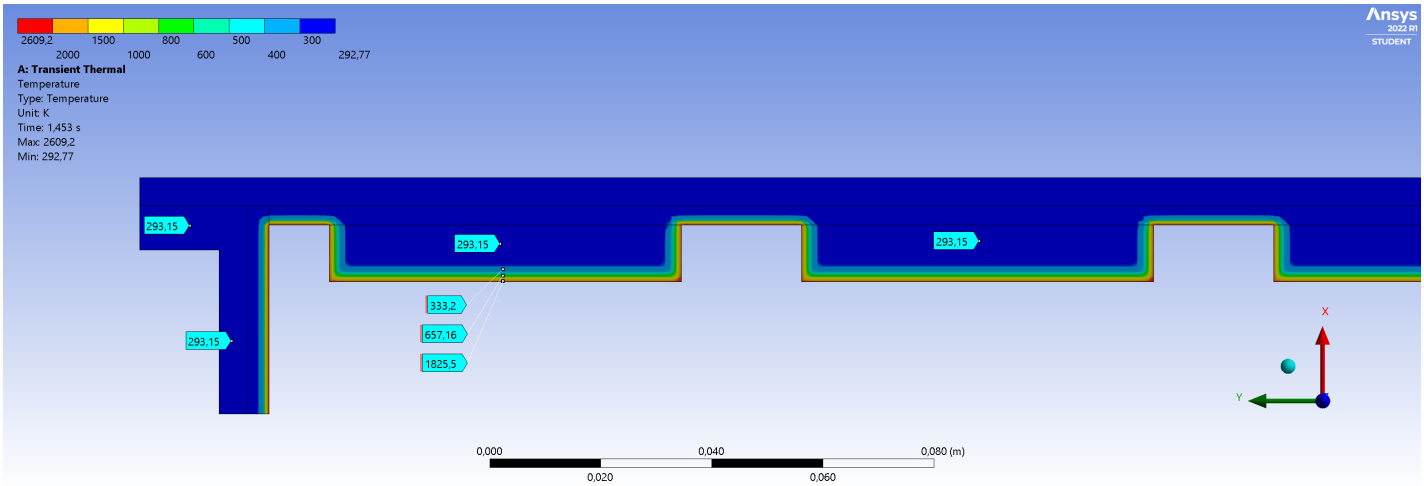

Figure 7.15: Zoom-in view of the top end's temperature distribution at burnout for the resized motor.

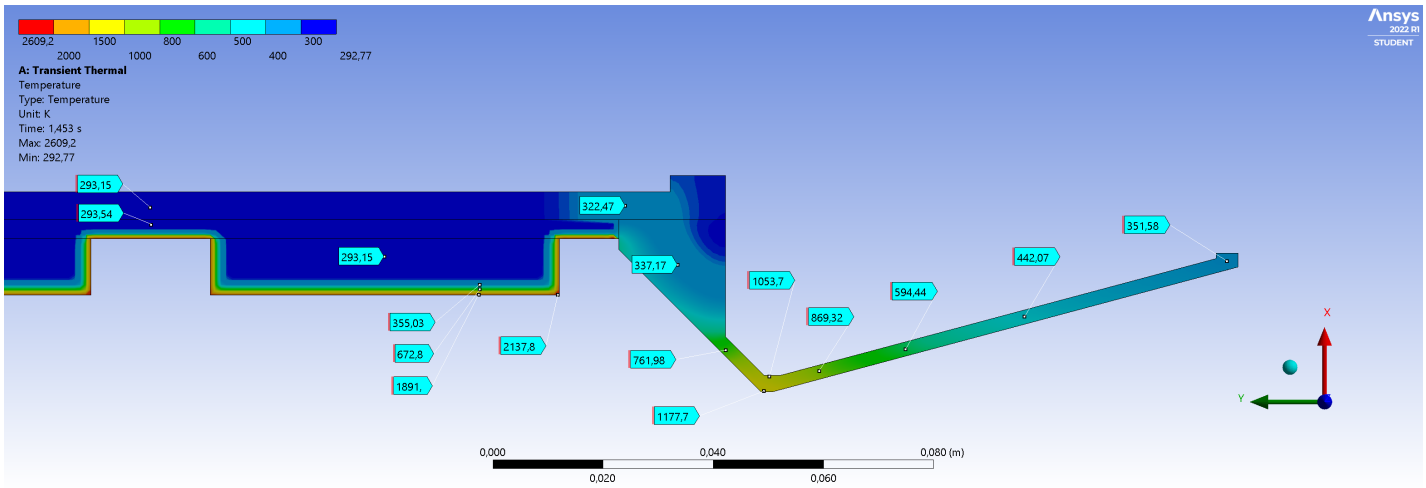

Figure 7.16: Zoom-in view of the bottom end's temperature distribution at burnout for the resized motor.

Again, the motor case temperature is maintained at ambient temperature while the nozzle temperature has been reduced. Figure 7.17 shows the nozzle inner wall temperatures at different time instants. As seen, now when the maximum temperatures are reached, i.e. at burnout, the maximum temperature is kept under melting conditions.

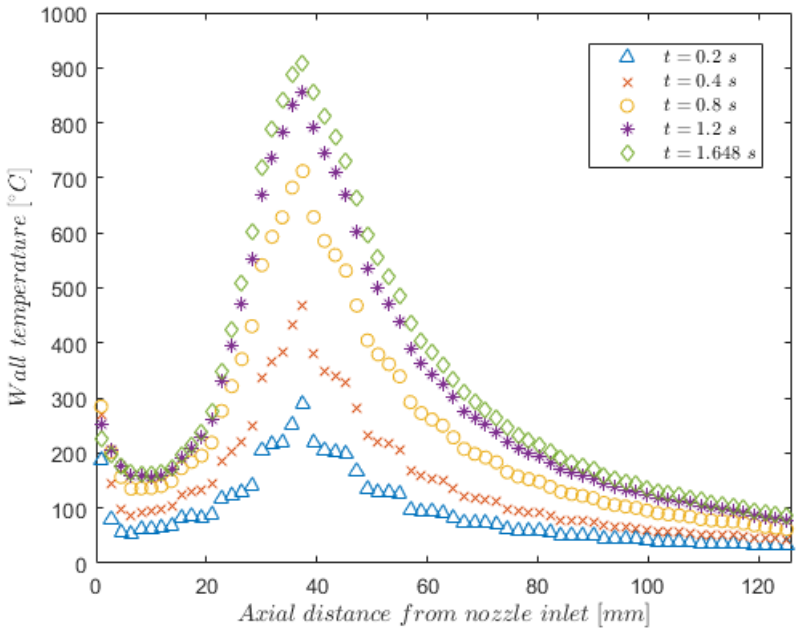

Figure 7.17: Nozzle inner wall temperature distribution across its length at different time instants for the resized motor.

The heat losses through the nozzle walls have also been computed and scale up to 0.69% of the total thermal energy. The effective exhaust velocity, thus, becomes 99.49% of the ideal exhaust velocity (with no heat losses).

7.2 Thermomechanical analysis

The thermomechanical analysis is developed to simulate the response of the motor structure when the pressure and the thermal loads are applied. It is modeled as a coupled effect, since the thermal gradient that generates at the nozzle walls makes the inner surface to expand more than the outer surface, thus, generating extra stresses in that region. The way in which the ANSYS software takes those stresses into account is by an increment in the strain. This is showed in equations (7.6), where the increment in the strain due to a thermal expansion or contraction is represented as the coefficient of thermal expansion (α) times the change in temperature with respect to the reference temperature[1].

$$\varepsilon_{rr} = \frac{1}{E}\left[\sigma_{rr} - \nu\left(\sigma_{\theta\theta} + \sigma_{zz}\right)\right] + \alpha\Delta T \tag{7.6}$$

$$\varepsilon_{\theta\theta} = \frac{1}{E}\left[\sigma_{\theta\theta} - \nu\left(\sigma_{rr} + \sigma_{zz}\right)\right] + \alpha\Delta T \tag{7.7}$$

$$\varepsilon_{zz} = \frac{1}{E}\left[\sigma_{zz} - \nu\left(\sigma_{rr} + \sigma_{\theta\theta}\right)\right] + \alpha\Delta T \tag{7.8}$$

With the development of this analysis, the structure will be studied in more detail than in the preliminary design, where the structural integrity was evaluated with a few analytical expressions. The stresses that are produced in both ends of the motor, which couldn't be computed with precision in chapter 5, will now be known and taken into account in the failure mode evaluation as well.

The assumptions that have been made for the development of the aforementioned analysis are:

- 2D axisymmetric analysis. This is possible since all the loads are axisymmetric. It has been done so as to obtain the temperatures from the previous analysis and, therefore, to give continuity to the thermal analysis.
- Steady-state analysis. Although the stresses of the motor structure vary in time, because the chamber pressure as well as the motor temperature do so, just the most critical instants will be evaluated. Those are the maximum chamber pressure instant, and the maximum nozzle temperature instant. Since each instant will be evaluated separately, the analysis performed will be in steady-state conditions[2]. Nonetheless, the temperature distribution imported for the analysis will be the one reached at that evaluated instant.
- Only the structural components are considered. This has been done to simplify the analysis, since the propellant is considered to be a viscoelastic material and its structural integrity is still a field of study. The structural integrity of the propellant would comprise a whole thesis and because no data was found, it has been decided to be omitted from the analysis.
- Homogeneous and isotropic materials. The materials used (aluminium and steel alloys) are considered to be homogeneous and isotropic, i.e., their properties are the same in each position and direction.

[1] The reference temperature is the temperature where no thermal stresses due to contraction or expansion of the material are considered to be present. In this case, it is considered to be the initial temperature (20 $^{\circ}C$).

[2] A transient structural analysis has been also performed in order to check the validity of this approximation. The results obtained coincide with the ones presented in this chapter, and have been uploaded in the following Drive folder: <https://drive.google.com/drive/folders/1WUYYPB3UmCNXoKVB-MouSi8H6mmEnGbZ?usp=sharing>.

- The chamber pressure is assumed to be uniform in all the positions of the combustion chamber.
- The pressure inside the nozzle is considered to vary isentropically as stated in chapter 4.
- Since the components shall remain in the elastic regime, a linear constitutive model will be used to analyze the response of the structure. This is used as a predictive tool to determine whether or not the plastic and ultimate limits of the materials are exceeded, not to determine the consequences of the structure when it fails.
- The yield and ultimate tensile strengths of the materials are assumed to vary with temperature. This will be taken into account when comparing the Von Mises stresses against the material limits. Figures 7.18 and 7.19 show the percent variation of the yield and ultimate tensile strengths with respect to the same limits at room temperature for several metals.

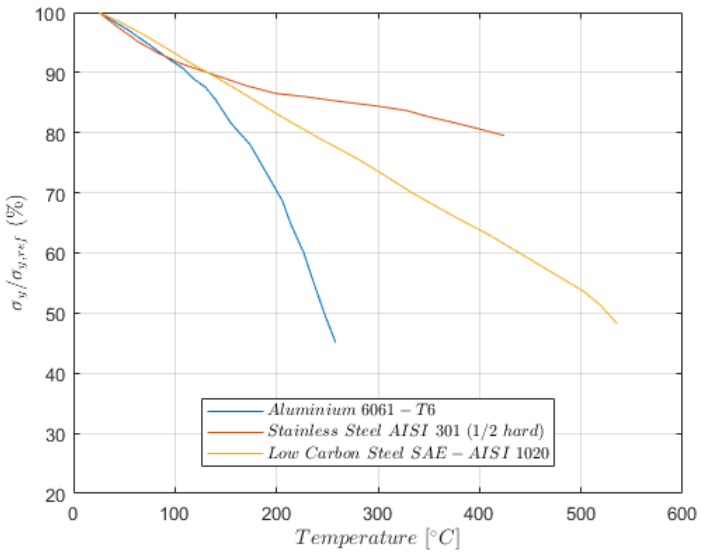

Figure 7.18: Temperature dependence of the yield strength for 1/2 hour exposure on several materials. Source: [5].

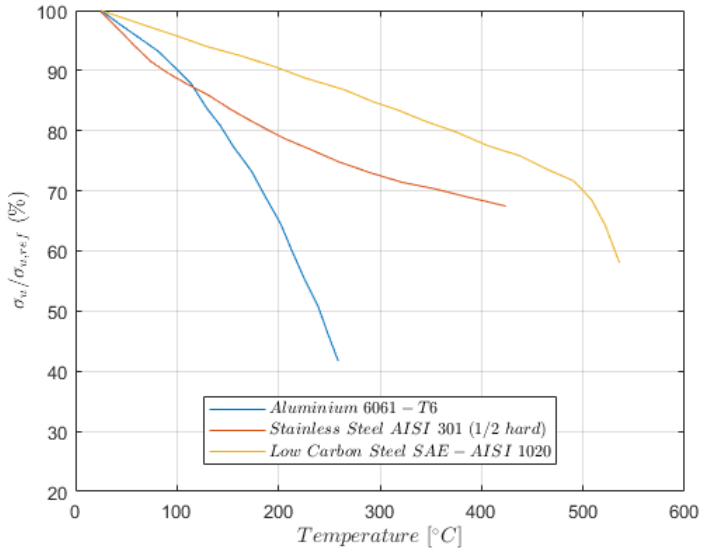

Figure 7.19: Temperature dependence of the ultimate strength for 1/2 hour exposure on several materials. Source: [5].

In reality, the yield and ultimate strength of a material not only depend on temperature, but also on the heating rate, as shown in figures 7.20 and 7.21, where the yield and ultimate tensile strength of a 2024-T3 aluminium alloy are presented for a 30 *min* exposure and a 38 $°C/s$ heating rate. Nonetheless, the lack of information in this sense in notable and this effect won't be considered in the analysis.

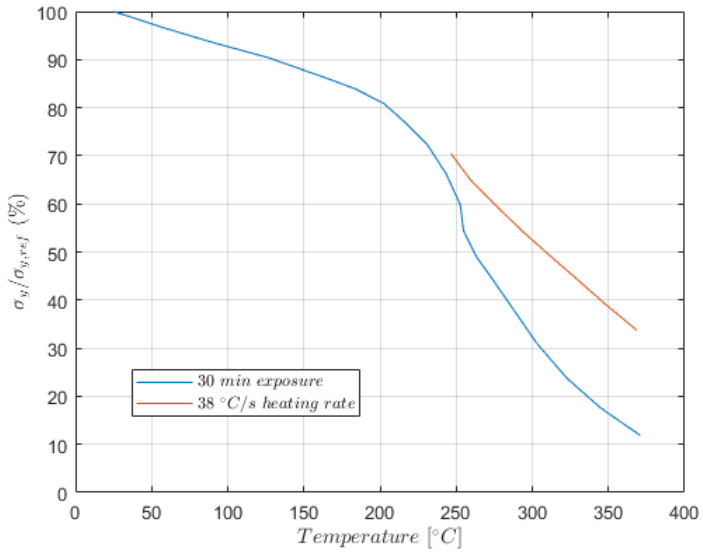

Figure 7.20: Effect of the heating rate on the temperature dependence of the yield strength for a 2024-T3 aluminium. Source: [5].

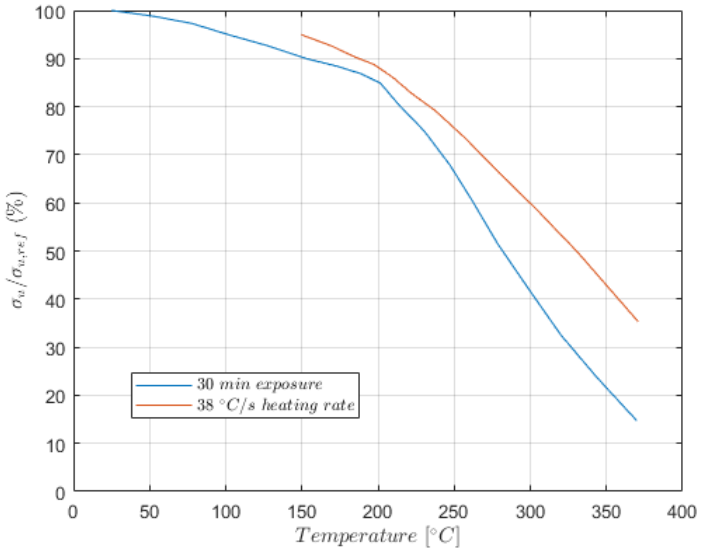

Figure 7.21: Effect of the heating rate on the temperature dependence of the ultimate strength for a 2024-T3 aluminium. Source: [5].

7.2.1 Geometry

As mentioned in the assumptions, the geometry employed consists in the forward closure, the motor case, and the nozzle, see figure 7.22. For simplicity, the bolts have not been modeled, but the contact regions with the case have been set to a bonded condition.

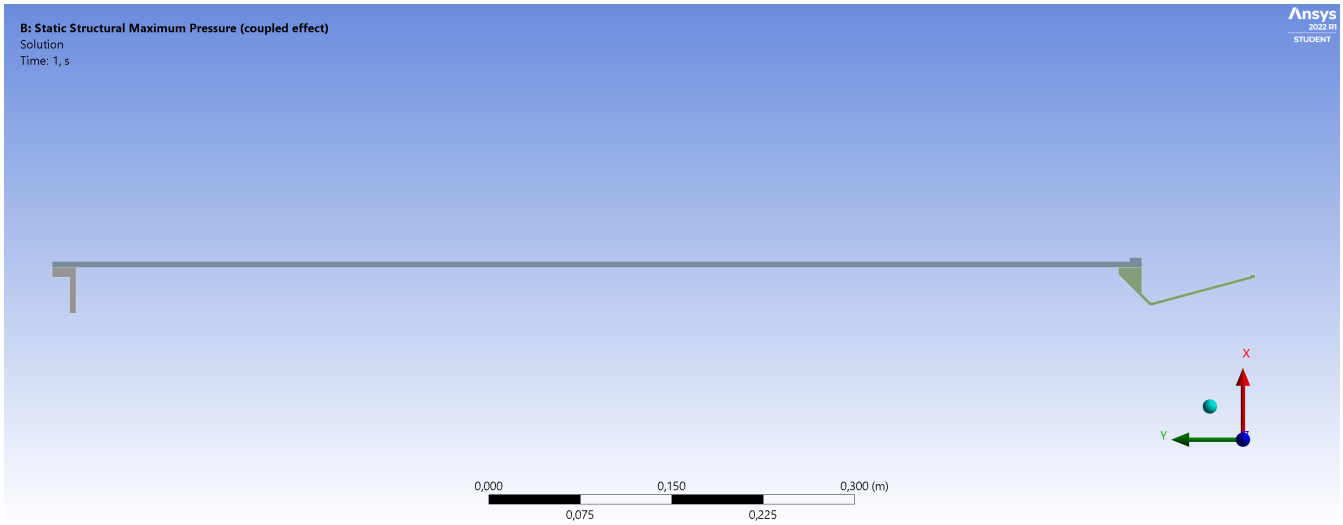

Figure 7.22: 2D axisymmetric geometry of the solid rocket motor employed in the thermomechanical analysis.

7.2.2 Mesh

The mesh employed in the thermomechanical analysis is the same as employed in the thermal. The element size used is again 1 mm, and the mesh is structured in the motor case, while in the forward closure and the nozzle, the mesh is unstructured with quadrilateral dominant elements and some triangular. Figures 7.23 and 7.24 show a detailed view of the meshed components.

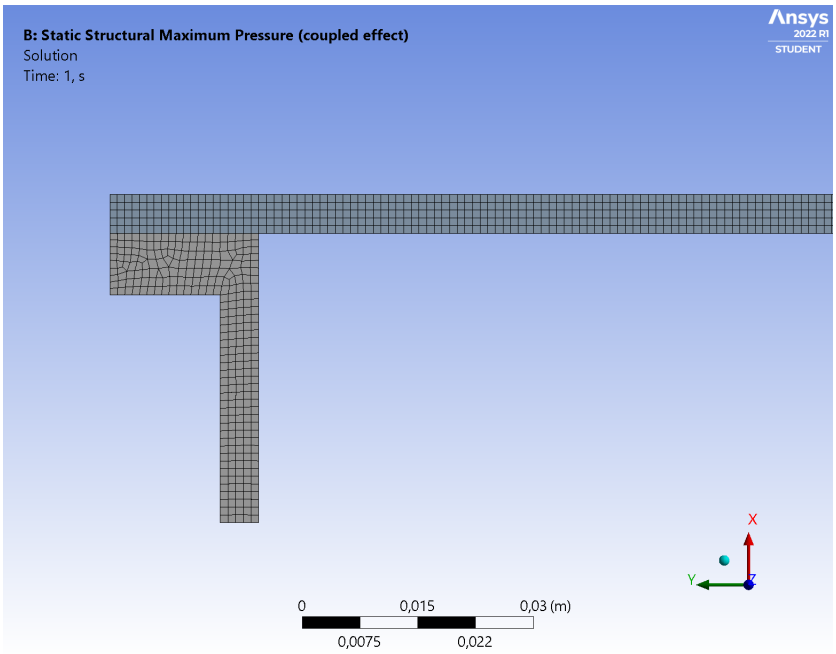

Figure 7.23: Zoom-in view of the top end of the thermomechanical meshed geometry.

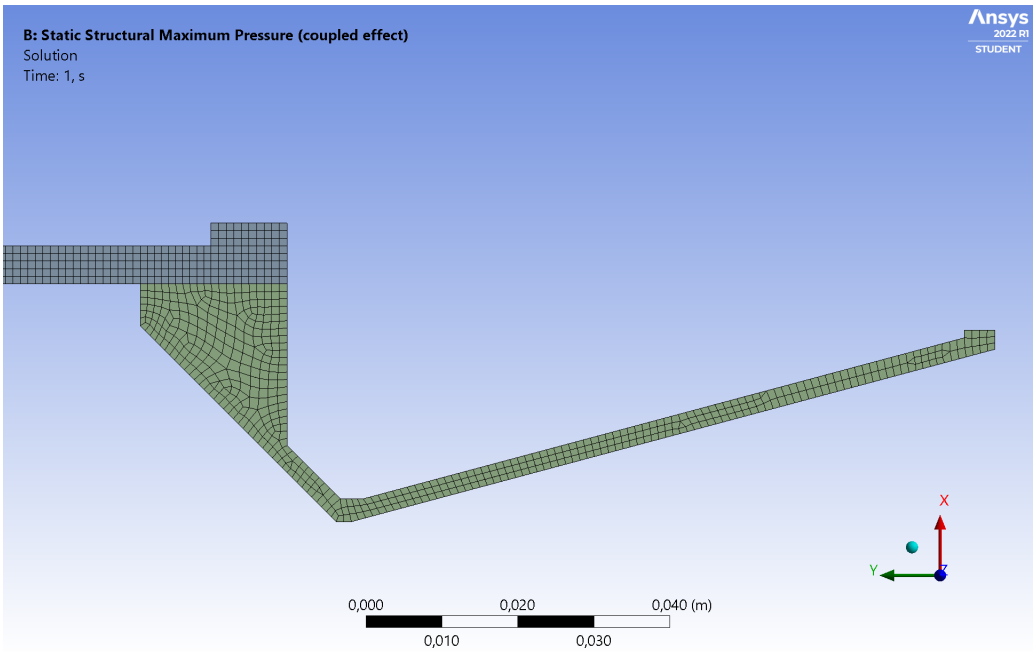

Figure 7.24: Zoom-in view of the bottom end of the thermomechanical meshed geometry.

7.2.3 Boundary conditions

The boundary conditions that apply are the following:

- On boundary Γ_u^i, that is the top surface of the thrust ring, the displacement in the normal direction is restricted:

$$u_i = 0 \ m$$

- On boundary $\Gamma_{\sigma_1}^i$, that is the nozzle external wall and the top surface of the forward closure, ambient pressure is applied:

$$\sigma_{ij} n_{ij} = P_{amb} = 101325 \ Pa$$

- On boundary $\Gamma_{\sigma_2}^i$, that is the combustion chamber surfaces, the chamber pressure is applied:

$$\sigma_{ij} n_{ij} = \max\left[P_{ch}(t)\right] = 26.004 \ MPa$$
$$\sigma_{ij} n_{ij} = P_{ch}(t_{end}) = 14.503 \ MPa$$

- On boundary $\Gamma_{\sigma_3}^i$, that is the inner nozzle walls, an isentropic and axial changing pressure is applied (see figure 7.25):

$$\sigma_{ij} n_{ij} = P(z, t \to P_{ch,max})$$
$$\sigma_{ij} n_{ij} = P(z, t = t_{end})$$

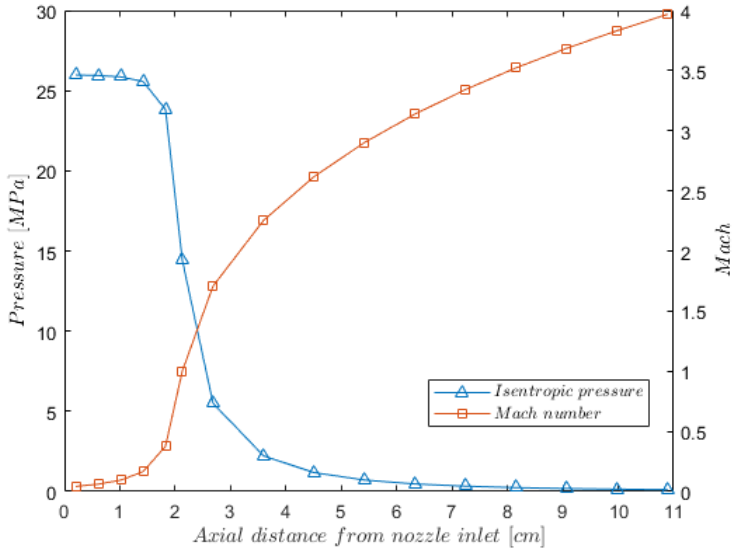

Figure 7.25: Isentropic pressure and Mach number evaluated at several sections of the nozzle for the maximum chamber pressure condition.

7.2.4 Results (maximum chamber pressure)

In this section, the first results to be evaluated will be the Von Mises stresses in the coupled response of the structure, that is by taking into account both, the thermal and mechanical loads. This is done to filter the design proposals that do not comply with the structural integrity requirements. Then, if a proposed solution for the design withstands all the loads with a maximum stress below the yielding limit, the mechanical and thermal effects can be analyzed separately for a better understanding.

The Von Mises stress distribution for the AP/HTPB/Al propellant motor structure is presented in figures 7.26 and 7.27. In those images, a zoomed view of both ends of the structure is presented, since the stress distribution of the case remains constant in the axial direction. A wire-frame of the undeformed structure is also presented.

Several things can be deduced from these results:

First, the motor case withstands all the loads of the combustion chamber, which are basically mechanical loads, since it remains at ambient temperature. It can be seen that the maximum equivalent stress produces at the inner surface and is lower than the yielding limit of 6061-T6 aluminium at ambient temperature.

Second, the forward closure exceeds the ultimate tensile strength in several points, being the stress distribution specially harsh at the center of the component.

Third, the nozzle exceeds by far the ultimate tensile strength of the SAE-AISI 1020 low-carbon steel at the inlet region.

Forth, the ultimate tensile strength of the nozzle steel is also reached and exceeded in the thinner region of the converging section.

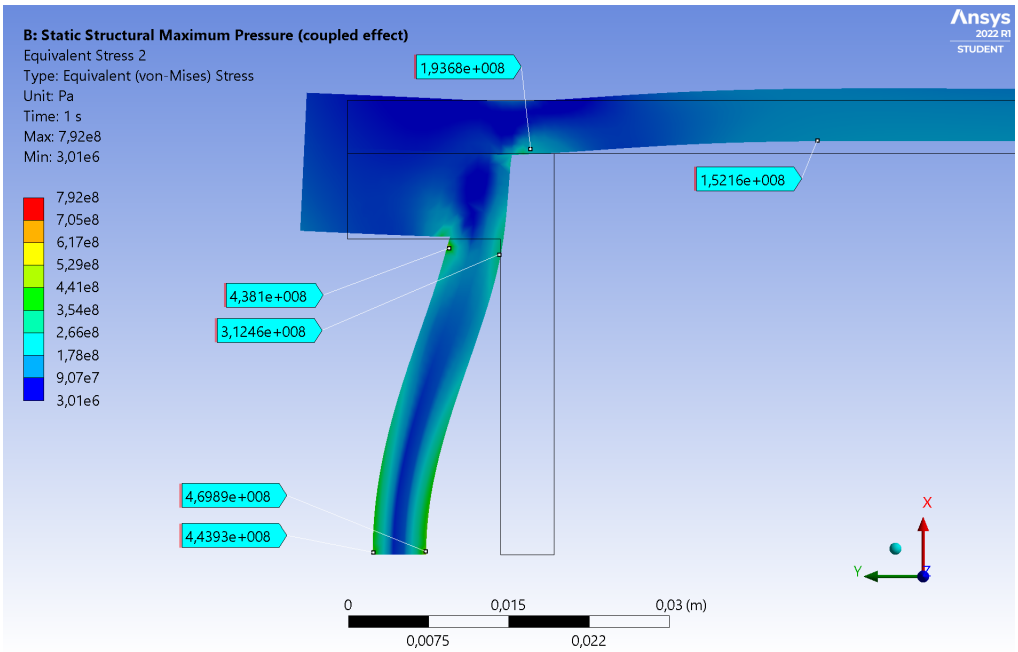

Figure 7.26: Zoom-in view of the top end's Von Mises stress distribution (Analysis 1). Scale factor: 15.

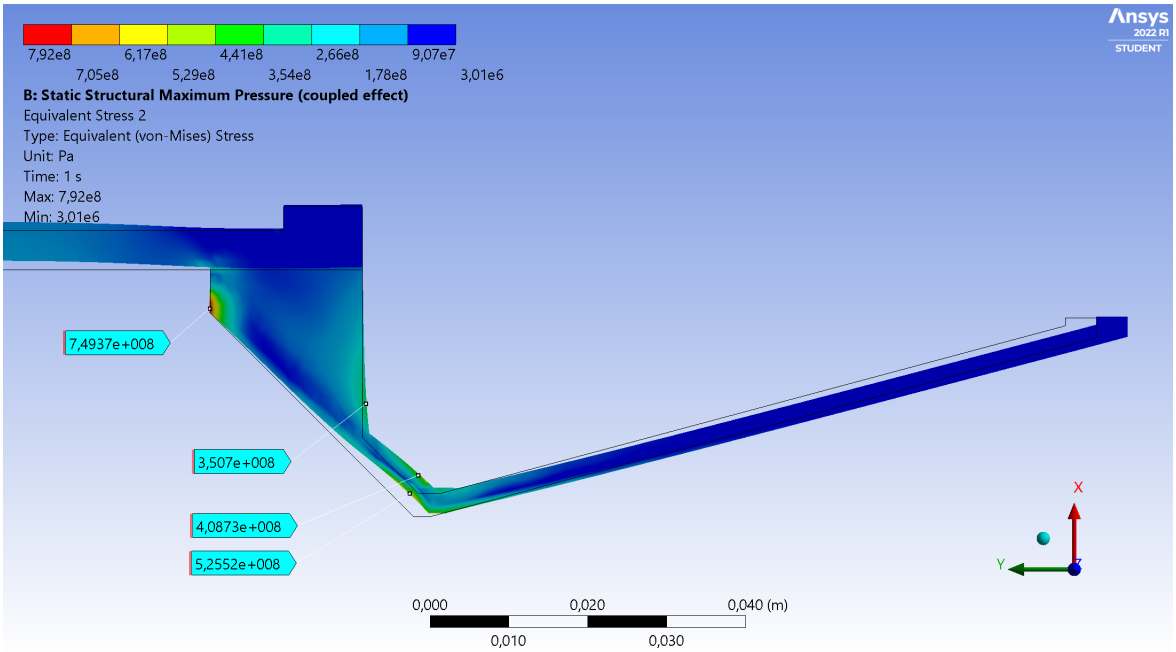

Figure 7.27: Zoom-in view of the bottom end's Von Mises stress distribution (Analysis 1). Scale factor: 15.

In this sense, a series of modifications have been developed so as to adjust the structure to the stresses seen in the analysis. Those modifications are:

1. A forward closure reinforcement in the central region. Since a stiffer material with a higher density would increase more the total mass than a simple reinforcement.

2. A nozzle reinforcement through several concentric rings in the thinner region of the converging section.

3. A change in the nozzle half converging angle from 45° to 47.1°, so as to reduce the thickness of the top surface.

This new geometry has been subjected to the same thermal and thermomechanical analysis than the previous geometry. Only the Von Mises stress distribution is presented (see figures 7.28 and 7.29), because the thermal results are practically identical to the previous.

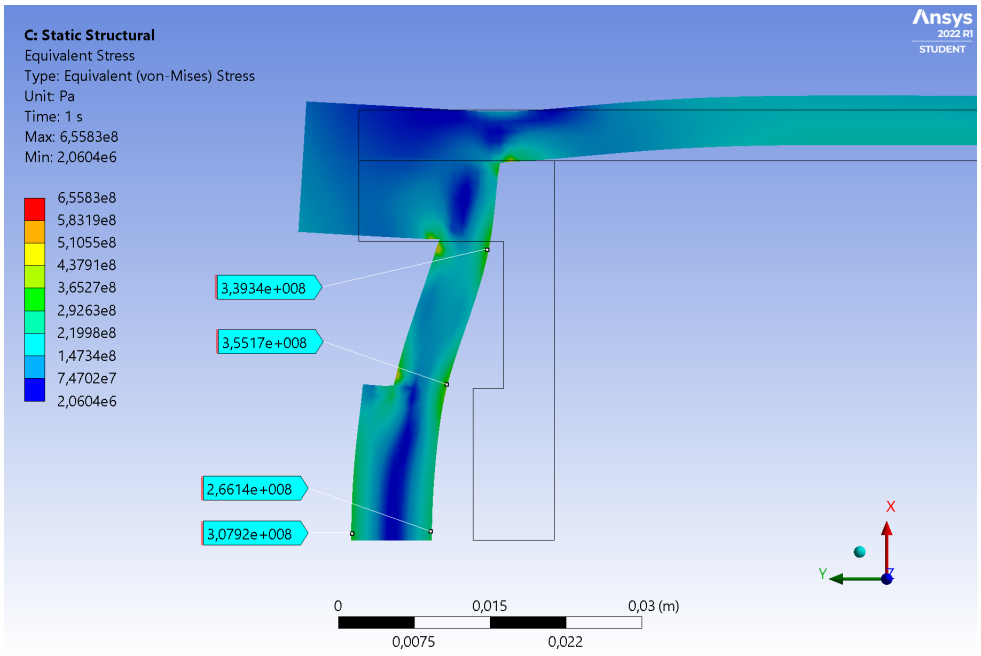

Figure 7.28: Zoom-in view of the top end's Von Mises stress distribution (Analysis 2). Scale factor: 15.

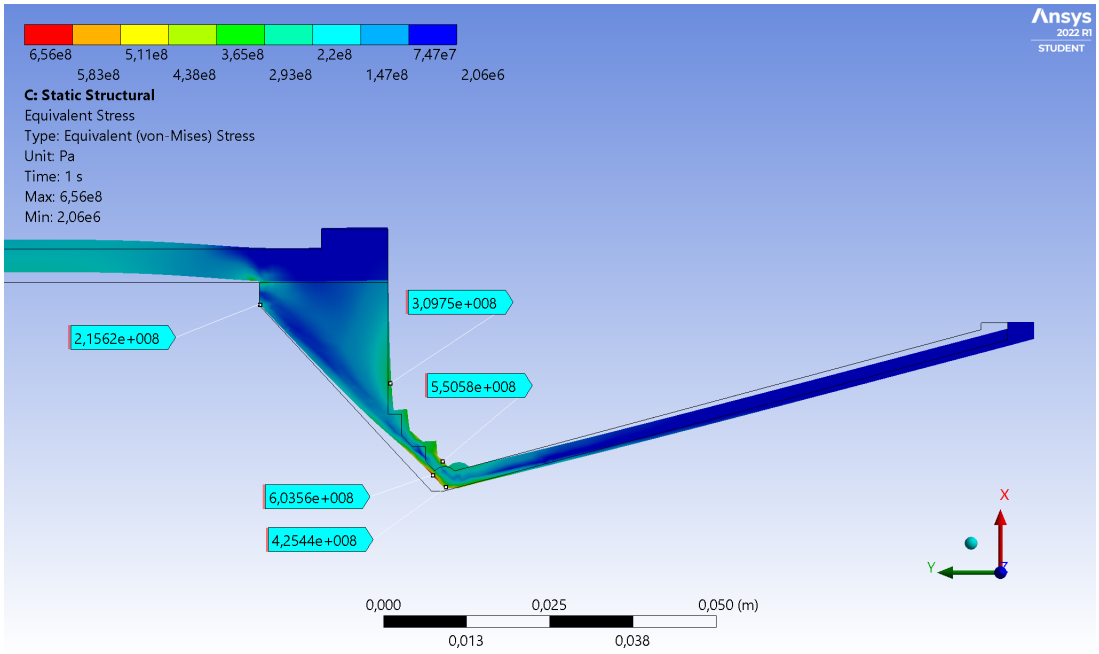

Figure 7.29: Zoom-in view of the bottom end's Von Mises stress distribution (Analysis 2). Scale factor: 15.

Again, figure 7.28 shows that the forward closure does not withstand the loads. Although

the central region does not burst thanks to the reinforcement, it exceeds the yielding strength. Also, regions of the thinner section of the forward closure surpass the ultimate strength.

In relation to the nozzle, the stress concentration that was seen in the top surface has been reduced with the increase of the angle. However, the reinforced region still exceeds the ultimate tensile strength at some points.

In order to resolve the issues mentioned, the following modifications will now be applied to the structure:

1. Removal of the forward closure reinforcement and change in the material to a 7075-T6 aluminium alloy. This alloy has a higher strength limits than the 6061-T6 (see table 5.2).

2. Removal of the ring reinforcements and increase of the nozzle thickness in the affected region.

A geometry with these adjustments has been analyzed again, and for the same reasons as in the previous analysis, only the Von Mises stress distribution is shown (see figures 7.30 and 7.31).

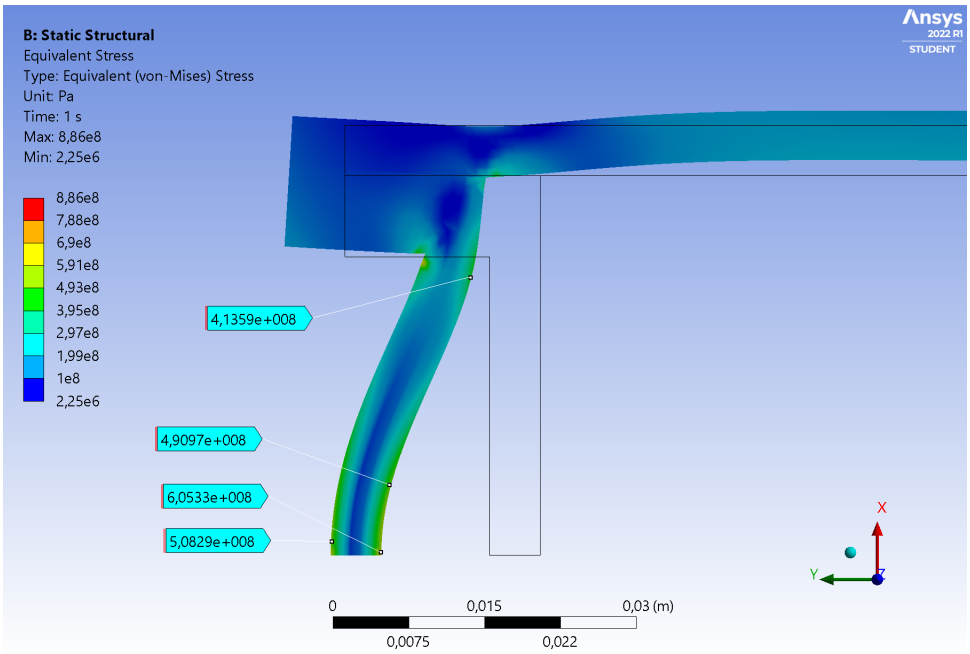

Figure 7.30: Zoom-in view of the top end's Von Mises stress distribution (Analysis 3). Scale factor: 15.

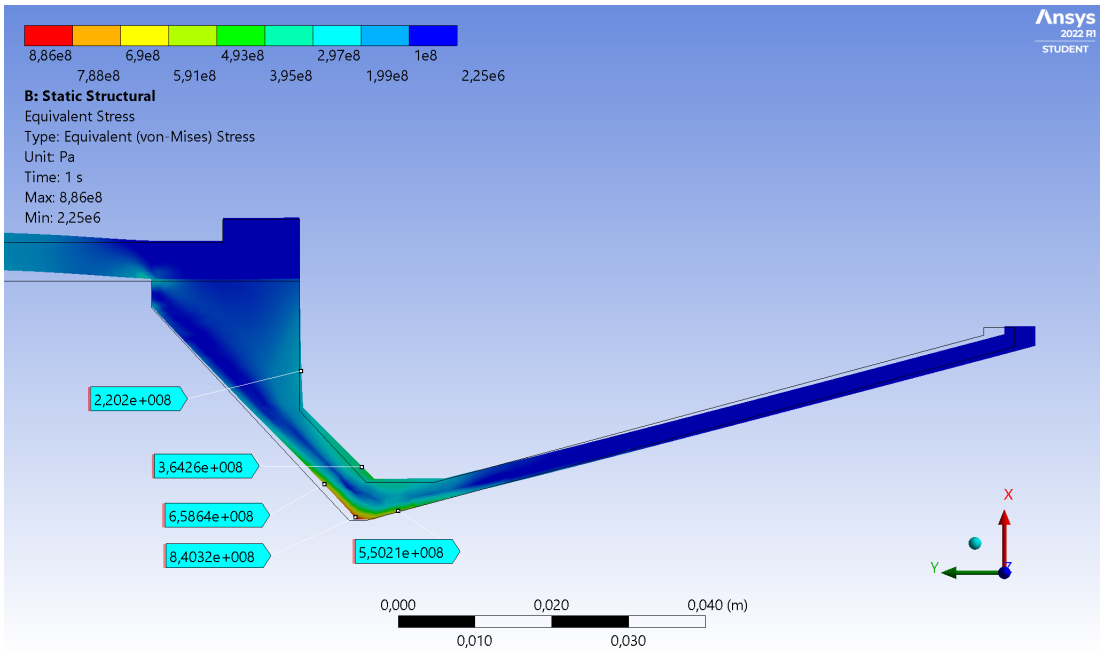

Figure 7.31: Zoom-in view of the bottom end's Von Mises stress distribution (Analysis 3). Scale factor: 15.

From the results of this last analysis, it can be seen that the forward closure still exceeds the yielding limit of the material in the central region, and the stresses in the critical region of the nozzle have increased with respect to the previous analysis. In this sense, new modifications will be performed in the affected components:

1. The same forward closure reinforcement seen in the second analysis will be added along with chamfers in the circular corners.
2. A different nozzle throat reinforcement will be added, inspired by the geometry employed in [9].

The results of this forth analysis are presented in figures 7.32 and 7.33.

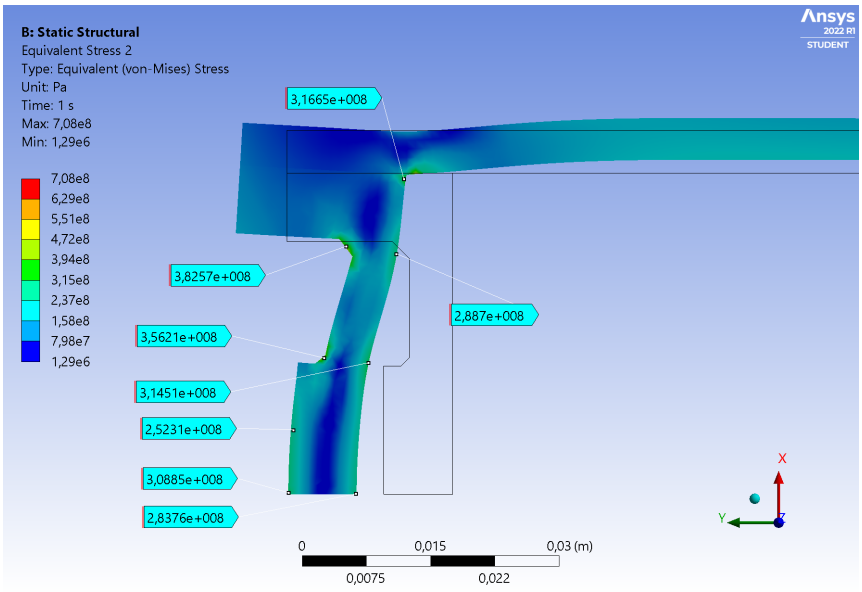

Figure 7.32: Zoom-in view of the top end's Von Mises stress distribution (Analysis 4). Scale factor: 15.

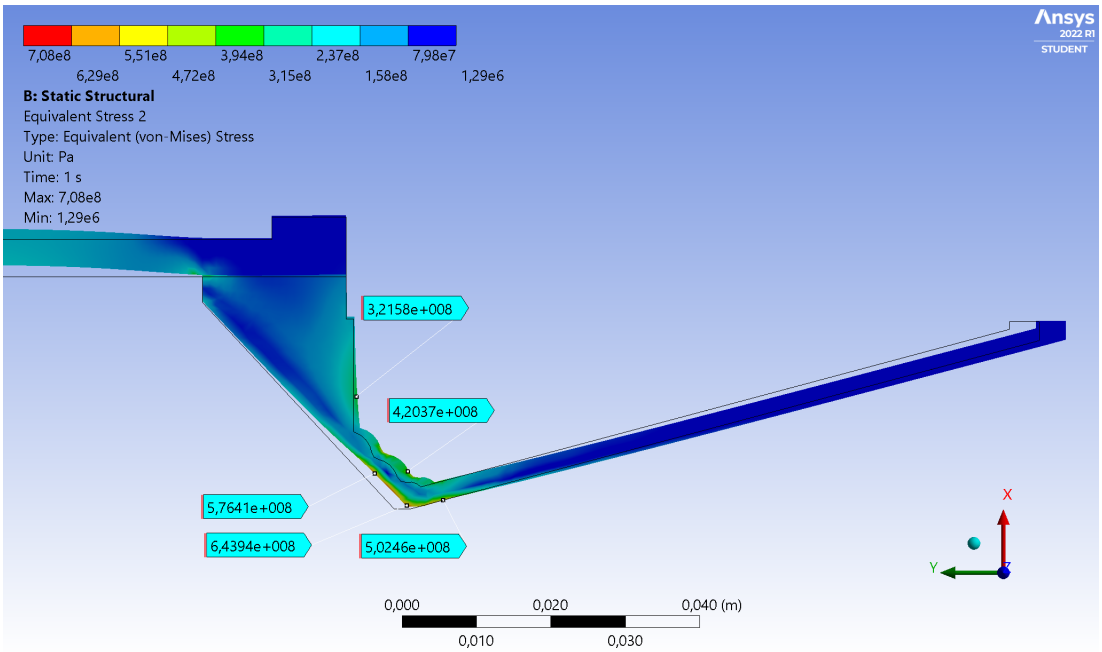

Figure 7.33: Zoom-in view of the bottom end's Von Mises stress distribution (Analysis 4). Scale factor: 15.

The combination of a strong aluminium alloy and the reinforcement proposed seem to withstand the loads applied at the forward closure, since the maximum stress in this component is $\sim 383\ MPa < \sigma_y(T_{amb}) = 480\ MPa$.

Nonetheless, the nozzle most critical region still exceeds the ultimate tensile strength of the steel employed, therefore, more resilient steels will be tested.

A summary of the geometry modifications performed in the structure throughout analysis 2, 3, and 4 is presented in figure 7.34 for clarification.

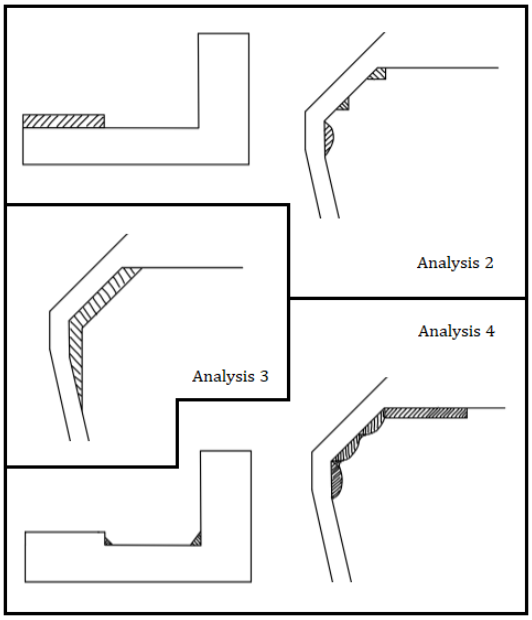

Figure 7.34: Summary of structure modifications employed in analysis 2, 3 and 4. Note that the striped regions are the ones that have been added at each analysis.

Some of the proposed materials to be tested are gathered and compared in table 7.5. Two steels with similar melting temperatures and higher strengths than the one used until now have been proposed (a high-carbon steel and a stainless steel).

Table 7.5: Comparison of structural properties from several steels for nozzle application. Source: <https://www.makeitfrom.com/>.

Material	Density ρ (g/cm^3)	Young's Modulus E (GPa)	Yield Strength σ_y (MPa)	Ultimate Strength σ_u (MPa)	Thermal Conductivity λ $(W/m \cdot K)$	Melting Temperature $(°C)$
Low-Carbon Steel SAE-AISI 1020	7.9	190	380	460	52	1420
Spheroidized and Cold Drawn High-Carbon Steel SAE-AISI 1090	7.8	190	610	790	50	1410
Half-Hard Stainless Steel AISI 301	7.8	200	860	1170	16	1400

The next analysis will be performed with the same forward closure geometry and material than the previous one, and with respect to the nozzle, the Spheroidized and Cold Drawn High-Carbon Steel SAE-AISI 1090 will be employed. Also, the reinforcement of the nozzle critical region will be eliminated, since the geometry with no reinforcements was the one with lower stress concentrations.

The results are presented in figure 7.35. Note that only the nozzle stress distribution is of interest now, because the forward closure does withstand the loads.

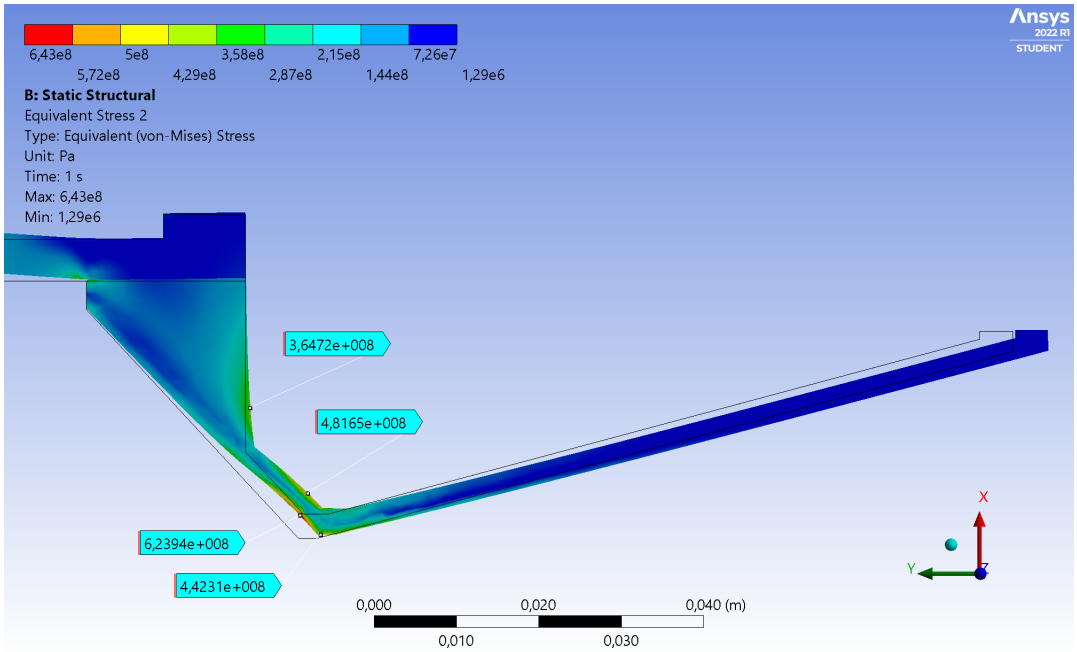

Figure 7.35: Zoom-in view of the bottom end's Von Mises stress distribution (Analysis 5). Scale factor: 15.

The results from this last analysis show that the yielding limit is again surpassed in the

most affected converging region.

Figure 7.36 presents the results obtained with a Half-Hard Stainless Steel AISI 301 in the nozzle.

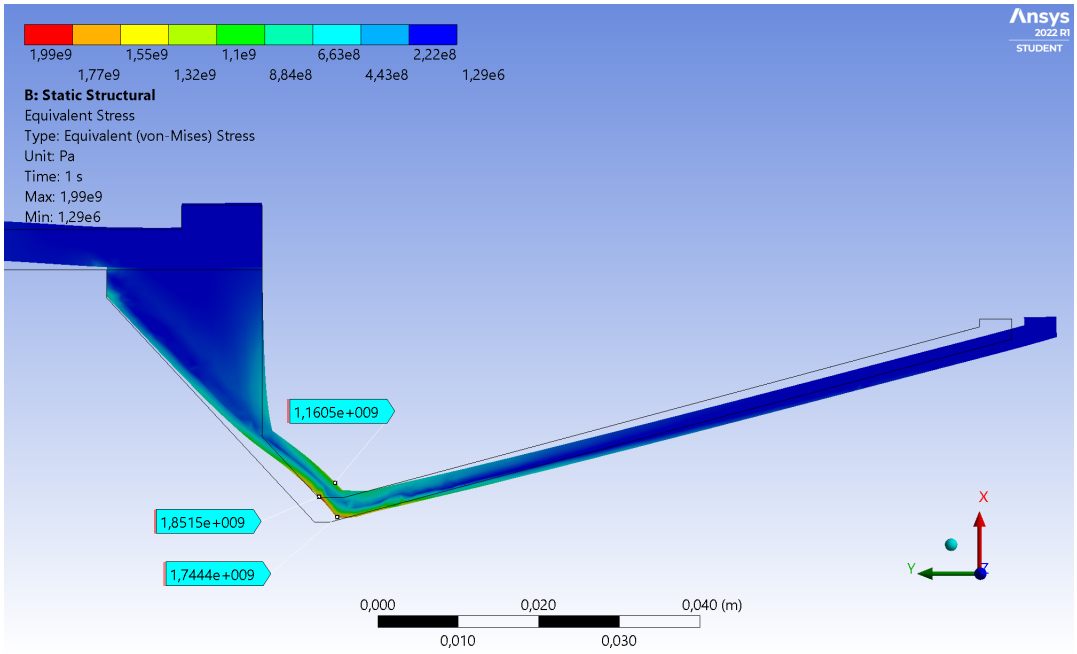

Figure 7.36: Zoom-in view of the bottom end's Von Mises stress distribution (Analysis 6). Scale factor: 15.

The results from this sixth analysis shows a tremendous increase in the stress concentrations at the union of the converging section with the throat. The yielding and ultimate limits of this stainless steel are once again exceeded.

In this situation, where no structural modification nor any other steel seems to withstand the nozzle stresses, some observations can be pointed out:

- The throat region and its surroundings seem to be the most critical region of the entire structure. This can be explained by the fact that the highest temperatures are achieved there. As previously mentioned, this causes an expansion of the material that, in turn, generates extra stresses. The conjunction of the stresses generated by the material expansion and the ones caused by the direct application of high pressures are so extreme, that can not be physically resisted by any of the steels employed (a temperature reduction would be needed).

- The stresses generated at the throat region of the nozzle are so high, that they exceed the yield and ultimate strengths of the materials at room temperature. It should be noted that in fact, the limits of the material at the throat are much lower than the ones mentioned, since the temperatures there, are extremely high (above 500 $°C$). The component failure has been evaluated in this sense.

- In analysis 1, 5 and 6, the same nozzle geometry was used (except for the converging angle of the first analysis), and three different steels were tested, each one with superior strength limits than the previous (see table 7.5). However, the more stiffer the steel used, the higher the stress concentrations that were produced near the throat region. This is explained because of the simultaneous decrease in the thermal conductivity of the

material. The lower the thermal conductivity, the higher the temperatures generated, and, therefore, the greater the stresses generated due to a material expansion.

In this scenario, two options are left for the continuity of the nozzle design: the use of ablative materials to avoid the extreme throat temperatures, or the use of a more expensive material with improved properties.

The first option has appeared numerous times across the thesis and the consequences are known: loss of performance throughout the motor operation due to the material erosion, non-reusable component.

The second option, requires the use of a high strength material, that while maintaining a similar melting temperature of that of steel, has a greater thermal conductivity. Although the use of this type of material could make the nozzle reusable, the drawback associated with it is the high cost of the material.

Finally, the option that has been selected is the second one. On the one hand, because of the lack of information regarding erosion rate of the ablative materials typically employed in this applications.

And on the other hand, the only supplier found, at the day of writing this thesis, that sells single-use nozzles for this kind of applications is *The RCS Store* in United States (<https://www.rocketmotorparts.com/>), where the cost of a nozzle for a 75 mm diameter motor ranges between $40 - 65$\$. However, shipment (around 20\$) and customs duty (15% of the cost of the products shipped) have to be included as well. Therefore, only the nozzle could cost around $66 - 94.75$\$ per flight if a single-use nozzle is employed. Then, if the motor is intended (as it is) to be used several times, a much expensive but reusable nozzle could be more worthwhile than a single-use (depending on the total cost of the reusable nozzle).

The material to be employed that fulfills the requirements just mentioned is the Molybdenum. It is one of the lightest refractory metals, although it is heavier than steel, has a melting temperature of 2620 $°C$ and a very low coefficient of thermal expansion (5.2×10^{-6} K^{-1}). Other properties of this material such as modulus of elasticity, yield strength, and ultimate tensile strength at room temperature are presented in table 7.6.

Table 7.6: Structural properties of molybdenum.
Source: <https://matmatch.com/>.

Material	**Density** ρ (g/cm^3)	**Young's Modulus** E **(GPa)**	**Yield Strength** σ_y **(MPa)**	**Ultimate Strength** σ_u **(MPa)**	**Thermal Conductivity** λ $(W/m \cdot K)$	**Melting Temperature** $(°C)$
Molybdenum	10.28	330	550	700	142	2620

Figures 7.37 and 7.38, show the temperature dependence of the yield and tensile strength of Molybdenum for very high temperatures.

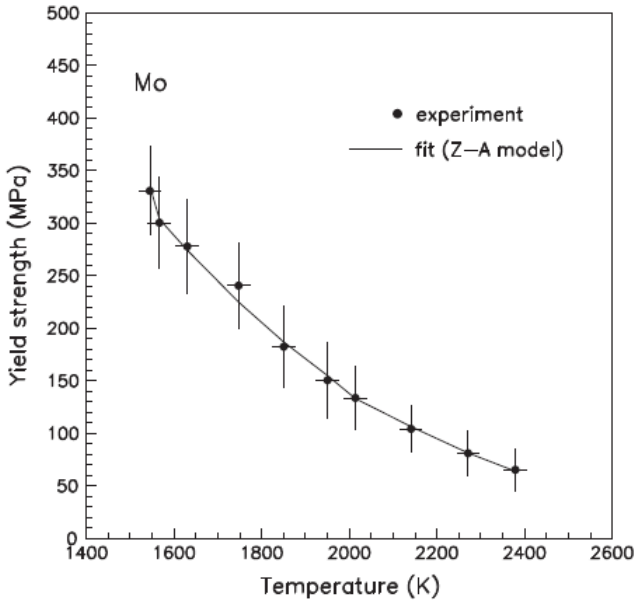

Figure 7.37: Molybdenum yield strength for very high temperatures. Source: [19].

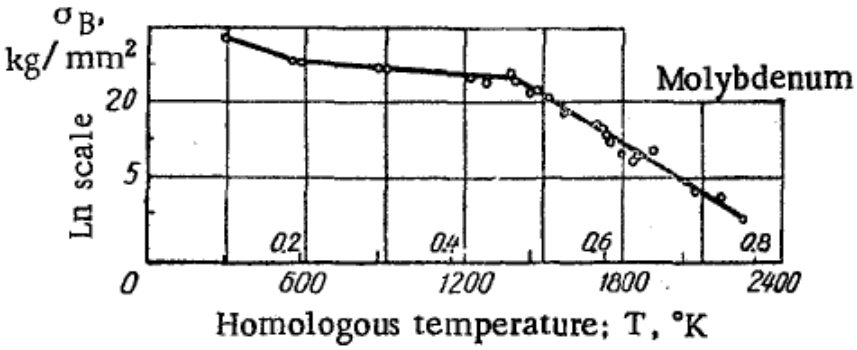

Figure 7.38: Molybdenum tensile strength for very high temperatures. Note that the vertical axis is in logarithmic scale. Source: [20].

A new analysis with the same geometry as the previous has been developed using Molybdenum as the nozzle material. Results of the Von Mises stress distribution at the nozzle are presented in figure 7.39.

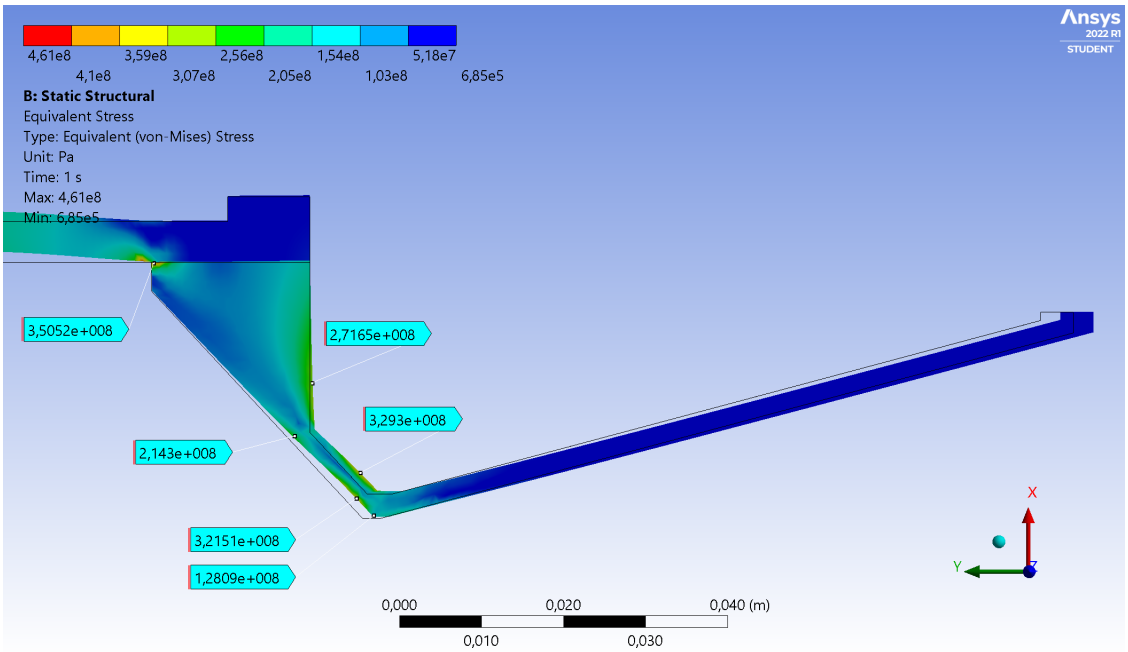

Figure 7.39: Zoom-in view of the bottom end's Von Mises stress distribution (Analysis 7). Scale factor: 15.

In the last result presented it can be seen that a stress concentration with a maximum value of $\sim 350\ MPa$ is reached at the union of the case with the nozzle, while the rest of the nozzle presents lower stresses. This concentration though, is generated by the program from the bonded condition of both components. In reality, this concentration would not produce, since the two components are bonded only at the bolt union, therefore, this value won't be taken into account.

In order to validate the integrity of the molybdenum nozzle, the temperature distribution of the component (which has been determined prior to the thermomechanical analysis) must be known. In this sense, figure 7.40 presents the nozzle temperature distribution at the maximum pressure instant.

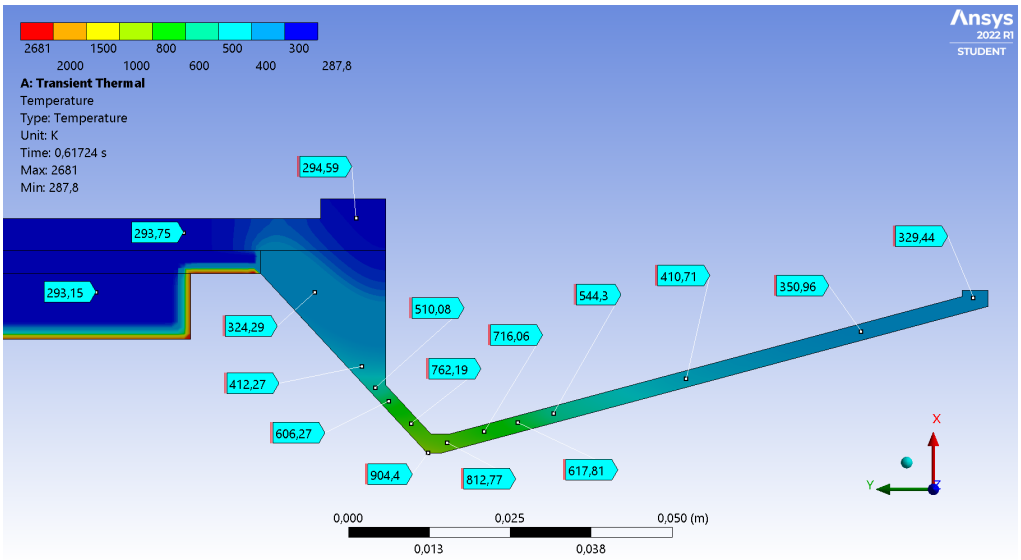

Figure 7.40: Zoom-in view of the bottom end's temperature distribution for the maximum pressure instant.

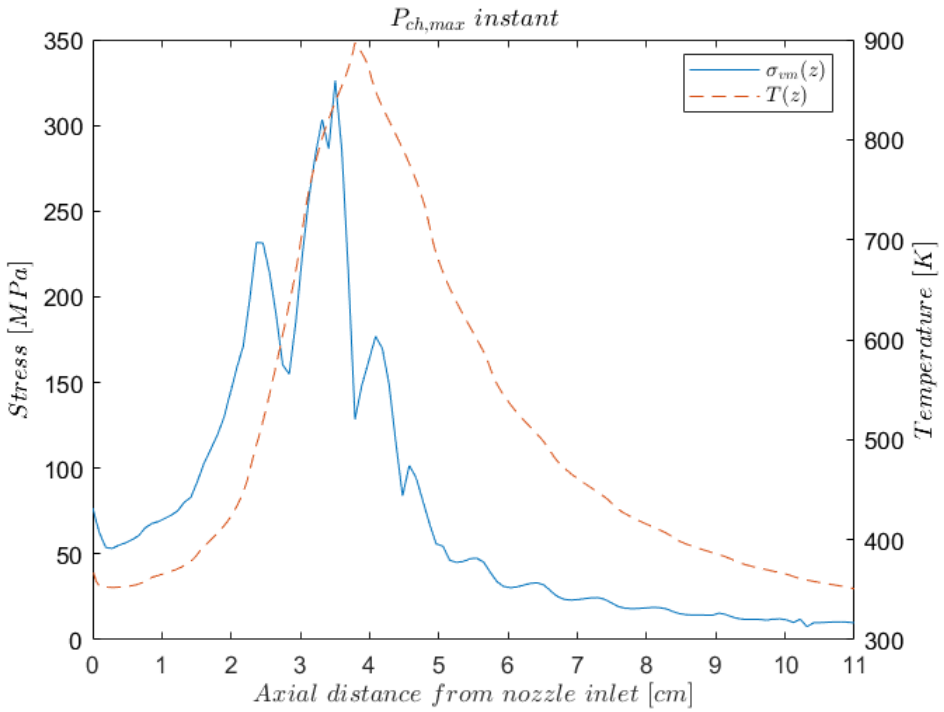

Figure 7.41: Von Mises stresses and temperature distribution at the nozzle inner surface for the maximum chamber pressure instant.

From figures 7.40 and 7.41, the maximum temperature is 904.4 K and is reached at the nozzle throat. Then, by assuming that the yield strength of molybdenum follows a similar trend to that of the tensile strength, it can be considered that

$$for\ T < 900\ K \longrightarrow \sigma_y > 350\ MPa$$

Since the rest of the nozzle is at temperatures under 900 K, and the stresses are also under 350 MPa, the structural integrity of the nozzle is achieved for this instant.

The mechanical and thermal load contributions have been analyzed separately in order to appreciate the effects of each one. The results are presented in appendix G.

7.2.5 Results (maximum nozzle temperature)

The maximum nozzle temperature (1206 K = 933 $°C$) is reached at burnout, that is at $t = 1.453\ s$. It is a critical instant to evaluate, since the stresses produced by the thermal loads are maximum. The temperature distribution at this instant is presented in figure 7.42.

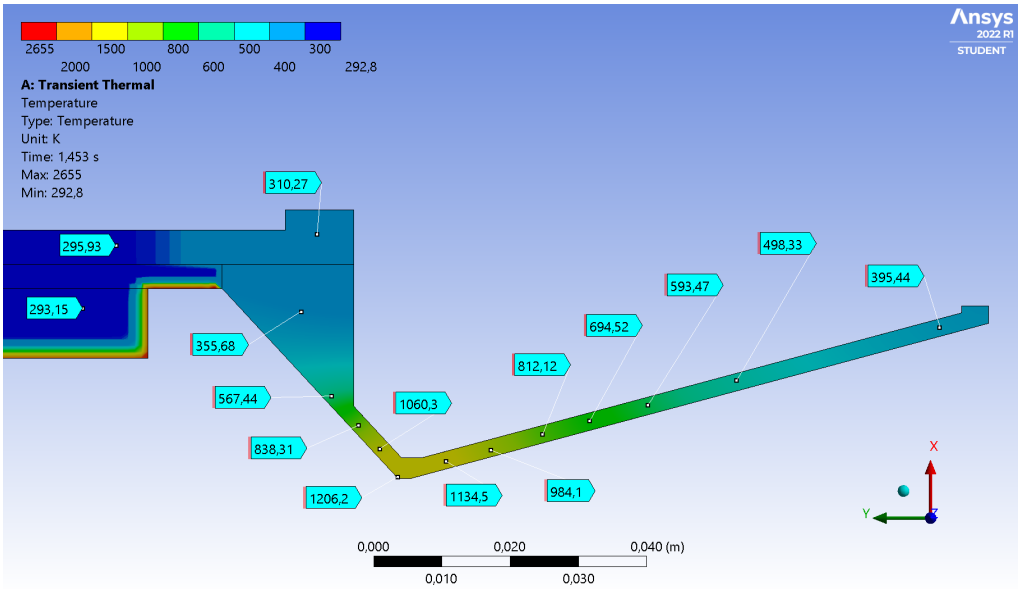

Figure 7.42: Zoom-in view of the bottom end's temperature distribution for the maximum temperature instant.

In this subsection, only the nozzle will be analyzed, since the forward closure remains at room temperature. Therefore, if as seen earlier, it withstands the loads derived from the maximum chamber pressure instant, it shall withstand the loads from the entire motor operation time.

The Von Mises stress distribution of the whole nozzle at burnout is presented in figure 7.43, however, for more clarification, figure 7.44 is also added. This last graph, presents the Von Mises stress and the temperature distribution of the nozzle inner surface.

From these results, in the first place, it is clear that the stresses generated at the nozzle are greater at burnout than at the maximum chamber pressure instant (over $\sim$ 100 MPa greater considering the maximum values).

In the second place, it is not clear if the regions with higher stresses exceed the yielding temperature of molybdenum, since the data obtained from [19] only covers the range between $1400 - 2400\ K$, and no other data was found.

In the third place, the maximum stress location (a point in the converging section near the throat) do not coincide with the maximum temperature location (the throat).

$$\sigma_{vm,max} = 486\ MPa \longrightarrow T \sim 700\ K$$

$$T_{max} = 1206\ K \longrightarrow \sigma_{vm} \sim 160\ MPa$$

The most critical point would be located at the converging section next to the throat, with an equivalent stress of $\sigma_{vm} \sim 450\ MPa$ and a temperature of $T \sim 1150\ K$.

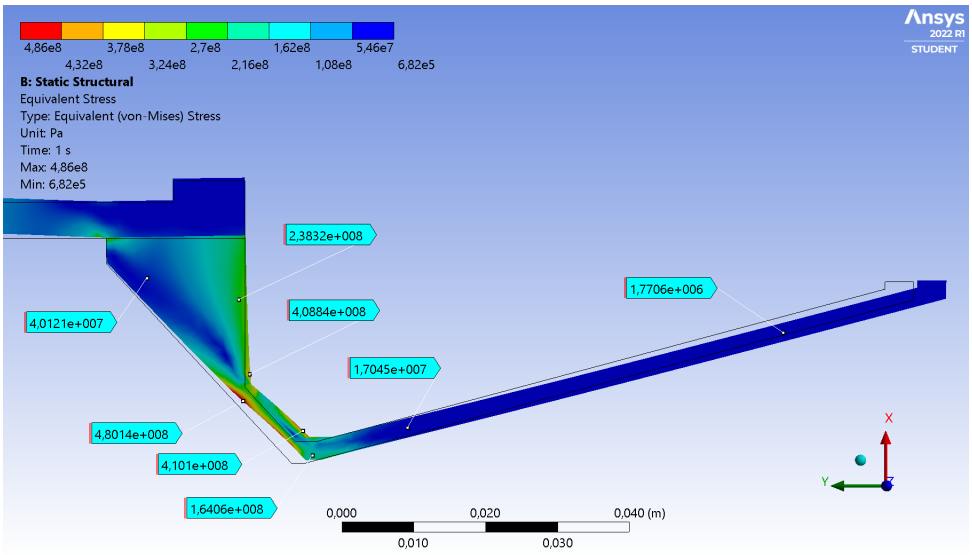

Figure 7.43: Zoom-in view of the bottom end's Von Mises stress distribution (Analysis 8). Scale factor: 15.

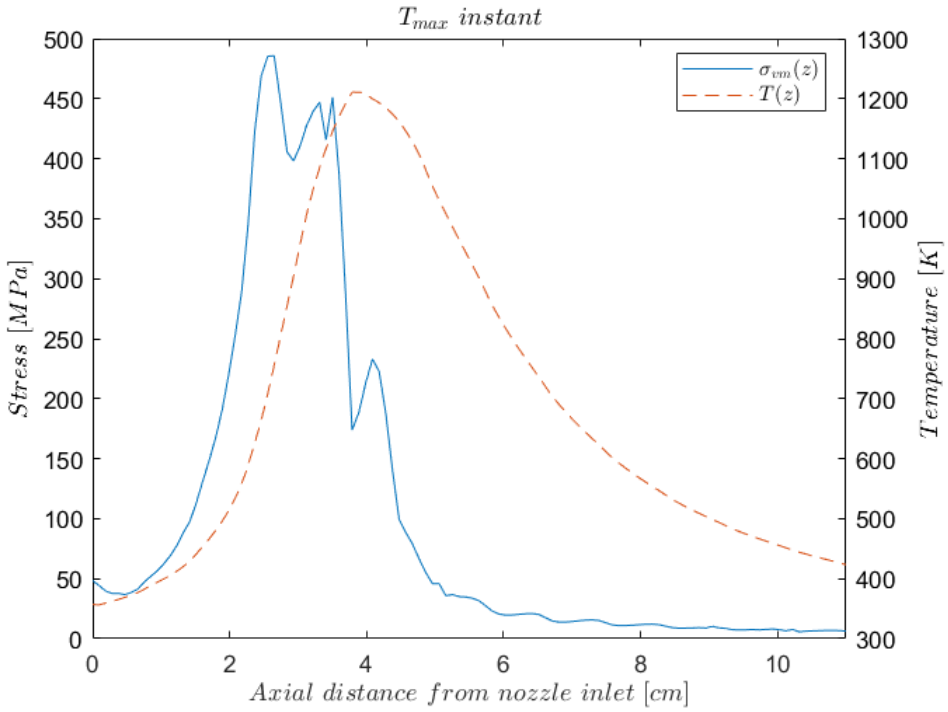

Figure 7.44: Von Mises stresses and temperature distribution at the nozzle inner surface for the maximum nozzle temperature instant.

The mechanical and thermal load contributions for this instant have also been analyzed separately, as in the previous case, and the results are presented in appendix H.

Chapter 8

Budget summary

The budget of the thesis has been developed in a separate document from the report, however, the results are summarized and presented in this chapter.

The break down cost of the design process itself is showed in table 8.1, whereas table 8.2 presents the break down cost of the motor manufacture.

Table 8.1: Budget of the design process of the thesis.

Expenses	Cost [€]
Professional fee	2268
Software lincenses	1600
Electric power consumption	25.74
TOTAL	**3893.74**

Table 8.2: Budget of the manufacturing process of the motor.

Expenses	Cost [€]
Propellant	129.32
Single-use components	15.52
Reusable components	1958.78 (1837.78)[1]
TOTAL	**2103.62 (1982.62)[1]**

[1] Cost without the anodized and painted finish.

From the *EuroSpaceTechnology* website, the prices of the most expensive, the cheapest, and an equivalent COTS motors can be obtained for a cost comparison: 1542.95 €, 678 €, and 1170 €, respectively [2].

Although the requirement GR-02 (which states that the total cost of the designed motor shall be less than the average cost of an equivalent COTS motor) is not met for a single flight, it is met for a minimum of 4 flights. This can be seen in figure 8.1, where the accumulated cost vs the number of flights for several motors has been plotted.

It is also worth noting that the designed motor becomes worthwhile for a minimum of 2 flights with respect to the most expensive 75 mm COTS motor, and for a minimum of 17 flights with respect to the cheapest 75 mm COTS motor.

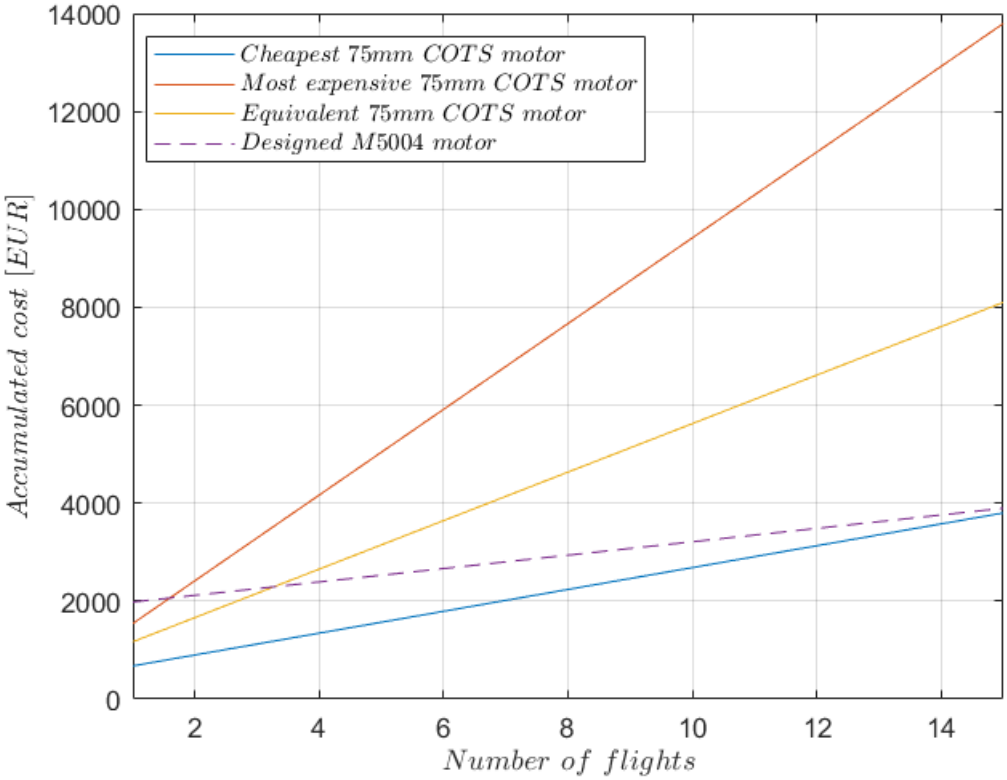

Figure 8.1: Comparison of the accumulated cost vs number of flights, for several COTS motors with respect to the designed motor.

Chapter 9

Analysis and assessment of environmental implications

The impact that the designed motor would have in the environment can not be considered to be positive, since at least five polluting agents are present in the combustion products expelled through the nozzle. Those are: carbon monoxide, hydrogen chloride, carbon dioxide, methane, and nitric oxide. The total mass of each product that is expected to be ejected per flight, can be computed from the molecular weight of the compounds, the number of moles per 100 g of propellant of each compound, and the total propellant mass.

Total mass of carbon monoxide

$$M_{\mathrm{CO}} = \mathrm{MW}_{\mathrm{CO}} \cdot \frac{n_{\mathrm{CO}}}{100\ g\ propellant} \cdot M_{propellant} = \\ = 28.0104 \frac{g\ \mathrm{CO}}{mol\ \mathrm{CO}} \cdot \frac{1.338\ mol\ \mathrm{CO}}{100\ g\ propellant} \cdot 3143.5\ g\ propellant = 1178.1\ g\ \mathrm{CO}$$

Total mass of hydrogen chloride

$$M_{\mathrm{HCl}} = \mathrm{MW}_{\mathrm{HCl}} \cdot \frac{n_{\mathrm{HCl}}}{100\ g\ propellant} \cdot M_{propellant} = \\ = 36.46064 \frac{g\ \mathrm{HCl}}{mol\ \mathrm{HCl}} \cdot \frac{0.644\ mol\ \mathrm{HCl}}{100\ g\ propellant} \cdot 3143.5\ g\ propellant = 738.1\ g\ \mathrm{HCl}$$

Total mass of carbon carbon dioxide

$$M_{\mathrm{CO_2}} = \mathrm{MW}_{\mathrm{CO_2}} \cdot \frac{n_{\mathrm{CO_2}}}{100\ g\ propellant} \cdot M_{propellant} = \\ = 44.0098 \frac{g\ \mathrm{CO_2}}{mol\ \mathrm{CO_2}} \cdot \frac{0.158\ mol\ \mathrm{CO_2}}{100\ g\ propellant} \cdot 3143.5\ g\ propellant = 218.6\ g\ \mathrm{CO_2}$$

Total mass of methane

$$M_{\mathrm{CH_4}} = \mathrm{MW}_{\mathrm{CH_4}} \cdot \frac{n_{\mathrm{CH_4}}}{100\ g\ propellant} \cdot M_{propellant} = \\ = 16.043 \frac{g\ \mathrm{CH_4}}{mol\ \mathrm{CH_4}} \cdot \frac{1.003 \times 10^{-4}\ mol\ \mathrm{CH_4}}{100\ g\ propellant} \cdot 3143.5\ g\ propellant = 0.051\ g\ \mathrm{CH_4}$$

Total mass of nitric oxide

$$M_{\mathrm{NO}} = \mathrm{MW}_{\mathrm{NO}} \cdot \frac{n_{\mathrm{NO}}}{100\ g\ propellant} \cdot M_{propellant} = \\ = 30.006 \frac{g\ \mathrm{NO}}{mol\ \mathrm{NO}} \cdot \frac{3.054 \times 10^{-6}\ mol\ \mathrm{NO}}{100\ g\ propellant} \cdot 3143.5\ g\ propellant = 0.003\ g\ \mathrm{NO}$$

Although this is just a prediction of the environmental impact of the motor, the design itself also has a direct impact associated. It can be computed from the power consumption of the tools used, and the emission factor of the power sources.

Only a laptop has been used, with an average consumption of $\sim 200\ W$. The total hours employed in the thesis have been around $12\ ECTS \cdot 25\ h/ECTS = 300\ h$. By considering that the CO_2 emission factor of electricity in 2022 in Catalonia is $0.259\ kg\ CO_2/kWh$ [21], the total CO_2 emissions from the design of the motor are

$$0.2\ kW \cdot 300\ h \cdot 0.259\ kg\ CO_2/kWh = 15.54\ kg\ CO_2$$

Chapter 10

Conclusions

Throughout the course of this thesis, a first motor design has been developed so as to fulfill all the objectives outlined in the introduction. Those include the propulsion of the Phobos rocket to a 3 km threshold while complying with the EuRoC requirements, the reduction in cost and the increase in availability for the motors in UPCSP, and the design and analysis of a solid rocket motor.

The requirements compliance will be now assessed in order to review how the motor design proposal deals with the restrictions imposed initially (see table 10.1).

Table 10.1: Requirement compliance matrix.

Code	Compliance	Justification
GR-01	Intend to Comply	The lack of molybdenum information regarding yield and ultimate tensile strength dependency on temperature and heating rate makes it unfeasible to determine whether the nozzle will withstand the stresses generated at burnout.
GR-02	Partial Compliant	The cost of the designed motor is less than that of an equivalent COTS motor, if used for more than 4 flights.
PR-01	Compliant	The total motor impulse has been computed in the performance evaluation chapter and is 7271 $N \cdot s$.
PR-02	Compliant	Assessed during rocket performance evaluation. The predicted altitude of the Phobos rocket with the designed motor loaded is 3113 m.
MR-01	Compliant	All the structural materials employed in the motor design are metalic.
MR-02	Compliant	The bolts selected for the motor assembly are made of a grade 10.9 steel alloy.
MR-03	Compliant	Only flexible materials have been used throughout the design process. Although some steels were used in earlier design phases, they are only considered to be brittle at very low temperatures, which is not the case.
GCR-01	Compliant	The constraint has been taken into account during the preliminary design phase.
GCR-02	Compliant	The total length of the motor case is exactly 893 mm.
PRR-01	Compliant	APCP is considered to be non-toxic in the EuRoC Rules & Requirements.
SR-01	Intend to Comply	A preliminary design has been developed with this restriction, however, during the detailed design phase, it could not be determined from the finite element analysis due to the lack of material information.

From the results obtained throughout the thesis, some conclusions can be drawn:

Although mid-performance propellants such as the PN/Epoxy/Fe are very suitable because of its low combustion temperature, it has been seen that they do not have enough energy to propel the Phobos rocket to the desired altitude, given the geometrical constraints imposed. Therefore, high-performance propellants were chosen for this application, more specifically, the AP/HTPB/Al.

Chemically powered rocket engines (solid, liquid, and hybrid) do not perform as perfect propulsion systems, in fact, they have many types of losses associated. In this thesis, the more severe effects of loss of performance have been taken into account in order to design the motor. In this sense, the effect that has been found to affect more directly to the total performance is the nozzle divergence angle, with a loss of exhaust velocity associated of 1.7%. Next are the boundary layer effects, with a loss factor of 1.0%, and, finally, the heat losses through the nozzle wall, with a loss factor associated to the exhaust velocity of 0.51%. Nonetheless, the reader should be aware that more types of losses are present in real nozzles (two phase flow, combustion efficiency, shock waves or flow discontinuities...), however, only the mentioned effects have been considered.

An internal ballistic software has been developed in order to predict the solid rocket motor performance, and has been compared to the current software in use in the sector, with maximum relative errors of 4.6% and 5.2% in the chamber pressure computation. It must be pointed out, though, that the program, as well as the other two similar programs used (BurnSim and OpenMotor), do not contemplate the effects of ambient temperature dependency of the grain, erosive burning, longitudinal and lateral rocket acceleration effects, nor rocket spin enhancements.

In a 1.453 s burning duration, the nozzle throat reaches a maximum temperature of 933 $°C$. This is caused by the tremendous chamber temperatures and the convection heat transfer that produces at the nozzle. During the thermal analysis of the rocket, it has been seen that for this short burning times, a simple cardboard or even a phenolic resin impregnated tube isolates perfectly the casing structure. Moreover, the problematic of dealing with high nozzle temperatures and the difficulty of controlling them has also been seen, being unfeasible to use the most common cooling methods in the professional sector: film cooling, regenerative cooling, radiation cooling and ablative cooling. Since the first two are employed in liquid propellant rocket engines, the third is used in space applications, and the latter conflicts with the reusability requirement. Another important aspect seen in the analyses, makes reference to the conduction heat transfer at the nozzle, where it has been observed that for a higher thermal conductivity, the nozzle temperature was significantly decreased. It is because of this reason, that the different steel alloys tested weren't suitable for the nozzle, since their thermal conductivity is relatively low.

Several nozzle geometries, reinforcements and steel alloys have been tested in the thermomechanical analysis phase, nevertheless, none of them has proofed to withstand the stresses generated at the nozzle. Although those design proposals could withstand the pressures to which they are exposed to, it is the combined thermal effect of yield and ultimate strength reduction, and the generation of extra stresses due to a material expansion, what causes the structural failure. Therefore, if a drastic temperature reduction was achieved in the critical nozzle region, a steel alloy would be suitable for this application. In this sense, a rare material has been chosen to make up the nozzle, that is molybdenum. As stated in the detailed design chapter, it has been chosen because of its high melting point, the increase in thermal

conductivity with respect to steel, and its strength limits. Although it might seem an odd material, it is relatively common in the professional sector, where along with other refractory metals, such as tungsten, niobium, tantalum or rhenium, are used in propulsive applications for their extreme properties. As mentioned earlier, the integrity of the molybdenum nozzle could not be determined for the maximum nozzle temperature instant, since the yield and ultimate tensile strength, not only depend on temperature but also on heating rate, and this data could not be found by any means. However, from the strength trends and the rapid heating of the nozzle, one could expect the component to remain without deforming, but this is just an assumption and not based in scientific data.

It is worth noting that the structural analysis has been developed using a linear constitutive model. Thus, it has been used to predict if the structure would fail or not (in other words, if the structure response remained in the elastic regime or not). In order to determine the permanent deformations of the structure once the yield strength is exceeded, a plastic (non-linear) model such as the Johnson-Cook would then be required. Although a complete thermomechanical study has not been done due to its complexity and the time it takes, the bases, the characteristics, and the consequences of a problem of this type have been understood and developed.

In terms of cost, although the total cost for manufacturing a single motor is significantly higher than that of an equivalent COTS motor, the cost of the reloads (that is the propellant, casting tube, thermal insulators, and o-rings) is very small in comparison with the mentioned commercial motors. Therefore, is has been seen that for a minimum of 4 operations, the designed M5004 motor would be worthwhile. Also related to the budget is the cost of the metal pieces, which even though the change in the nozzle material from steel to molybdenum has an impact on the cost, the major part of it comes from the fabrication process.

Further work

The following improvements could be tackled in future work in order to continue with the research of this thesis:

- A 2 phase flow study of the combustion products.
- The analysis of the grain structural integrity for propellant cracking avoidance.
- The characterization and test of less polluting propellants such as AN-based.
- The development of a refined Computational Fluid Dynamics (CFD) analysis of the nozzle flow, so as to determine the pressure change with more detail than with the isentropic relations.
- The development of a more refined thermomechanical analysis through a non-linear Johnson-Cook model.
- The manufacture and the subsequent static fire test of the designed motor for comparison of the actual and predicted performance.

Bibliography

[1] Á. Lopes, I. Ávila, M. Wihelm, and P. Quental, *European Rocketry Challenge Rules & Requirements*. Feb. 2021, Last accessed 14 March 2022. [Online]. Available: https://euroc.pt/wp-content/uploads/2022/02/EuRoC2022_RR_V03-.pdf.

[2] *PRO 75 RELOADS*. Euro Space Technology - Rocketworld, 2022, Last accessed 14 March 2022. [Online]. Available: https://eurospacetechnology.eu/index.php?id_category=58&controller=category.

[3] G. P. Sutton and O. Biblarz, *Rocket propulsion elements*, 9th ed. John Wiley & Sons, 2017.

[4] T. McCreary, "Experimental composite propellant," *Murray, Kentucky*, 2000.

[5] R. Nakka, *Richard Nakka's Experimental Rocketry Site*. 1997, Last accessed 20 June 2022. [Online]. Available: http://www.nakka-rocketry.net/.

[6] S. Chaturvedi and P. N. Dave, "Solid propellants: Ap/htpb composite propellants," *Arabian Journal of Chemistry*, vol. 12, no. 8, pp. 2061–2068, 2019.

[7] A. Coma Busquets, "Specification, design and development of a solid rocket engine for suborbital sounding missions," Universitat Politècnica de Catalunya, Dec. 2020.

[8] P. G. Hill and C. R. Peterson, *Mechanics and thermodynamics of propulsion*, 2nd ed. Pearson, 1992.

[9] C. M. Suryavanshi, "Thermo-structural analysis of a rocket engine thrust chamber," Universitat Politècnica de Catalunya & University of Pisa, Dec. 2018.

[10] D. Bartz, "Turbulent boundary-layer heat transfer from rapidly accelerating flow of rocket combustion gases and of heated air," Jet Propulsion Laboratory, California Institute of Technology, Tech. Rep., Dec. 1963.

[11] S.-G. Wu and C. Tao, "Application of the finite element method to the nozzle-wall temperature prediction," *American Institute of Aeronautics and Astronautics*, Jun. 1979.

[12] E. Hearn, *Mechanics of Materials, Volume 1-An Introduction to the Mechanics of Elastic and Plastic Deformation of Solids and Structural Materials*, 3rd ed. Butterworth-Heinemann, 1997.

[13] R. Huston and H. Josephs, *Practical stress analysis in engineering design*, 3rd ed. CRC Press, 2009.

[14] J. A. Chambers, "Preloaded joint analysis methodology for space flight systems," National Aeronautics and Space Administration, Technical Memorandum NASA-TM-106943, Dec. 1995, Last accessed 20 June 2022. [Online]. Available: https://ntrs.nasa.gov/citations/19960012183.

[15] J. C. Thomas, G. R. Morrow, C. A. Dillier, and E. L. Petersen, "Comprehensive study of ap particle size and loading effects on the burning rates of composite ap/htpb propellants," in *2018 Joint Propulsion Conference*, 2018, p. 4874.

[16] W. H. Miller, "Solid rocket motor performance analysis and prediction," National Aeronautics and Space Administration, Special Publication NASA-SP-8039, May 1971, Last accessed 20 June 2022. [Online]. Available: https://ntrs.nasa.gov/citations/19720011135.

[17] W. Miller and D. Barrington, "A review of contemporary solid rocket motor performance prediction techniques," *Journal of Spacecraft and Rockets*, vol. 7, no. 3, pp. 225–237, 1970.

[18] M. A. Willcox, M. Q. Brewster, K.-C. Tang, D. S. Stewart, and I. Kuznetsov, "Solid rocket motor internal ballistics simulation using three-dimensional grain burnback," *Journal of Propulsion and Power*, vol. 23, no. 3, pp. 575–584, 2007.

[19] G. Škoro, J. Bennett, T. Edgecock, and C. Booth, "Yield strength of molybdenum, tantalum and tungsten at high strain rates and very high temperatures," *Journal of nuclear materials*, vol. 426, no. 1-3, pp. 45–51, 2012.

[20] V. Borisenko, "Investigation of the temperature dependence of the hardness of molybdenum in the range of 20-2500° c," *Soviet Powder Met. Metal Ceram.(English Transl.)*, 1962.

[21] Generalitat de Catalunya. Departament d'Acció Climàtica, Alimentació i Agenda Rural, *Guia de càlcul d'emissions de gasos amb efecte d'hivernacle (GEH)*. Apr. 2022, Last accessed 14 June 2022. [Online]. Available: https://canviclimatic.gencat.cat/web/.content/04_ACTUA/Com_calcular_emissions_GEH/guia_de_calcul_demissions_de_co2/220427_GUIA-CALCUL-EMISSIONS-GEH_v_2022.pdf.

[22] C. D. P. Segarra, *Transferència de calor per conducció, Heat transfer lecture notes*. Universitat Politècnica de Catalunya, 2021.

[23] ——, *Convection mathematical formulation, Heat transfer lecture notes*. Universitat Politècnica de Catalunya, 2021.

[24] S. Gordon and B. J. McBride, "Computer program for calculation of complex chemical equilibrium compositions and applications. part 1: Analysis," National Aeronautics and Space Administration, Office of Management, Tech. Rep., 1994.

[25] B. J. McBride, S. Gordon, and M. A. Reno, "Coefficients for calculating thermodynamic and transport properties of individual species," National Aeronautics and Space Administration, Office of Management, Tech. Rep., 1993.

[26] L. O. Berrocal, *Elasticidad*, 3ª ed. McGraw-Hill, 1998, ISBN: 8448120469.

[27] M. Heil, *The equations of linear elasticity, Elasticity lecture notes*. University of Manchester, 2006, Last accessed 26 February 2022. [Online]. Available: https://personalpages.manchester.ac.uk/staff/matthias.heil/Lectures/Elasticity/Material/Chapter5.pdf.

[28] *Constitutive equations, Structural mechanics lecture notes*. Massachusetts Institute of Technology, Last accessed 26 February 2022. [Online]. Available: http://web.mit.edu/16.20/homepage/3_Constitutive/Constitutive_files/module_3_no_solutions.pdf.

[29] *Boundary value problems in linear elasticity, Structural mechanics lecture notes*. Massachusetts Institute of Technology, Last accessed 26 February 2022. [Online]. Available: http://web.mit.edu/16.20/homepage/4_ElasticityBVP/ElasticityBVP_files/module_4_with_solutions.pdf.

[30] J. A. H. Ortega, *Classical linear elastostatics, Computational engineering lecture notes*. Universitat Politècnica de Catalunya, 2021.

[31] J. Fish, *A First course in finite elements / Jacob Fish, Ted Belytschko*, eng. Chichester: John Wiley & sons, 2007, ISBN: 9780470035801.

[32] S. Timoshenko, *Strength of materials, part II*. D. Van. Nortrand. Co., 1941, vol. 245.

[33] *6061-T6 Aluminium – The Ultimate Guide*. Munich: Matmatch GmbH, 2022, Last accessed 05 March 2022. [Online]. Available: https://matmatch.com/learn/material/6061-t6-aluminium.

[34] *Isobaric Properties for Water*. National Institute of Standards and Technology, U.S. Department of Commerce, 2021, Last accessed 05 March 2022. [Online]. Available: https://webbook.nist.gov/chemistry/fluid/.

[35] H. Wong, *Handbook of essential formulae and data on heat transfer for engineers*. Addison-Wesley Longman Limited, 1977.

[36] N. Noda, R. B. Hetnarski, and Y. Tanigawa, *Thermal stresses*. Taylor & Francis, 2003.